Abstract

Title of dissertation: Dust and Molecular Gas in the Winds of Nearby Galaxies

Alexander N. McCormick,
Doctor of Philosophy, 2015

Dissertation directed by: Professor Sylvain Veilleux
Department of Astronomy

Galactic winds provide a fundamental mechanism for galaxy evolution. The outflow of material in winds remains the most likely culprit responsible for a host of galaxy observations, plus mounting evidence for galactic winds at times in the past points to their importance in understanding the history of the universe. Therefore, detailed observations of galactic winds are critical to fleshing out the narrative of galaxy evolution. In particular, the dust and molecular gas of a galaxy's interstellar medium (ISM) play crucial roles in the absorption, scattering, and reemission of starlight, the heating of the ISM, and provide critical materials for star formation.

We present results from archival *Spitzer Space Telescope* data and exceptionally deep *Herschel Space Observatory* data of the dust and molecular gas found in and around 20 nearby galaxies known to host galactic-scale winds. Selecting nearby galaxies has allowed us the resolution and sensitivity to differentiate dust and molecular gas outside the galaxies and observe their typically faint emission. These are the most detailed surveys currently available of the faint dust and molecular gas

components in galactic winds, and we have utilized them to address the following questions: i) What are the location and morphology of dust and molecular gas, and how do these components compare with better known neutral and ionized gas features? ii) How much do dust and molecular gas contribute to the mass and energy of galactic winds? iii) Do the properties of the dust and molecular gas correlate with the properties of the wind-hosting galaxy?

Spitzer archival data has revealed kiloparsec-scale polycyclic aromatic hydrocarbon (PAH) structures in the extraplanar regions of nearly all the wind-hosting galaxies we investigated. We found a nearly linear correlation between the extraplanar PAH emission and the total infrared flux, a proxy for star formation. Our results also suggest a correlation between the height of extraplanar PAH emission and star formation rate surface density, supporting the idea of a surface density threshold on the energy or momentum injection rate for producing detectable extraplanar wind material.

New, very deep *Herschel* data of six nearby dwarf galaxies with known winds show circumgalactic cold dust features on galactic scales, often well beyond the stellar component. Comparisons of these features with ancillary data show an imperfect spatial correlation with the ionized gas and warm dust wind components. We found $\sim$10-20% of the total dust mass in these known wind galaxies resides outside their stellar disks, and $\sim$70% in one case. Our data also hint at metallicity depletion via cold dust ejection and possible correlations of dust and other host galaxy properties, though these tantalizing implications are not statistically significant given the small number of objects in the sample and the uncertainties in the measurements.

Dust and Molecular Gas in the Winds of Nearby Galaxies

by

Alexander N. McCormick

Dissertation submitted to the Faculty of the Graduate School of the
University of Maryland, College Park in partial fulfillment
of the requirements for the degree of
Doctor of Philosophy
2015

Advisory Committee:
Professor Sylvain Veilleux, Chair/Advisor
Professor Alberto Bolatto
Professor Robert D. Hudson
Dr. Janice C. Lee, Space Telescope Science Institute
Professor Stuart Vogel

Preface

The main contents of this thesis consist of two articles: one published in the Astrophysical Journal, and one to be submitted to the Astrophysical Journal. The paper to be submitted is the second in a series of papers by a collaboration using data from the *Herschel Space Observatory* (thus the designation II). The titles and authors of these articles, the publication date of the first, the submission date for the second, and their location in this thesis are as follows:

Paper Titles & Authors	Pub./Sub. Date (Journal)	Thesis Chapter
Dusty Winds: Extraplanar Polycyclic Aromatic Hydrocarbon Features of Nearby Galaxies, by McCormick, A., Veilleux, S., & Rupke, D. S. N.	Pub. 9/2013 (ApJ)	§2
Exploring the Dust Content of Galactic Winds with *Herschel* II. Nearby Dwarf Galaxies, by McCormick, A., Veilleux, S., Meléndez, M., Martin, C. L., Bland-Hawthorn, J., Cecil, G., Heitsch, F., Müller, T., Rupke, D. S. N., Zastrow, J., & Engelbracht, C.	Sub. 9/2015 (ApJ)	§3

Dedicated to my parents and brother:

Rosanne, Michael, and Aaron

Acknowledgments

I owe a huge debt of gratitude to my advisor and mentor, Sylvain Veilleux. I also must recognize my extraordinary collaborators: David Rupke & Marcio Meléndez.

My committee members have provided advice, support, and perhaps just the right amount of prodding: Alberto Bolatto, Stuart Vogel, Stacy McGaugh, & Massimo Ricotti.

I am indebited to Sylvain's other research children for their invaluable help: Hannah Krug, Michael McDonald & Stacy Teng.

Many other colleagues provided useful assistance with code, theory, and miscellaneous galaxy stuff: Rodrigo Herrera-Camus, Katherine Jameson, Lisa Wei, Jonathan Fraine, Taro Shimizu, & Margaret Trippe.

For invaluable help with code, plotting, and data management, I thank Andrew Harris, Peter Teuben, Robert Olling, Marc Pound, Mark Wolfire, & William Sebok

I also recognize the significant contributions of our collaborators for their generous sharing of data, advice, and expertise: Crystal Martin, Joss Bland-Hawthorn, Gerald Cecil, Thomas Müller, & Jordan Zastrow.

Finally, I thank my parents and brother whose love and support keep me sane.

Contents

List of Tables

List of Figures

List of Abbreviations & Acronyms

AGN	active galactic nucleus
CCD	charge-coupled device
CMB	Cosmic Microwave Background
FIR	far-infrared
Gyr	Gigayear
HIPE	Herschel Interactive Processing Environment
HSA	Herschel Science Archive
IMF	initial mass function
IRAC	InfraRed Array Camera
IRAS	InfraRed Astronomical Satellite
IRSA	Infrared Science Archive
ISM	interstellar medium
JWST	James Webb Space Telescope
kpc	kiloparsec
ΛCDM	Lambda cold dark matter
MIPS	Multi-band Imaging Photometer for Spitzer
MIR	mid-infrared
MOPEX	MOsaicker and Point source EXtractor
Mpc	Megaparsec
Myr	Megayear
NIR	near-infrared
PACS	Photodetector Array Camera & Spectrometer
PAH	polycyclic aromatic hydrocarbon
SED	spectral energy distribution
SMBH	super massive black hole
SPIRE	Spectral and Photometric Imaging REceiver
UV	ultraviolet
z	redshift ($1 + z = \lambda_{obsv}$ / λ_{emit})

Chapter 1

Introduction

1.1 Galaxies and Their Evolution

Galaxies consist of stars, planets, black holes, neutrinos, cosmic rays, plasma, gas, dust and molecular material all held together by gravity. These constituents, apart from the black holes and neutrinos, are often called baryonic matter, since the majority of their mass resides in baryons: protons and neutrons. Over the past ∼80 years, robust evidence gathered by Zwicky, Rubin and many others has pointed to the presence of an additional, undetected, "dark matter" halo in the gravitational signatures of galaxies observed via their stellar motion, rotation, and lensing of background light from the distant universe [e.g. Zwicky, 1937, Rubin & Ford, 1970, Tremaine, 1992, Blandford & Narayan, 1992]. The existence of dark matter remains the current prevailing theory we will reference, but certain observations cannot be explained by this model [e.g. McGaugh & de Blok, 1998], possibly supporting a modification to gravity [Milgrom, 1983].

If the universe contained just baryonic and dark matter, it would contract under the force of gravity. This problem led Einstein to artificially adjust models of the universe with a "cosmological constant" which would push back and prevent such a collapse of the cosmos [Einstein, 1917]. However, since Hubble's observations of galaxies' apparent recession in 1929 [Hubble, 1929], we have understood the universe is currently undergoing expansion. Within the last ∼20 years or so observations have confirmed a surprising acceleration of this expansion [e.g. Riess et al., 1998, Schmidt et al., 1998, Perlmutter et al., 1999], driven by a still mysterious phenomenon, currently termed "dark energy" or "vacuum energy."

Baryonic matter, dark matter, and dark energy are the constituents of the universe within the currently canonical ΛCDM model [Komatsu et al., 2009, and references therein], where Λ represents dark energy and CDM denotes "cold dark matter." Comparing models with observations of the small temperature fluctuations of cosmic microwave background [CMB, Penzias & Wilson, 1965, Planck Collaboration et al., 2015, see Figure 1.1] yields the relative fractions of these components: ∼69% dark energy, ∼26% dark matter, and ∼5% baryonic matter [Planck Collaboration et al., 2015]. Although the baryonic matter in galaxies therefore represents the smallest fractional part of the universe, its emission of electromagnetic radiation lights the way, allowing observers to study the dark components by proxy.

The ΛCDM model and an abundance of observational evidence point to the hierarchical build-up of galaxies and galaxy clusters. Observations of the CMB [Figure 1.1, Planck Collaboration et al., 2014] have revealed the matter distribution of the early universe appears quite smooth. This contrasts with its current clumpy

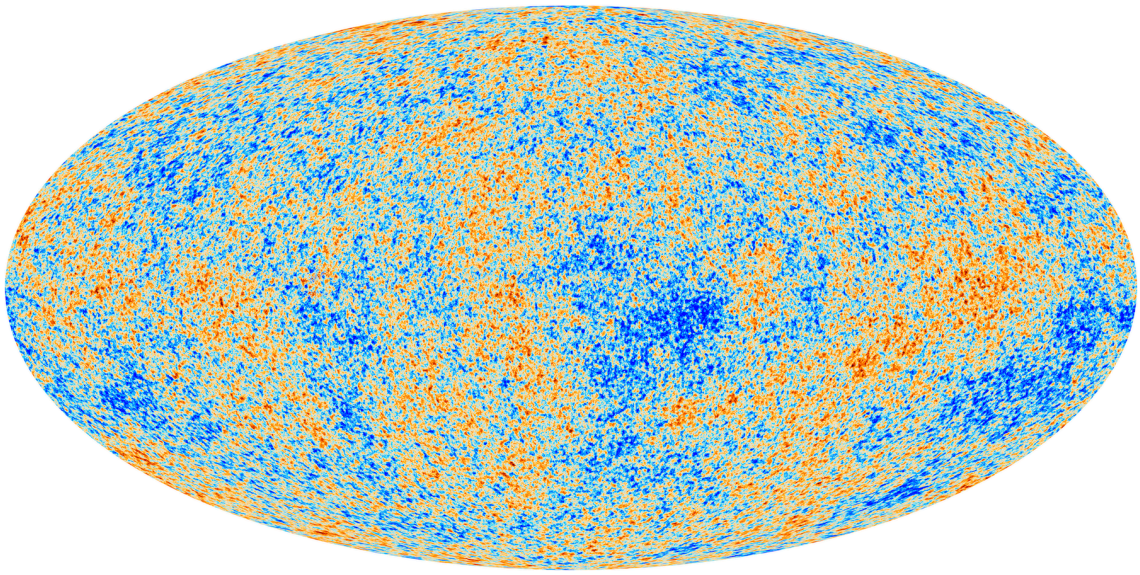

Figure 1.1: Small temperature fluctuations in the Cosmic Microwave Background - as seen by Planck. Credit: ESA and the Planck Collaboration

distribution in which galaxies tend to collide, merge, group, and cluster along a network of filamentary and nodal structures forming a cosmic web [Figure 1.2, Peacock et al., 2001]. Recent large-scale simulations incorporating dark matter and dark energy have reproduced the evolution of the matter distribution from this early, very smooth state to the more clumpy present [Figure 1.3, Springel et al., 2005b, 2008, Boylan-Kolchin et al., 2009]. These models build up structure via the mergers of dark matter halos and the galaxies within them [Davis et al., 1985, Barnes & Hernquist, 1992]. Mergers typically take place with a frequency <1 Gyr^{-1} [e.g. Hopkins et al., 2010], so observations can only take snapshots of the hierarchical build-up process [Zwicky, 1956, Toomre & Toomre, 1972]. Although the large-scale simulations referenced here reliably reproduce the observed cosmic web, they have not reproduced many observed features of stars, supermassive black holes, chemical composition, gas, and dust at the scale of individual galaxies and clusters. As simu-

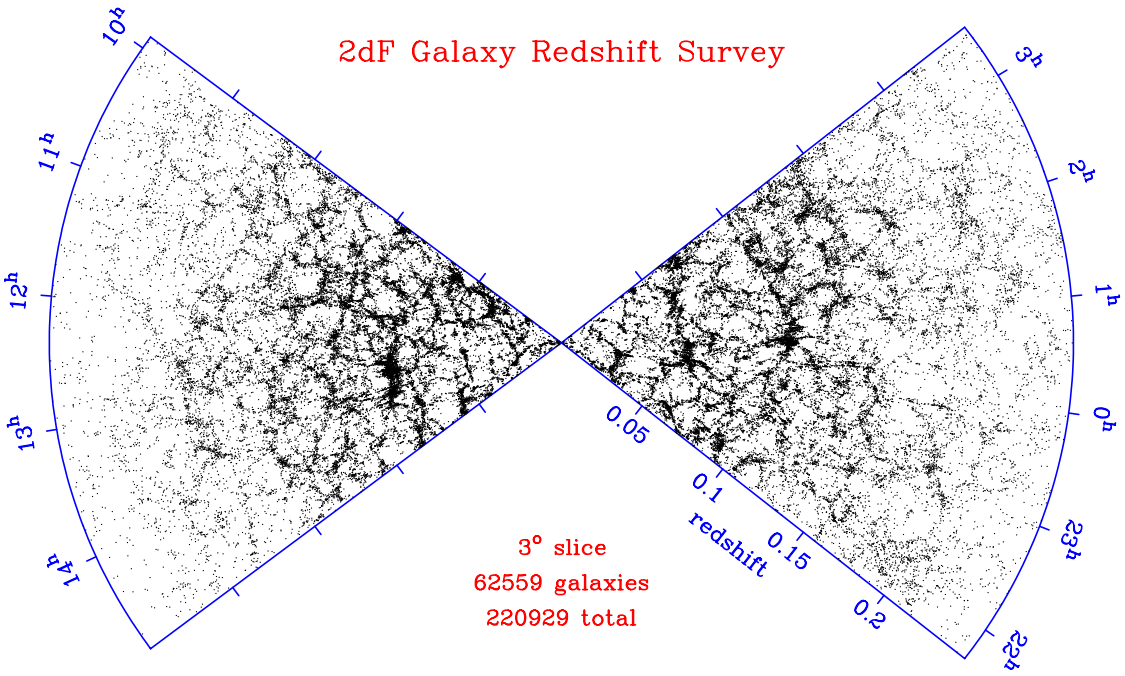

Figure 1.2: A slice of the 2dF Galaxy Redshift Survey [Peacock et al., 2001].

lations become more detailed, multi-wavelength observations have and will provide indispensable constraints.

The following by no means exhaustive list contains some observational features of galaxies not yet resolved by cosmological simulations (i.e. without including some artificial parameters to force agreement):

- *Cosmic star formation history* - Using a variety of techniques and light at different wavelengths, observers have estimated the star formation rate density over the history of the universe [see Madau & Dickinson, 2014, for a review]. Although there are considerable challenges in reliably measuring star formation rates at high redshift, the most carefully calculations point to a peak in the star formation rate at $z \approx 1.9$ or approximately 3.5 Gyr after the Big Bang

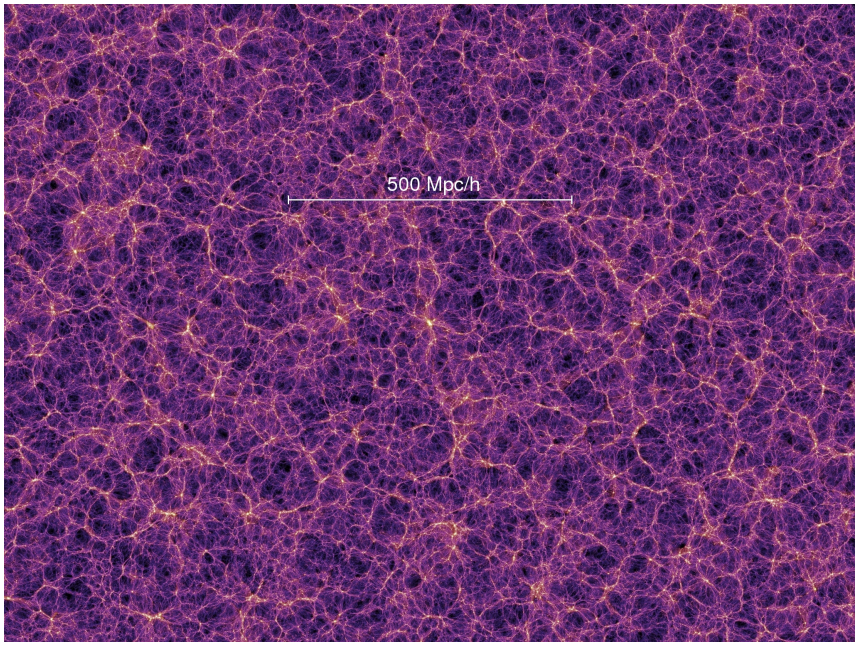

Figure 1.3: A $z = 0$ (t = 13.6 Gyr) slice of the Millennium Simulation [Springel et al., 2005b] with scale indicated in Megaparsecs per Hubble parameter h.

initiated the expansion of the universe (see Figure 1.4).

- *Supermassive black holes / AGN* - The observed ubiquity of supermassive black holes (SMBH, $M_{BH} \gtrsim 10^5\ M_\odot$) at the centers of galaxies is a relatively recent result [Magorrian et al., 1998] and necessitates some combination of matter accretion and mergers to build up the types of masses observed in the local universe at $z = 0$. Many of these central SMBHs actively accrete material, which can lead to bright emission outshining the entire surrounding galaxy, highly collimated, relativistic jets, and the galactic winds which are the subject of this thesis (described in more detail in § 1.2). A SMBH exhibiting some or all of this behavior is called an "active galactic nucleus" (AGN).

- *M_{BH}-σ relation* - The masses of SMBHs at the centers of galaxies, M_{BH}, are strongly correlated with the surrounding stellar bulge masses as measured by

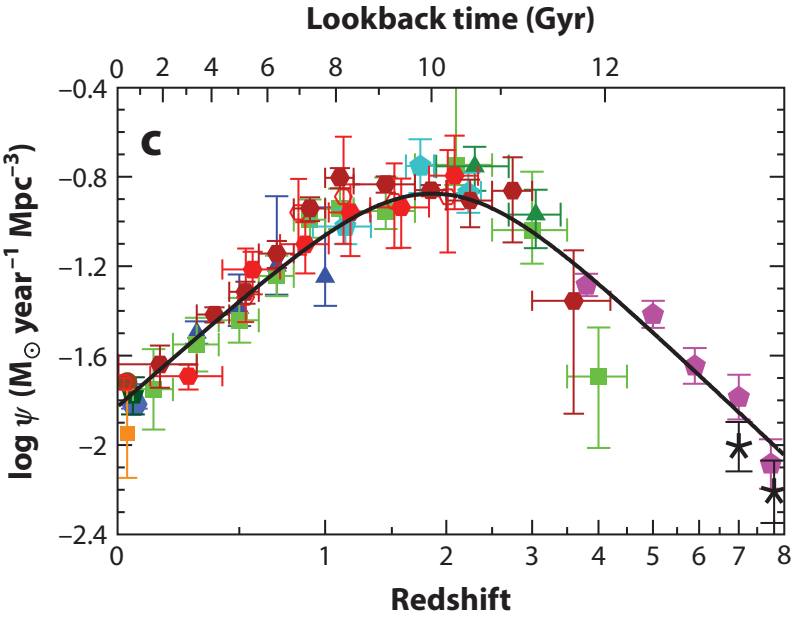

Figure 1.4: Figure 9c from Madau & Dickinson [2014]. The red points represent star formation rate density (ψ) determined via IR observations while the blue, green, and lavender points come from UV observations. The black line is a fit to the data.

the velocity dispersion of the stars in the bulge, σ [Ferrarese & Merritt, 2000, Gebhardt et al., 2000] - see Figure 1.5. Since the scale of influence for the SMBH is several orders of magnitude smaller than that of the stellar bulge, this observational result presents the serious challenge of explaining how these two galactic components "know" about each other or somehow evolve together.

- *M_*-Z relation* - The initial mass function, which describes the probability density of stellar masses, doesn't appear to vary significantly from one group of stars to another on mass scales much smaller than the mass of even small galaxies [Kroupa, 2001]. It follows that similar groups of stars should undergo similar evolution, producing a similar metallicity (Z) regardless of overall galactic mass. Metallicity, Z, is the mass fraction of "heavy" elements or

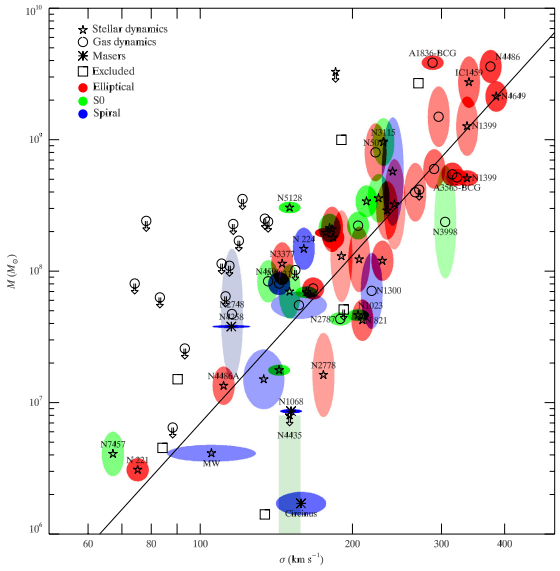

Figure 1.5: Figure 1 from Gültekin et al. [2009]. A correlation between central SMBH mass, M, in units of solar masses, and the stellar bulge velocity dispersion, σ.

metals, which excludes hydrogen and helium. However, observations show a deficit of heavy elements for lower mass galaxies [Tremonti et al., 2004, Figure 1.6]. Therefore, some process must be suppressing the production of metals in low mass galaxies.

- *The "too big to fail" problem* - Dark matter simulations predict many more massive dark matter sub-halos than the number of observed dwarf galaxy counterparts in the Local Group, the group of galaxies surrounding the Milky Way [Boylan-Kolchin et al., 2011]. While observers continue to discover new extremely low mass galaxies, detection limits dictate that the predicted sub-halo counterparts would have already been found by now.

- *Enrichment of the IGM / ICM* - The attenuation of light from distant quasars [Zhu et al., 2014] and direct infrared (IR) and X-ray and radio observations

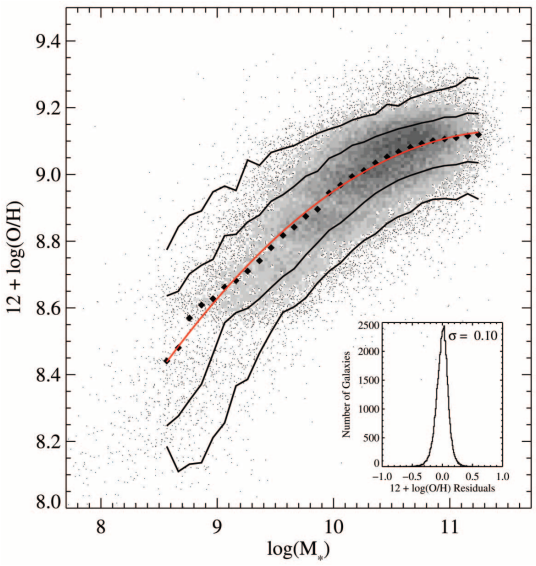

Figure 1.6: Figure 6 from Tremonti et al. [2004]. A relation between stellar mass, in units of solar masses, and gas-phase oxygen abundance for ∼53,400 star-forming galaxies in the Sloan Digital Sky Survey (SDSS). The black diamonds are binned data, the red line is a fit to the binned data, and the black contours enclose 68% and 95% of the galaxies (gray points).

of galaxy clusters show the enrichment of the intergalactic and intracluster media, the IGM and ICM, respectively. The metals within these extragalactic components preclude their coming from primordial abundances, so they must have been ejected from the stars where they formed at some point, suggesting a galactic origin.

While not a panacea for all the issues raised by these observational results, the removal of material via galactic winds (also known as negative feedback or outflows) has been invoked to help explain many of the challenges raised by each of these apparent features of galaxy evolution.

1.2 Galactic Winds and Their Properties

Much of the following discussion relies heavily on a review article detailing the observational results and fundamental physics of galactic winds, Veilleux et al. [2005].

Galactic winds are typically faint compared to their host galaxies [e.g. Lehnert & Heckman, 1995], which helps explain why they weren't detected until about 50 years ago. The first observations of galactic winds date back to the early 1960s as observers gradually realized the immense energy fluxes emanating from sources like the first identified quasar [Hazard, 1962] and an explosive event in Messier 82 [Lynds & Sandage, 1963] plus the outflows from several elliptical galaxies [Burke, 1968] likely were fundamentally altering their hosts. The relative lack of interstellar medium (ISM) material in elliptical galaxies when compared with spirals helped drive interest in galactic winds as a possible mechanism for removing this material [Johnson & Axford, 1971, Mathews & Baker, 1971]. Since those early inklings, the advent of highly sensitive CCD cameras, larger telescopes, plus instruments and space observatories capable of revealing all parts of the electromagnetic spectrum have allowed detailed study of these typically faint, but vitally important features of galaxies.

Momentum or energy injection via robust star formation, an AGN, or perhaps both can drive the formation of a galactic wind. Except in the case of very young ($<10^7$ years), high metallicity ($Z > Z_\odot$), starbursts containing many high-mass (

$\gtrsim 60\ M_\odot$), stellar winds alone typically do not provide enough energy to break out of the ISM, but normally they can prime the pump by blowing a bubble of hot ($\sim 10^4$ K) diffuse ionized hydrogen (an H II region). This leaves a thinner layer of ISM for supernovae to puncture when they eventually explode. If enough high mass stars supernova in close proximity, the momentum injection rate including stellar winds can be calculated based on the simulations of Leitherer et al. [1999] and is on the order of 5×10^{33} (SFR / $M_\odot$ yr^{-1}) dyne (where SFR is the star formation rate). Once the supernovae impart their momentum, Rayleigh-Taylor instabilities can develop where the expanding supernova bubble meets the remaining thinner layer of ISM. If enough momentum is injected without too much energy radiating away, then a break out will occur likely sweeping out some of the hot ionized gas, molecular material, and dust in the ISM. The bubble may not burst if not enough momentum is injected or if too much of it radiates away. However, the occurrence of a break out does not also imply escape from the gravitational potential of the galaxy and its dark matter halo, so material may fall back onto the galaxy in a "galactic fountain."

Mass accretion onto a SMBH powers an AGN and can provide enough energy to drive a galactic wind. The infall of mass onto the black hole can release energy to the ISM via electron scattering of radiation produced in the accretion disk, scattering and absorption on dust grains, photoionization, or scattering in atomic resonance lines. The relative importance of these properties depends on the brightness and geometry of the AGN, its accretion disk, and other surrounding features, plus the local properties of the ISM. Radiation from the AGN may cause the surrounding gas

to undergo runaway heating, which in turn might then drive an outflow if through heating, its sound speed exceeds the rotational velocity of typical galaxies. Finally magnetorotational instability in the accretion disk may help drive an active corona, which generate outflows and further boosts them via centrifugal force.

Simulations have shown that the outflows of material in winds can inhibit the growth of a central supermassive black hole and curb the galactic SFR by removing its fuel [Di Matteo et al., 2005, Narayanan et al., 2008, Hopkins & Elvis, 2010]. As discussed above winds have also been invoked to explain a host of galaxy observations, including but not limited to the mass-metallicity relation [Tremonti et al., 2004], the relation between central black hole mass and bulge velocity dispersion [Ferrarese & Merritt, 2000, Gebhardt et al., 2000], and metal enrichment of the ICM and IGM [Renzini, 1997, Buote, 2000]. Furthermore, mounting evidence for galactic winds at $z > 1$ [e.g. Lowenthal et al., 1997, Pettini et al., 2001, Smail et al., 2003, Weiner et al., 2009] in accordance with cosmic star formation history points to their importance. Care must be exercised when trying to draw any conclusions about high-z galaxies from observations of nearby wind-hosting galaxies. However, detailed observations of nearby galactic winds still provide the best opportunity to understand this crucial process in the narrative of galaxy evolution.

1.3 Infrared (IR) Emission from Galaxies

Dust grains and interstellar molecular material absorb and scatter star light. Anyone who has gazed up at the Milky Way for a while likely noticed it appears

darker in some areas where lanes of dust obscure parts of the stellar disk. Caroline and William Herschel first discovered dark nebulae [Herschel, 1785], but it wouldn't be until the 20th century that observations established interstellar dust grains cause the obscuration [Wolf, 1923, Trumpler, 1930]. Since then, observations by Wilson et al. [1970] and others have established the molecular content of the Milky Way and extragalactic sources, so that now "dust" and "molecular gas/material" are often used interchangeably. These components of the ISM hold special importance, because dense molecular clouds tend to provide the nurseries for the most intense star formation. Dust also acts a catalyst helping form molecular hydrogen, H_2, in the ISM. Finally, dust absorbs stellar radiation in the UV through the near-IR (NIR) and re-emits it in the mid-to-far IR (MIR - FIR). Observations of this reprocessed, IR light provide the basis for this thesis.

IR observations remain challenging, though. Earth's atmospheric opacity blocks nearly all of the IR spectrum ($\sim$ 1 μm - 1 mm) with just a few transmission windows (see Figure 1.7). Therefore, with a few exceptions, observing most of the useful IR features of galaxies requires space-based telescopes. Warm electronics and any other slightly heated element of the instrument emit in the IR as well, providing bothersome instrument noise, so IR telescopes and instruments require cooling below temperatures where this systematic noise could drown a signal.

Further complicating matters, galactic winds are often faint relative to their host galaxies [e.g. Lehnert & Heckman, 1995]. Nearby galaxies known to host a wind provide the best opportunity for detailed IR observations of any dust and molecular gas components because of their brightness. Polycyclic aromatic hydrocarbons

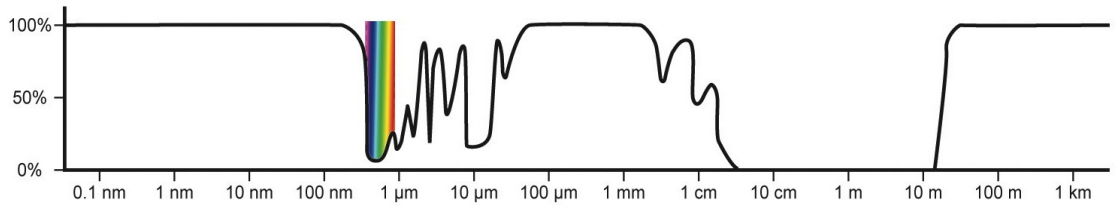

Figure 1.7: The opacity of Earth's atmosphere versus electromagnetic wavelength. The IR range is $\sim$ 1 μm - 1 mm. Credit: NASA

(PAHs) are usually detectable via the mid-infrared (MIR) 7.7 μm emission feature [Leger & Puget, 1984, Allamandola et al., 1985, 1989]. Dust continuum emission shows up in the far-infrared (FIR), at wavelengths $\gtrsim$ 60 μm [Draine, 2003]. The H_2 v = 1-0 S(1) 2.12 μm line provides a diagnostic for the molecular gas component [Veilleux et al., 2009b]. In addition to the relative faintness of the winds, detailed spatial mapping works best for nearby galaxies due to the resolution constraints of current IR instruments. Since many known winds emerge along the minor axes of their host galaxies [e.g. Sharp & Bland-Hawthorn, 2010], surveys focused on highly inclined galaxies (i $\gtrsim$ 60) allow for the delineation of the galaxy's wind component from its stellar component. For these reasons, we have chosen IR observations of nearby, close to edge-on galaxies with known wind properties.

1.4 Observatories/Instruments Used in This Work

The archival and new data presented in this thesis come from the *Spitzer Space Telescope* and the *Herschel Space Observatory* respectively. Both telescopes are still in their orbits (*Herschel* resides at the L2 Lagrangian point), and both have run out of their cryogenic material. *Spitzer* continues to operate at its shortest wavelengths

where IR noise is less of a problem in what is called its "Warm Mission," while *Herschel* can no longer perform observations as of June, 2013. Data from both telescopes are now publicly available via the Infrared Science Archive (IRSA), and the Herschel Science Archive (HSA).

1.4.1 *Spitzer Space Telescope* - IRAC

The InfraRed Array Camera (IRAC) on *Spitzer* has four imaging channels; one each centered at 3.6, 4.5, 5.8, and 8.0 μm. Of course, atmospheric opacity requires space-based observations in these wavebands. Each channel consists of a 256 $\times$ 256 pixel detector covering $\sim$5' $\times$ 5' on the sky, which translates to a pixel scale of $\sim$1.22"/pixel. Each channel has a spatial resolution of $\sim$2". Some of the galaxies in our sample fit within this array, while others required maping. The 7.7 μm strong PAH emission feature and another PAH feature at 8.6-8.8 μm make the IRAC 8.0 μ channel ideal for detecting warm dust in extragalactic sources. Meanwhile the 4.5 μ channel detects the tail of the stellar emission providing a convenient comparison. We performed some of the archival data reduction with the *Spizter* Science Center-provided software MOPEX (see Chapter 2).

1.4.2 *Herschel Space Observatory* - PACS & SPIRE

Herschel's PACS and SPIRE instruments each have three imaging channels: centered at 70,100, and 160 μm for PACS, and centered at 250, 350, and 500 μm SPIRE. We did not collect data in the PACS 100 μm channel. At these wavelengths

in the FIR, the atmosphere is completely opaque, again requiring space-based observations. The PACS channels have pixel sizes 1.4" and 2.85" for the 70 and 160 μm channels respectively, which is about 1/4 the size of PSF FWHM. The SPIRE channels likewise have pixels sizes 4.5", 6.25", and 9.0" for the 250, 350, and 500 μm channels respectively, again about 1/4 the size of PSF FWHM. Cool and cold (T <100K) dust in the ISM of galaxies tends to emit in these wavebands as an approximate blackbody, which through fitting allow approximate measurements of the dust mass, temperature, and spectral index. We used the *Herschel*-provided HIPE software to perform initial data reduction (see Chapter 3).

1.5 Outline of Thesis

In Chapter 2, we present the results of our *Spitzer* archival survey of 16 wind-hosting galaxies. Chapter 3 contains the analysis and results of our new, very deep *Herschel* observations of six nearby dwarf galaxies, of which three overlap with the *Spitzer* survey. Chapter 4 summarizes our results, raises analysis still to be done on our NEWFIRM data, and discusses some potential future directions for continuing research. Finally, Appendices A and B contain notes on individual galaxies and their dust and molecular gas features.

Chapter 2

Dusty Winds: Extraplanar Polycyclic Aromatic Hydrocarbon Features of Nearby Galaxies

2.1 Introduction

Superwinds are galaxy-scale outflows of material often present in galaxies hosting star formation or active galactic nuclei (AGNs) [Heckman et al., 1990, Lehnert & Heckman, 1995, Veilleux et al., 2005]. The feedback from winds plays an important role in the evolution of galaxies, their interstellar media (ISM), and the surrounding intergalactic or intracluster medium in which they are embedded. Outflows of material can inhibit the growth of a central supermassive black hole and limit the star formation rate (SFR) by removing the fuel for star formation [Di Matteo et al., 2005, Narayanan et al., 2008, Hopkins & Elvis, 2010].

Prior to 2005, much of the observational data have emphasized the entrained

gas in winds from the neutral gas [Heckman et al., 2000, Rupke et al., 2002, 2005a,b,c, Schwartz & Martin, 2004, Martin, 2005] to ionized gas [Heckman et al., 1990, Lehnert & Heckman, 1995] to the highly ionized X-ray emitting plasma [Read et al., 1997, Pietsch et al., 2000, McDowell et al., 2003, Ehle et al., 2004, Huo et al., 2004, Strickland et al., 2004a,b]. Recent observations have shown that these outflows entrain dust [Heckman et al., 2000, Tacconi-Garman et al., 2005, Engelbracht et al., 2006, Roussel et al., 2010] and molecular gas [Veilleux et al., 2009b, Fischer et al., 2010, Feruglio et al., 2010, Irwin et al., 2011, Sturm et al., 2011, Alatalo et al., 2011, Aalto et al., 2012].

The striking detection by Engelbracht et al. [2006] of polycyclic aromatic hydrocarbon (PAH) emission in the prototypical wind of M82 has demonstrated that the four near-infrared (NIR) to mid-infrared (MIR) channels of the InfraRed Array Camera (IRAC) on board the *Spitzer Space Telescope* are ideal for detecting warm dust and molecules in galactic winds. PAHs are aromatic molecules a few Å in diameter and are often referred to as small dust grains. Tens of carbon atoms with a "fringe" of hydrogen atoms make up a typical PAH molecule, while the largest ones contain hundreds of carbon atoms. These molecules are found throughout the ISM of our Galaxy as well as in nearby galaxies exhibiting evidence of ongoing or recent star formation. Since they efficiently absorb ultraviolet and optical photons, their reprocessed infrared (IR) emission features are often much stronger than the background dust continuum [Smith et al., 2007]. PAHs are widely believed to be responsible for emission features in the NIR to MIR at 3.3, 6.2, 7.7, 8.6-8.8 and 11.3-11.9 μm [Leger & Puget, 1984, Allamandola et al., 1985, 1989].

The 3.6, 4.5 and 5.8 μm IRAC channels can detect dust at temperatures a few hundred to 1000 K, and the 3.6, 5.8 and 8.0 μm channels are sensitive to PAH emission features. The 8.0 μm band is particularly important due to the 7.7 μm PAH feature (e.g. Figure 1 of Reach et al. 2006) which typically dominates compared to other flux contributions from stars, dust continuum, molecular emission, and fine structure lines (see discussion in § 2.3.3). Relative to the 8.0 μm band, the 4.5 μm band contains very little PAH emission while significantly more stellar and dust continuum emission. Some H_2 rotational line emission and trace Brα emission may also contribute in the 4.5 μm band [Engelbracht et al., 2006]. The 3.6 and 5.8 μm bands also contain the 3.3 and 6.2 μm PAH emission features respectively, so using these bands as tracers of stellar emission is less reliable. Therefore, a comparison of 4.5 and 8.0 μm images differentiates PAH emission from stellar emission. We have used this comparison to identify extraplanar PAH features and estimate extraplanar PAH flux. Our sample of local galaxies provides the resolution necessary to distinguish coplanar from extraplanar emission and to study morphological features. In this paper, PAH emission or PAH flux refers to measurements in the IRAC 8.0 μm band rather than a bolometric PAH measurement.

In § 2.2, we describe the selection criteria for our sample of nearby galaxies and provide tables summarizing their basic properties and the data we used from the *Spitzer* archive. In § 2.3 and 2.4, we describe the data reduction process with example images and our analysis respectively. We present our results in § 2.5, include images of each galaxy in the IRAC 4.5 and 8.0 μm channels, discuss some of the most prominent features we have identified, compare our results with previous

observations, and describe variations with galaxy type, IR luminosity, and SFR surface density. Our results are summarized in § 2.6. Appendix A contains discussion of each individual galaxy and its features.

2.2 Sample

We selected the 16 galaxies in our sample (listed in Table 2.1) based on three main criteria. (1) From observations at other wavelengths, they are known to host galactic-scale winds or exhibit associated extraplanar material. Most have disk morphology with inclinations (i) typically $\sim 70°$, making extraplanar regions distinguishable from the galaxy's disk. (2) They are nearby galaxies with a median distance of 8.6 Mpc. We adopted redshift-independent distance values (except for NGC 2992) found using the tip of the red giant branch or the Tully-Fisher relation. By choosing local sources, we maintain good spatial resolution even for the most distant galaxy in our sample: at the adopted distance of 31 Mpc for NGC 2992, the 1.72" and 1.98" mean FWHM of the 4.5 and 8.0 μm IRAC bands resolve structure down to $\sim$ 260 pc and $\sim$ 300 pc respectively. (3) Each source has publicly available IRAC data in the *Spitzer* archive (summarized in Table 2.2). Data for four of the galaxies (NGC 1482, NGC 1705, NGC 4631, and M82) came from the SINGS survey [Kennicutt et al., 2003].

From previous multi-wavelength observations, most of the galaxies host active star formation (H II regions), two (NGC 3079 and NGC 4945) contain both H II regions and an AGN and two (NGC 2992 and NGC 4388) exhibit AGN but little or

Table 2.1: Nearby Wind Galaxies from the *Spitzer* Archive and Their Properties

Galaxy	Type [1]	Morph. [2]	D_{25} (') [3]	i (°) [4]	d (Mpc) [5]	L_{IR} ($10^{10} L_{\odot}$) [6]	Wind/eDIG Ref(s). [7]
NGC 55	H II	SB(s)m	29.3	80	1.6	0.026	1,2,3,4,5,6,7
NGC 253	H II	SAB(s)c	30.0	76	3.46	3.44	1,4,7,8,9,10,11,12,13,14,15
NGC 891	H II	SA(s)b?	13.5	79	9.6	2.32	5,7,14,15,16,17,18
NGC 1482	H II	$SA0^{+}$ pec	2.2	56	19.6	3.82	7,12,14,15,19,20
NGC 1569	H II	IBm	3.63	61	3.36	0.16	21,22,23,24
NGC 1705	H II	$SA0^{-}$ pec	1.8	42	5.1	0.009	25,26,27,28
NGC 1808	H II	(R)SAB(s)a	5.2	53	12.3	4.86	12,29
NGC 2992	AGN	Sa pec	3.5	72	31	2.94	30,31,32,33
NGC 3079	H II + AGN	SB(s)c	7.9	80	20.2	6.58	1,7,9,14,15,34,35,36
NGC 3628	H II	Sb pec	14.8	78	12.7	2.84	1,7,12,14,15,37,38
NGC 4388	AGN	SA(s)b	5.6	77	16.7	1.18	30,31,32,39
NGC 4631	H II	SB(s)d	15.5	80	7.62	1.61	1,7,8,14,15,40
NGC 4945	H II + AGN	SB(s)cd	23.3	79	3.55	2.49	7,9,14,15,41,42
NGC 5253	H II	pec	5.2	67	3.77	1.64	43
NGC 6810	H II	SA(s)ab	3.8	74	28.7	5.30	12,18,44
M82	H II	I0	11.2	67	3.53	5.56	1,7,8,9,45,46,47

[1] Optical/UV types are galaxies identified by star-forming H II regions (H II), active galactic nuclei (AGN), and galaxies containing both an AGN and star-forming H II regions (H II + AGN).

[2] de Vaucouleurs morphological type from de Vaucouleurs et al. [1991] (hereafter RC3).

[3] Diameter (major axis) in arcminutes based on 25th magnitude B-band observations (RC3 or Lauberts & Valentijn [1989]).

[4] Inclination in degrees with respect to the line of sight from the calculation of $\cos^{-1}(b/a)$ (RC3).

[5] z-independent distance (except NGC 2992). References: NGC 55, NGC 891, and NGC 1482: Tully 1988; NGC 253: Dalcanton et al. 2009; NGC 1569: Grocholski et al. 2008; NGC 1705: Tosi et al. 2001; NGC 1808 and NGC 4945: Tully et al. 2009; NGC 2992: Veilleux et al. 2001; NGC 3079 and NGC 6810: Springob et al. 2009; NGC 3628: Willick et al. 1997; NGC 4388: Yasuda et al. 1997; NGC 4631: Seth et al. 2005; NGC 5253: Sakai et al. 2004; M82: Karachentsev et al. 2002.

[6] IR luminosity (8 - 1000 μm) expressed in units of $10^{10} L_{\odot}$, calculated using equations in Table 1 of Sanders & Mirabel [1996], IRAS flux densities listed in the NASA/IPAC Extragalactic Database [Moshir et al., 1990, Sanders et al., 2003], and the distances listed in this table.

[7] Selected references to a galactic wind or extraplanar diffuse ionized gas (eDIG): (1) Dahlem et al. 1998; (2) Ferguson et al. 1996; (3) Graham & Lawrie 1982; (4) Hoopes et al. 1996; (5) Miller & Veilleux 2003; (6) Otte & Dettmar 1999; (7) Tüllmann et al. 2006; (8) Alton et al. 1999; (9) Heckman et al. 1990; (10) Hoopes et al. 2005; (11) Pietsch et al. 2000; (12) Sharp & Bland-Hawthorn 2010; (13) Strickland et al. 2002; (14) Strickland et al. 2004a; (15) Strickland et al. 2004b; (16) Alton et al. 1998; (17) Howk & Savage 1997; (18) Bregman et al. 2013; (19) Hameed & Devereux 1999; (20) Veilleux & Rupke 2002; (21) della Ceca et al. 1996; (22) Heckman et al. 1995; (23) Hunter et al. 1993; (24) Waller 1991; (25) Heckman et al. 2001; (26) Meurer et al. 1989; (27) Meurer et al. 1992; (28) Meurer et al. 1998; (29) Phillips 1993; (30) Colbert et al. 1996; (31) Colbert et al. 1998; (32) Gallimore et al. 2006; (33) Veilleux et al. 2001; (34) Cecil et al. 2001; (35) Pietsch et al. 1998; (36) Veilleux et al. 1994; (37) Dahlem et al. 1996; (38) Fabbiano et al. 1990; (39) Veilleux et al. 1999; (40) Wang et al. 2001; (41) Moorwood et al. 1996; (42) Nakai 1989; (43) Marlowe et al. 1995; (44) Strickland 2007; (45) Engelbracht et al. 2006; (46) Strickland et al. 1997; (47) Veilleux et al. 2009b.

Table 2.2: *Spitzer Space Telescope* Archival Data

Galaxy	Exp. [1]	t_{exp} (s) [2]	*Spitzer* AOR [3]	PI (survey) [4]	$\sigma_{4.5}$ [5]	$\sigma_{8.0}$ [6]
NGC 55	180	30 (26.8)	14478592	de Jong, R. S.	0.0062	0.0276
NGC 253	135	30 (26.8)	18377728	Armus, L.	0.0076	0.0252
	72	30 (26.8)	18377984			
	168	30 (26.8)	18378240			
	168	30 (26.8)	18378496			
	48	30 (26.8)	18378752			
NGC 891	96	100 (96.8)	3631872	Fazio, G.	0.0171	0.0130
	128	100 (96.8)	3632128			
	128	100 (96.8)	3632384			
NGC 1482	4	30 (26.8)	5533696	Kennicutt, R. (SINGS)	0.0104	0.0450
NGC 1569	5	12 (10.4)	4434944	Fazio, G.	0.0220	0.0850
NGC 1705	4	30 (26.8)	5535744	Kennicutt, R. (SINGS)	0.0068	0.0303
	4	30 (26.8)	5536000			
NGC 1808	16	30 (26.8)	18284800	Fisher, D. B.	0.0061	0.0264
NGC 2992	15	12 (10.4)	4933376	Houck, J. R.	0.0139	0.0425
NGC 3079	16	30 (26.8)	22000896	Rieke, G.	0.0061	0.0292
NGC 3628	36	30 (26.8)	22547200	Kennicutt, R. (LVL)	0.0082	0.0378
	36	30 (26.8)	22547456			
NGC 4388	9	12 (10.4)	27090688	Forman, W. R.	0.0134	0.0598
NGC 4631	15	30 (26.8)	5540864	Kennicutt, R. (SINGS)	0.0081	0.0359
	15	30 (26.8)	5541120			
NGC 4945	30	30 (26.8)	21999616	Rieke, G.	0.0142	0.0636
NGC 5253	24	12 (10.4)	4386048	Houck, J. R.	0.0131	0.0466
NGC 6810	1	12 (10.4)	12471808	Gallimore, J. F.	0.0583	0.1331
M82	10	12 (10.4)	13457920	Kennicutt, R. (SINGS)	0.0081	0.0443
	20	30 (26.8)	13458176			
	20	30 (26.8)	13458432			
	10	12 (10.4)	13459200			

[1] Exp. = number of exposures used for our reduction - many extraneous exposures were excluded. The same number of exposures were used from each IRAC channel.
[2] Integration time for each frame (effective integration time per pixel) in seconds.
[3] *Spitzer* Astronomical Observation Request identifing the data set we used for each galaxy in the *Spitzer* archive.
[4] Principal Investigator and survey (e.g. SINGS), where applicable.
[5,6] σ of the background noise for the combined/mosaicked IRAC 4.5 and 8.0 μm images in units of (MJy sr^{-1}).

no ongoing star formation. Since NGC 55 and NGC 891 are not generally considered starburst galaxies, but do contain active star forming regions, we used the broader catch-all 'H II' type to include a range of SFRs.

Rossa & Dettmar [2003] investigated extraplanar diffuse ionized gas (eDIG) in Hα for a sample of nearby edge-on spiral galaxies. Their sample covered a range of IR luminosities (L_{IR}) in order to determine minimum thresholds for SFR surface density (Σ_{SFR} - from far-IR surface brightness, L_{FIR}/D_{25}^2) and far-IR flux ratio (S_{60}/S_{100}) leading to the presence of eDIG. All the galaxies in our sample apart from NGC 55 lie above their derived lower limit for L_{FIR}/D_{25}^2 ($(3.2 \pm 0.5) \times 10^{40}$ erg s^{-1} kpc^{-2}) and lie either near or above their limit for S_{60}/S_{100} (0.4). Combining their data with that of Lehnert & Heckman [1995], Rossa & Dettmar [2003] noted the apparent correlation between Σ_{SFR} and far-IR flux ratio, which is also recovered in our sample as shown in Figure 2.1. The Σ_{SFR} shown in Figure 2.1 was derived from Kennicutt [1998] using the L_{IR} and D_{25} values in Table 2.1.

2.3 Data Reduction

Extended, extraplanar emission features are typically faint compared to their host galaxy and its nuclear regions. These features are particularly susceptible to confusion with data artifacts even for nearby, resolved galaxies. Therefore, a careful data reduction process is necessary to distinguish emission features from a number of potential artifacts.

Our sample contains data from a variety of observations, and each of the

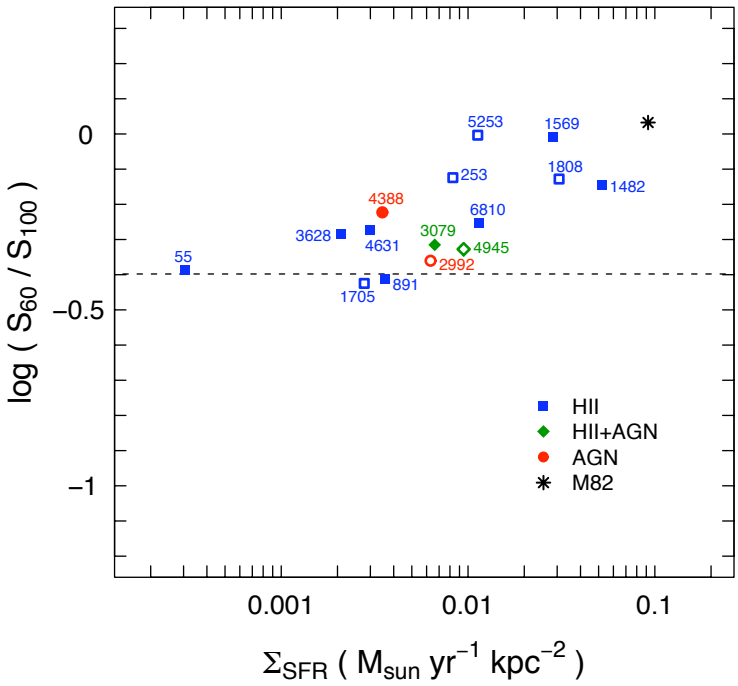

Figure 2.1: Far-infrared color vs. SFR surface density as analog to Fig. 5 in Rossa & Dettmar [2003]. We have included their threshold for IRAS warm galaxies at $S_{60}/S_{100} \geq 0.4$ as the dashed line. Σ_{SFR} was derived from Kennicutt [1998] using the D_{25} values in Table 2.1 for consistency with the method of Rossa & Dettmar [2003]. Open points represent galaxies for which we used a 20σ region to define the disk in our flux measurements, while solid points used a fitted scale height region (see § 2.4.2). Points are labeled with each galaxy's NGC number (except for M82).

galaxies has different properties and morphology, so the lack of uniformity made it impossible to use a single data reduction rubric for all sources. Therefore, we tailored our approach to each data set's individual features and artifacts. Typically, we used the basic calibrated data, uncertainty and mask FITS files from the *Spitzer* archive as our starting point. Since we were most interested in the extraplanar emission, maintaining the quality of the galaxy's nuclear region was sometimes sacrificed in order to get a better result for extraplanar regions. We also dealt with other features such as cosmic ray hits, image alignment, and rotation. However, we dealt with these

relatively minor issues in standard ways, so we do not discuss them here.

2.3.1 Removal of IRAC Artifacts

The mitigation of artifacts in the IRAC basic calibrated data presents a variety of challenges due to electronic, instrumentation, and environmental effects. Here, we discuss the major artifact corrections performed on the data in our sample. A comprehensive discussion of the IRAC pipeline and data artifacts can be found in the IRAC instrument handbook[1].

2.3.1.1 SSC-contributed Artifact Correction Code

All of the IRAC data sets from the *Spitzer* archive contain basic calibrated data images (BCDs), uncertainty maps, and mask files amongst their data products. These products are the result of the *Spitzer Science Center* (SSC) pipeline which corrects for detector bias, does dark subtraction, flatfielding and photometric calibrations. Prior to release, some of the data were also run through a SSC-contributed artifact mitigation code[2], so these data contain corrected basic calibrated data (CBCDs) in addition to the original BCDs. The SSC-contributed code attempts to correct for the following artifacts:

- Column pulldown/pullup - a uniform bias shift up or down within columns containing a bright source. According to the IRAC instrument handbook, this artifact only appears in the 3.6 and 4.5 μm channels, but we also observed a

[1]http://ssc.spitzer.caltech.edu/irac/iracinstrumenthandbook/

[2]http://ssc.spitzer.caltech.edu/dataanalysistools/tools/contributed/irac/iracartifact/

similar artifact in some 8.0 μm data (see § 2.3.1.3).

- Muxbleed - a periodic shift in the bias along rows in the image containing a bright source such as a star. It appears like a decaying "trail of breadcrumbs". This artifact only affects the 3.6 and 4.5 μm channels.

- Electronic banding - a nearly constant bias shift to higher values across rows containing a bright source. This artifact appears only in the 5.8 and 8.0 μm channels.

- First frame effect - a bias effect on the entire frame, which makes consecutive frames mismatched - a problem when co-adding images or creating mosaics. In our mosaics and image stacks, we excluded the first short frame taken at each new pointing, since those frames are most affected by the first frame effect.

The SSC-contributed code does not correct full-array pull-up, internal scattering, optical banding, "muxstriping", or persistent images. For a detailed description of these artifacts, consult the IRAC instrument handbook. We discuss the correction of full-array pull-up, internal scattering, and optical banding in the following sections. The data are minimally affected by "muxstriping" or persistent images, so in general these artifacts could be ignored. Whenever advantageous, we worked from the CBCDs, since they often exhibited a useful reduction or elimination of the prescribed artifacts. As implied above, some data sets only contained BCDs and no CBCDs. For those data sets, we downloaded the SSC-contributed code and used it to produce CBCDs.

2.3.1.2 Full-Array Pull-Up and Internal Scattering

When integrating individual frames in both the 4.5 μm and 8.0 μm channels, the total flux from all sources within the frame contributes a uniform, proportional offset across all pixels - an effect called "full-array pull-up" by the IRAC instrument handbook. In addition to this effect, some light can scatter approximately uniformly within the array due to the presence of a bright source in the 8.0 μm channel, adding to the total offset. We accounted for the offsets due to full-array pull-up and internal scattering by background subtracting all individual frames via user-defined background regions. The background regions were carefully selected to exclude galaxy features, foreground stars, and any data artifacts. Bright features within the galaxy's disk or any bright stars within the frame were the main source of the internally scattered flux, but these features were not part of our extraplanar flux measurements, so removing their redistributed flux from the frame was an acceptable solution.

Background matching via subtraction worked significantly better than utilizing the MOPEX Overlap modules, which tended to introduce a bias across the mosaic. It does not escape our notice that any uniform extraplanar emission would be subtracted off using this method, but we expect such a flux distribution to be unlikely (a test of this background subtraction method is described in § 2.3.4 below).

2.3.1.3 Electronic and Optical Banding

The horizontal (row) electronic and optical banding effect was pervasive in the data and presented a significant challenge in exposures where a galaxy covered a large fraction of the array or in exposures where banding and extraplanar features overlapped. In the course of inspecting the CBCDs, we found that the banding correction applied to the 8.0 μm data by the SSC-contributed code and later versions of the SSC pipeline provided incomplete artifact removal by only addressing the brightest rows.

Since the banding artifacts for extended sources covered a wide range of rows, we developed a PyRAF script to correct individual frames by removing the entire band rather than just the few brightest rows. Our PyRAF script employs user-defined rectangular regions to sample the background and banding artifact regions. It then subtracts a constant value banding offset from each affected row. Overlaid example regions are shown in the left panel of Figure 2.2 and an example result is shown in the right panel.

We also observed a less common, but similarly uniform bias shift in the columns of 8.0 μm images containing a bright source. However, in this case the bias shift was uniformly negative rather than positive. We adapted our PyRAF script and corrected the affected columns.

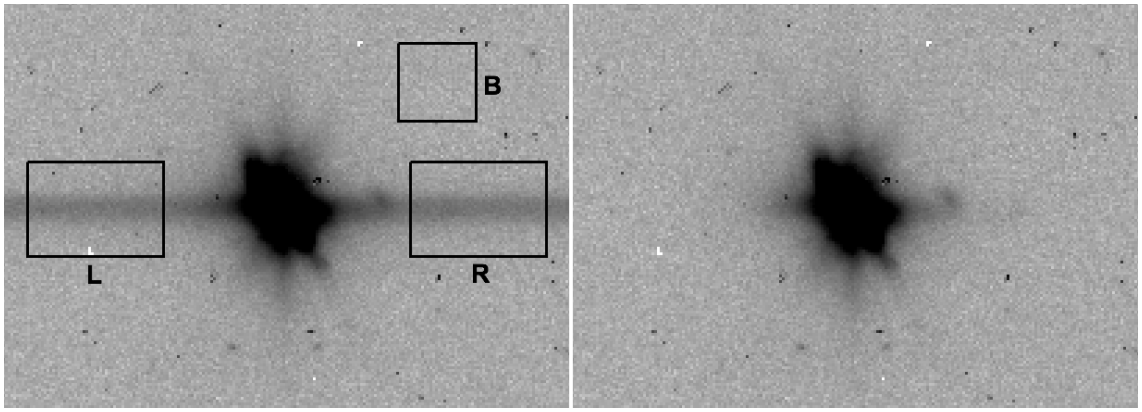

Figure 2.2: Before (left) and after (right) electronic banding correction using our PyRAF script on a single IRAC 8.0 μm frame of NGC 1482. The regions labeled L and R sample the areas affected by the banding artifact and define the rows where the subtraction takes place. The region labeled B samples the background.

2.3.1.4 PSF Fitting and Subtraction

The point spread function (PSF) wings of bright sources can be another locus of confusion with extraplanar emission. Although the galaxies in our sample are not true point sources, several (NGC 1482, NGC 2992, NGC 3079, NGC 3628 and NGC 5253) contain bright, concentrated nuclei, which exhibit PSFs very similar to those produced by bright stars and extend to regions of possible extraplanar emission. In addition, several galaxies (e.g. NGC 1569) have bright foreground stars with prominent PSF wings in close proximity to or overlapping the galaxy's disk. The SSC has produced point response functions (PRFs), which are tables for point source fitting stored as 2-dimensional FITS files and over-sampled to account for intra-pixel sensitivity variations. By sampling the PRFs at the appropriate resolution, we fit and subtracted an estimate of the PSF wings for nuclei and foreground stars using the APEX and APEX QA modules of the SSC-provided MOPEX software.

Since the nuclei of our sample galaxies are not true point sources (the closest being NGC 5253), fitting their wings presented more of a challenge than foreground stars. The bright source generating the PSF is typically spread over several pixels, each with their own intra-pixel variation, leading to smeared wings, which could not be fit well for a single frame with the SSC-provided PRFs. When multiple frames were stacked or mosaicked, that reduced some of the intra-pixel variation, making a fit a bit more straightforward, but we still needed to use a combination of the APEX fitting modules in MOPEX together with some common sense "manual" adjustments, which sometimes meant a segmented model of the source to imitate the smearing. Figure 2.3 shows an example of the fitting challenges.

2.3.2 Aperture Corrections

The IRAC instrument handbook lists extended source photometrical correction factors[3] based on the radius of an effective circular aperture for the flux measurement region. Since our sources are nearby, and all our extraplanar regions cover extended solid angles (> 35"), we applied the infinite, asymptotic correction coefficients: 4.5 μm $\rightarrow$ 0.94 and 8.0 μm $\rightarrow$ 0.740. In order to save a step in our flux measurements, we applied the aperture corrections to the 4.5 and 8.0 μm micron images before the stellar continuum emission subtraction in the next section. Despite these aperture corrections, our flux measurements still have uncertainties at the 10-20% level due to differences in "full-array pull-up" and internal scattering from source to source. We propagated these uncertainties through our calculations.

[3]http://irsa.ipac.caltech.edu/data/SPITZER/docs/irac/iracinstrumenthandbook/30/

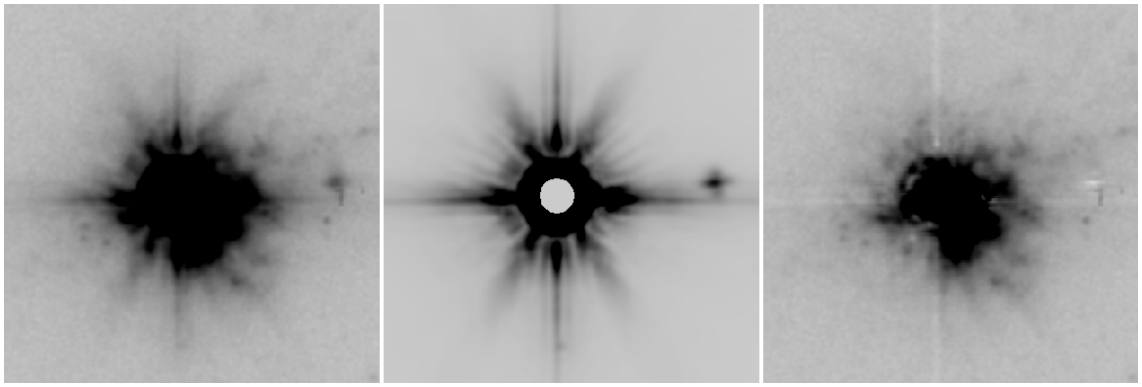

Figure 2.3: PSF fitting and subtraction for NGC 5253 (all IRAC 8.0 μm). The left panel shows the co-added and resampled image. The center panel contains the PSF fitted to the wings of the 8.0 μm image using the SSC-produced extended PRF. The right panel shows the residual image after PSF subtraction (left - center = right). Each panel contains only the central region of these images aligned with their xy-coordinates. The left and right panels are shown on the same scale with a logarithmic stretch, but the center image has a different scale, so it has been clipped and stretched to approximately match the other images. The central region of the fitted PSF was excluded during fitting. In this example, the PSF has been somewhat over-subtracted in certain areas, as shown by the white cross-hairs pattern visible in the right panel. However, other areas seem under-subtracted, such as the area encircling the nucleus. NGC 5253 is not typical of the objects in our sample, but rather illustrates the worst case scenario where the intensity of the PSF is comparable to and overlapping with extraplanar PAH emission. Finally, in the PSF-subtracted image, we can clearly identify extraplanar emission plumes extending toward the lower right corner of the image.

2.3.3 Convolution, Stellar Scaling and Subtraction

Apart from the 7.7 and 8.6-8.8 PAH emission features, other potential contributions to the 8.0 μm band flux include stellar and dust continuum emission, [Ar II] and [Ar III] fine structure lines at 6.985 μm and 8.991 μm respectively, and the H_2 $S(5)$ and H_2 $S(4)$ pure rotational lines at 6.909 μm and 8.026 μm respectively. Smith et al. [2007] included the fine structure lines and H_2 rotational lines in their detailed decomposition of IR spectra from 59 nearby galaxies with a range of star

formation properties, but these lines typically accounted for negligible flux in the 8.0 μm band compared with the contributions of the PAH emission features plus stellar and dust continuum emission. Likewise, these atomic and molecular lines appear comparatively weaker in the nuclei of starburst galaxies [Brandl et al., 2006] as well as within ultraluminous infrared galaxies [Armus et al., 2007, Veilleux et al., 2009a]. In addition, absorption from amorphous silicate centered at 9.7-9.8 μm can attenuate PAH emission at the red end of the 8.0 μm band, particularly the 8.6-8.8 μm PAH feature [Brandl et al., 2006, Smith et al., 2007]. However, the optical depth due to silicate absorption will likely approach zero for extraplanar regions, so we considered it negligible. Similarly, dust continuum emission should be less important in extraplanar regions. Therefore, we focused on accounting for the stellar emission contribution to the 8.0 μm band flux.

First, we convolved the 4.5 μm images to the resolution of the 8.0 μm images using the appropriate convolution kernel as described in Gordon et al. [2008] along with the associated IDL routines[4]. The convolved images and original 8.0 μm images both have a PSF FWHM of $\sim$ 1.9", which is comparable to the 1.22" pixel scale of the IRAC images. As a check, we also generated kernels from the data directly, producing similar flux values after convolution. However, we used the images convolved with the kernels from K. Gordon for our stellar subtraction, since the data-generated kernels tended to over-reduce resolution and compromise the subtraction of individual stars.

Dale et al. [2005] used a conceptually simple approach to model the stellar

[4]http://dirty.as.arizona.edu/~kgordon/mips/conv_psfs/conv_psfs.html

contribution to the SEDs of 75 nearby galaxies. Using a Starburst99 [Leitherer et al., 1999, Vázquez & Leitherer, 2005] model with 900 Myr continous star formation, solar metallicity, and a Salpeter IMF ($\alpha_{IMF} = 2.35$) and dust models essentially parametrized by the far-infrared color $f_\nu(70\ \mu\text{m})/f_\nu(160\ \mu\text{m})$, they found "remarkable" fits to their sample's SEDs. With this method, they estimated the "dust-only" 8.0 and 24 μm fluxes by subtracting an extrapolated stellar contribution scaled from the 3.6 μm flux. Since the 4.5 μm band contains predominantly stellar continuum emission, it can be used along with a scaling factor to estimate the stellar contribution to the 8.0 μm band. Adopting their scaling factors, the extrapolated stellar contribution scaling factor to go from 4.5 to 8.0 μm is $\eta_\nu^{8*} = 0.352$. Thus, in order to obtain fluxes with only 8.0 μm PAH emission, we subtracted the scaled 4.5 μm flux:

$$f_{PAH} \ = \ f_{8.0\mu m} \ - \ \eta_\nu^{8*} f_{4.5\mu m} \tag{2.1}$$

A couple IRAC artifacts tend to redistribute the flux of bright sources, so star subtraction with this method doesn't work as consistently well for bright stars as it does for dimmer stars. When residual stars remained in the extraplanar regions of our stellar continuum-subtracted maps, we masked them out before taking flux measurements (see § 2.4.2). Figure 2.4 shows an example of subtracting the stellar continuum from the data for NGC 891. In subsequent sections, we refer to the stellar continuum-subtracted 8.0 μm maps as PAH images.

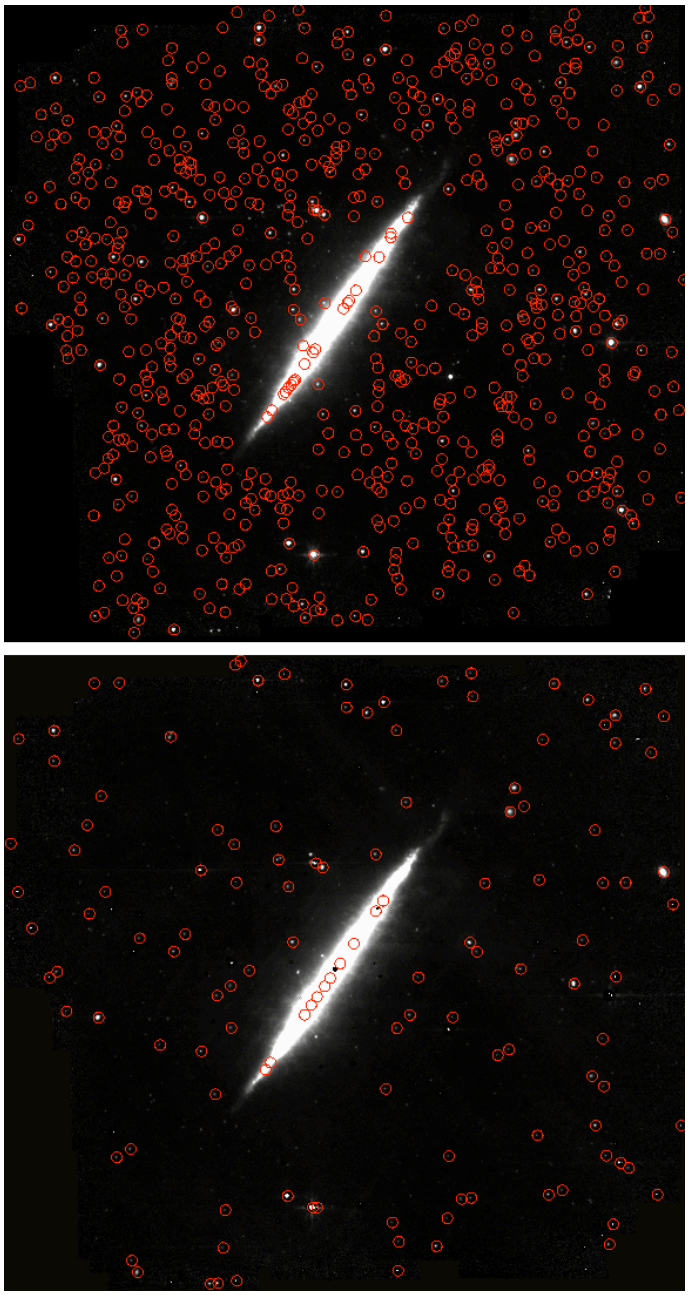

Figure 2.4: Subtraction of the stellar continuum from the data of NGC 891. The top panel shows the IRAC 8.0 μm map with overlaid red circles indicating 718 point sources (excluding those found in the galaxy's disk) detected with the APEX module in the MOPEX software. The bottom panel shows the scaled stellar continuum-subtracted map and 129 overlaid point source detections using the same APEX parameters. Mostly due to IRAC artifacts, the brighter foreground stars tend not to subtract as well, so this is a systematic effect rather than a deficiency in our stellar continuum scaling.

2.3.4 Test of the Background Subtraction

Since measuring diffuse extraplanar flux depends critically on the accuracy of the background subtraction, we tested our method by carefully constructing a model of diffuse extraplanar PAH emission for NGC 891. We chose NGC 891, because (1) it has one of the best behaved edge-on disk morphologies of our sample galaxies, making it simpler to model the underlying stellar disk at 4.5 μm, (2) it is dominated by a very diffuse, nearly featureless extraplanar PAH emission morphology, and (3) it is large on the sky, with the disk subtending more than two full IRAC fields of view. Attributes (2) and (3) make quantifying the extraplanar PAH emission in NGC 891 most challenging, and thus an excellent test case for our methods of data reduction. We modeled the diffuse extraplanar PAH emission as a basic exponential disk:

$$I_{PAH} \; = \; I_0 \; * \; e^{-z/H_z} \; * \; e^{-R/H_R} \tag{2.2}$$

where I_{PAH} is the pixel intensity as a function of z and R, I_0 is the reference intensity, and H_z and H_R are the vertical and radial scale heights with respect to the disk. We chose values of I_0, H_z, and H_R which came close to replicating the morphology of the 8.0 μm data, but with more extended, diffuse flux in the z-direction. We chose a more extended z-direction morphology in order to make it harder to find background reference regions within individual on-source frames.

In order to simulate each individual frame of 8.0 μm data in the same pattern as the observations, we added (1) a scaled 4.5 μm frame, (2) the corresponding 256x256

pixel area from our model, (3) 20-30% (the percentage was chosen at random in that range) of the total flux from the first two components evenly distributed throughout the 256x256 frame, and (4) a constant offset. Components (1) and (2) approximate the source's 8.0 μm flux, while (3) and (4) approximate the behavior of the detector, with component (3) mimicking the "full-array pull-up" plus internal scattering. The 20-30% range was chosen to bracket the $\sim$ 25% value listed in the IRAC instrument handbook.

Next, we performed background subtraction on the individual frames by following the procedure described in § 2.3.1. We made a mosaic of these simulated 8.0 μm frames using MOPEX, performed scaled stellar subtraction, and applied aperture corrections, obtaining a model of diffuse extraplanar PAH emission.

We measured the flux of our modeled diffuse extraplanar PAH emission and recovered $\sim$ 98% of the flux originally contained within the same extraplanar region of the model. This flux loss of $\sim$ 2% is an order of magnitude lower than the $\sim$ 10-20% systematic uncertainty of IRAC flux measurements as listed in the IRAC instrument handbook, so our method of background subtraction has a negligible effect on the measured fluxes. Since our method of background subtraction performed well in the challenging case of NGC 891, we are confident that our reduction also worked well for the other galaxies in our sample.

2.4 Data Analysis

2.4.1 Extent of Extraplanar PAH Features

Measuring the extent of extraplanar PAH emission features gives a basis for comparison to other data such as Hα, X-ray, Na I D, etc. In order to measure the extent of extraplanar PAH features (z_{ext}), we measured perpendicularly from the major axis of the disk to the tip of the feature as it appeared in the 8.0 μm images (before stellar continuum subtraction). We defined the tip of the feature by overlaying a 3σ contour, based on the σ value of the background noise in the 8.0 μm image (as listed in Table 2.2). The projection angles of features are unknown, so our method finds the value of z_{ext} as though it were perpendicular to the line of sight setting an approximate lower limit to the actual size of these features. For cases where the galactic disks are not quite edge-on, the error in our z_{ext} measurement may be larger. Table 2.3 lists the z_{ext} value representing the most extended PAH emission feature for each galaxy.

2.4.2 PAH Flux Measurements

Beyond simply identifying extraplanar PAH emission features, quantifying their flux and comparing with the host galaxy's properties allows us to investigate relationships with star formation and galaxy type. Measuring a value for the extraplanar PAH flux necessitates delineating the disk from the extraplanar region of each galaxy. Factors such as inclination and morphology can complicate this task

somewhat, but our sample consists primarily of disk galaxies with nearly edge-on orientations, simplifying matters.

We wrote a PyRAF script, which determines the vertical scale height (H_z) of a galaxy's stellar disk and from that value generates a disk region. We used the 4.5 μm images (pre-convolution) to generate disk regions based on continuum stellar emission. Before running our script, we rotated the images to align each galactic disk horizontally. Our script first determines a vertical scale height value (H_{col}) for each column of pixels 'above' the disk of the galaxy by fitting a simple exponential:

$$I(z) = I_0 \; e^{-(z-z_{mp})/H_{col}} \quad (\; z \; \geq \; z_{mp} \;) \tag{2.3}$$

where $I(z)$ is the intensity at height z, and I_0 is the intensity where the fit begins. Since the vertical intensity profile plateaus near the midplane of the disk, our script omits this area by using a small offset above the midplane (z_{mp}) for the beginning pixel of the fit. The fit range then extends up to where the intensity has fallen off by $1/e^2$. The script determines a global H_z value by finding the median of all the H_{col} values.

The actual or apparent vertical thickness of the galaxy's stellar component can vary along the disk, especially with a bulge, disk asymmetry, or inclination effects. When measuring the extraplanar flux, the biggest contaminating flux typically comes from the galaxy's bulge. Setting a constant vertical 'edge' based on just H_z can include too much of the central bulge or exclude regions at larger galactic radii which should be considered extraplanar. Therefore, the method in our script for

finding a vertical 'edge' (z_{edge}) needed to account for the bulge and other variations in disk thickness when delineating the disk region.

Starting from our assumption that *to first order*, the vertical light profile will have the same functional shape and H_z value at all galactic radii, the exponential profile in equation 2.3 will simply shift in the z-direction based on the value of I_0. Consider two columns which reach the same $I(z)$ at different values of z - say one at large galactic radius where the projected disk intensity is low (I_1) and one near the nucleus where the projected disk intensity is high (I_2):

$$I(z) = I_1 \; e^{-(z_1 - z_{mp})/H_z} \tag{2.4}$$

$$I(z) = I_2 \; e^{-(z_2 - z_{mp})/H_z} \tag{2.5}$$

where z_1 and z_2 ($z_1 < z_2$) are the different heights at which the intensity reaches $I(z)$. If we define the shift in the z-direction as $z_s = z_2$ - z_1, then

$$z_s \;=\; H_z \ln\left(\frac{I_2}{I_1}\right) \tag{2.6}$$

Thus the shift of the exponential profile in the z-direction should depend only on the ratio (I_2 / I_1) and H_z, which we've assumed to be constant for the entire disk.

Therefore our script determines the edge of the disk region, z_{edge}, by combining the offset at the midplane (z_{mp}) with a multiple of H_z and a term to account for the intensity profile shift in the z-direction due to a bulge or other variations in disk thickness:

$$z_{edge} = z_{mp} + 3H_z + A \ln\left(\frac{I_{bin}}{I_*}\right) \tag{2.7}$$

where A is a distance constant determined by trial, I_{bin} is the median I_0 within a bin along the major axis of the disk, and I_* is the unit intensity in MJy sr^{-1}. The bin size is chosen to reflect a balance of disk feature size and image resolution constraints. The factor of 3 represents a typical value for the ratio of the thick disk to the thin disk [e.g., de Grijs & Peletier, 1997], since our method typically finds the vertical scale height of the thin disk. Including each galaxy's H_z value within the shift term as suggested by equation 2.6 produced inconsistent results, often underestimating or overestimating the disk edge. Instead, we adopted the distance constant A, which we found by iteratively running our script with different constant values in order to appropriately scale the shifts of all bins. We use the same unit intensity I_* as the reference value within the shift term for all galaxies in order for the z-direction shift to depend only on the relative values of I_{bin} (i.e. the intensity variation within the disk). Figure 2.5 shows an example of vertical scale height fits to the 4.5 μm surface brightness profile above and below the midplane of NGC 891.

The midpoint of the bin and z_{edge} are then the (x,y) coordinates of a point on the edge of the disk region. Once these coordinates are determined for all the bins 'above' the midplane, the script then repeats the fitting process 'below' the midplane and generates a polygonal disk region by connecting points sequentially. Our method for determining z_{edge} is purposefully conservative to make sure disk regions include the thick disk and bulge, so our extraplanar flux measurements may

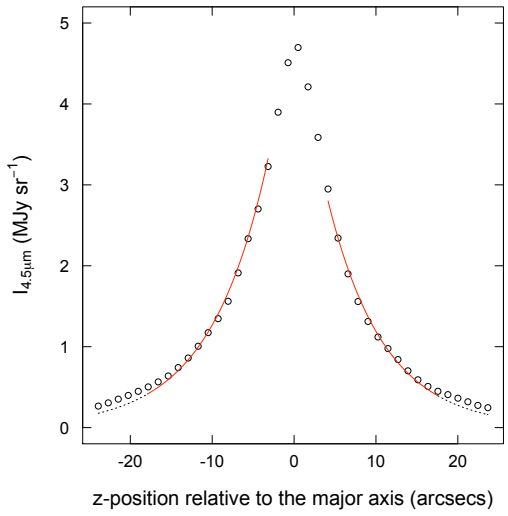

Figure 2.5: Scale height fitting to the vertical surface brightness profile (single column of pixels) of NGC 891 using the 4.5 μm data. The data are shown as black open circles. The solid red lines describe the individual exponential profiles fit to the thin disk above and below the midplane. The extent of the solid red lines indicates which pixels were used in the fits. A few central pixels near the midplane were excluded from the fits, since the profile turns over at the midplane. The dotted extension of each fit to z-positions further from the midplane illustrates the transition to the thick disk as $|z|$ increases.

be lower limits. Figure 2.6 shows an example of the disk region generated with this method for NGC 4388.

For the six galaxies in our sample with lower inclination or less disk-like morphology (NGC 253, NGC 1705, NGC 1808, NGC 2992, NGC 4945, and NGC 5253), our method for finding a vertical scale height does not work. Therefore, we used a disk region defined by the 20σ contour of the 4.5 μm image, where σ is the standard deviation of the background noise (see Table 2.2). As a check on the validity of this method to characterize the disk region, we compared the 20σ contour to the disk region for galaxies where we were able to fit a vertical scale height. The results produced spatially similar regions with a typical flux difference from one region to

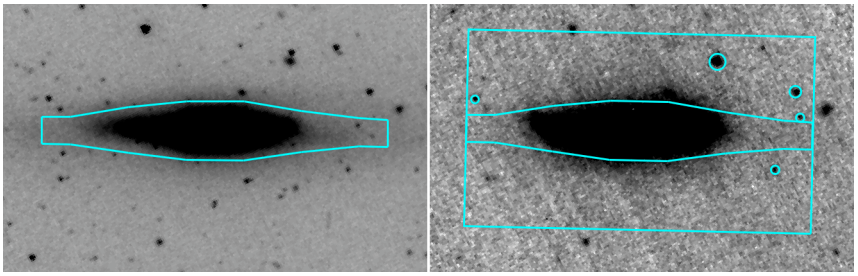

Figure 2.6: Extraplanar PAH flux calculation for NGC 4388. The left panel shows the IRAC 4.5 μm image with the disk region generated by scale height fitting. The right panel shows the IRAC 8.0 μm PAH emission image with the disk, mask and extraplanar regions overlaid. North is up, east is left in both images.

the other of less than $\sim 5\%$.

Overlaying the disk regions onto the PAH images, we chose rectangular regions with the same radial extent as the disk regions to enclose any extraplanar emission, but exclude features that might be due to tidal interactions (e.g. NGC 2992). Exceptions are NGC 1569, which has some extraplanar emission in a radial direction and NGC 1705, which has relatively low inclination and peculiar morphology. In several cases, artifacts or field stars remained in the PAH images, so these were masked out wherever possible. All images were background-subtracted prior to the flux calculations. Figure 2.7 shows all sample galaxies with disk, 20σ, extraplanar, and mask regions overlaid.

The extraplanar PAH flux (f_{ePAH}) was calculated by subtracting the disk and mask regions' flux from the extraplanar region's flux for each aperture corrected 8.0 μm PAH emission image (stellar continuum-subtracted):

$$f_{ePAH} = \left[\sum_{pixels} (I_{ext}) - \sum_{pixels} (I_{disk}) - \sum_{pixels} (I_{mask}) \right] d\Omega \qquad (2.8)$$

where I_{ext}, I_{disk} and I_{mask} are the specific intensities in MJy sr^{-1} of pixels in the

rectangular extraplanar region, disk region, and mask region(s), respectively, and $d\Omega$ is the pixel scale in steradians. The values of f_{ePAH} are listed in Table 2.3.

2.4.3 Characteristic PAH Properties

Quantifying the extraplanar PAH emission's characteristic height above the disk provides another avenue for comparison with galaxy properties. In order to arrive at a characteristic height, we first defined a characteristic specific intensity of the extraplanar PAH emission (I_{ePAH}) by finding the median pixel value of the extraplanar PAH emission (extraplanar - disk - mask) from the PAH images. We removed any potential biasing due to noise by taking the median from a subset of extraplanar emission pixels, clipped to only include pixel values 3σ above the background noise. Figure 2.8 shows an example of contours at 3σ above the background and at the calculated value of I_{ePAH} overlaid onto the PAH image of NGC 6810.

We also define a stellar disk diameter, $D_{4.5\mu m}$, taken as the major axis of a 0.175 MJy sr^{-1} contour on the IRAC 4.5 μm image. D_{25} is linearly related to $D_{4.5\mu m}$, as shown in Figure 2.9. Taking I_{ePAH} together with $D_{4.5\mu m}$ and the total extraplanar flux, f_{ePAH}, we define the extraplanar PAH emission characteristic height as

$$H_{ePAH} = \frac{f_{ePAH}}{2\ I_{ePAH}\ D_{4.5\mu m}} \tag{2.9}$$

H_{ePAH} can be imagined conceptually as the height of a rectangular region with all pixel values equal to I_{ePAH}, width $D_{4.5\mu m}$, and total flux $f_{ePAH}/2$. The factor of 2 arises, since f_{ePAH} includes flux from above and below the disk. The measured and

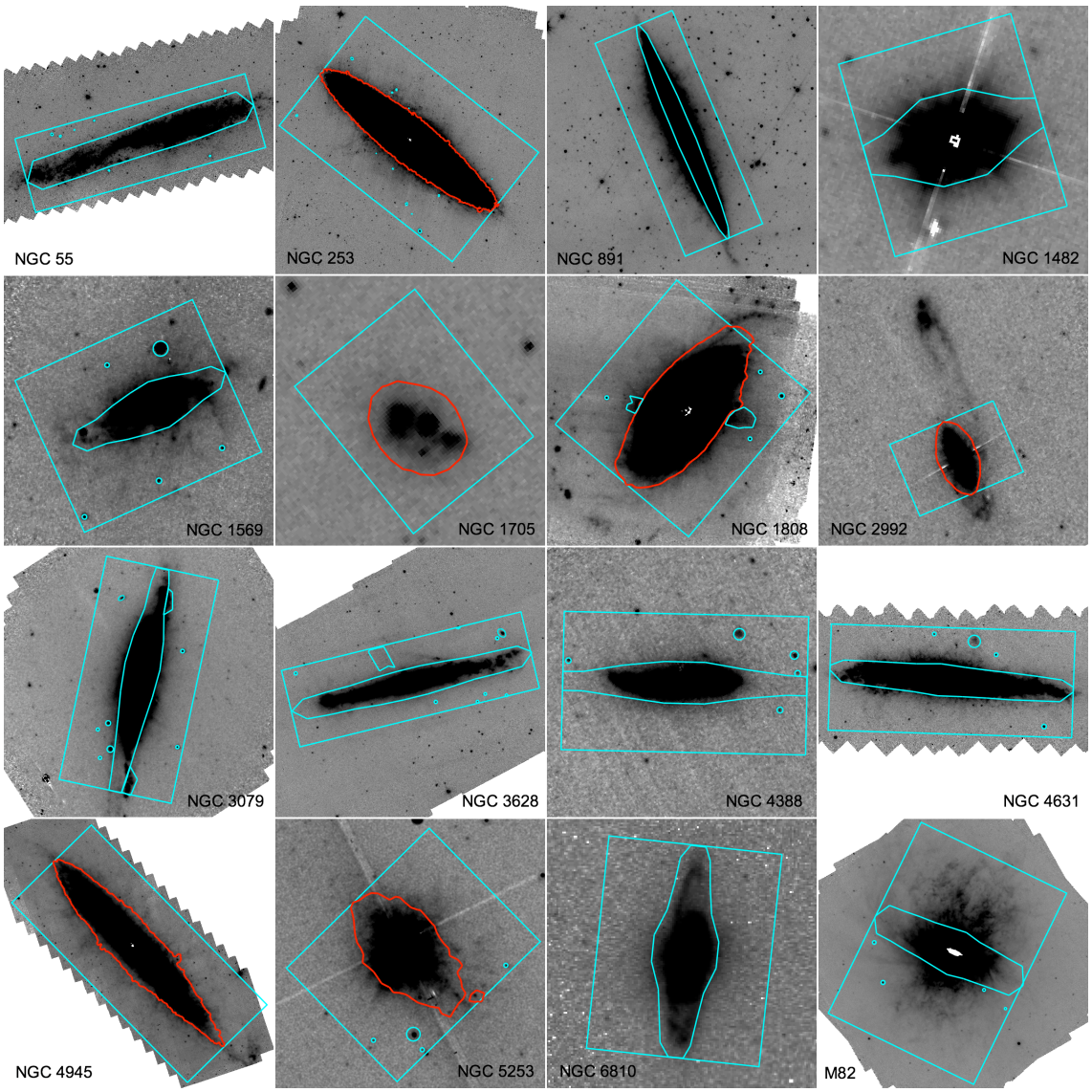

Figure 2.7: Regions used to determine the flux of the extraplanar PAH emission: IRAC 8.0 μm maps overlaid with the disk, 20σ, mask, and extraplanar regions as described in § 2.4.2. 20σ contours are shown in red. Note that 20σ and disk regions were generated from the IRAC 4.5 μm images, so the 8.0 μm disk emission will often differ significantly in spatial extent (e.g. M82). The intensity scalings are logarithmic. North is up and east is left in all images.

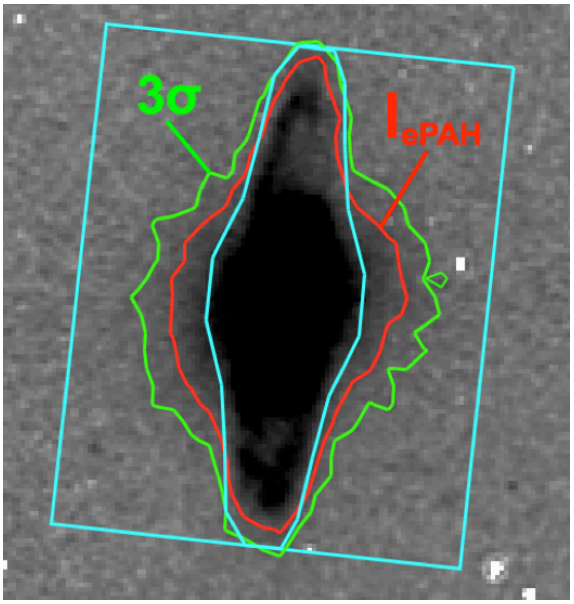

Figure 2.8: Determining the characteristic extraplanar emission height, H_{ePAH}. The overlaid map is the PAH image of NGC 6810. The green contour is 3σ above the background, and the red contour follows the characteristic intensity value, I_{ePAH}. The cyan regions are the disk and extraplanar regions. The intensity scaling of the overlaid image is logarithmic. North is up and east is left.

calculated values of I_{ePAH}, $D_{4.5\mu m}$, and H_{ePAH} are listed in Table 2.3.

H_{ePAH} behaves essentially like a measure of the extraplanar PAH emission's bulk height. Since it contains both a measure of the vertical distribution of the emission (I_{ePAH}) and a measure of the emission's width compared to the disk (contained within f_{ePAH}), H_{ePAH} is most sensitive to their ratio. $D_{4.5\mu m}$ is less important to the behaior of H_{ePAH}, since f_{ePAH} also depends somewhat on the galaxy's diameter. We illustrate the behavior of H_{ePAH} under different scenarios in Figure 2.10.

In order to compare H_{ePAH} with the star formation properties of the host galaxy, we converted L_{IR} into SFR using equation 3 from Kennicutt [1998]:

$$\frac{SFR}{1\ M_\odot\ yr^{-1}} = \frac{L_{IR}}{5.8 \times 10^9\ L_\odot} \tag{2.10}$$

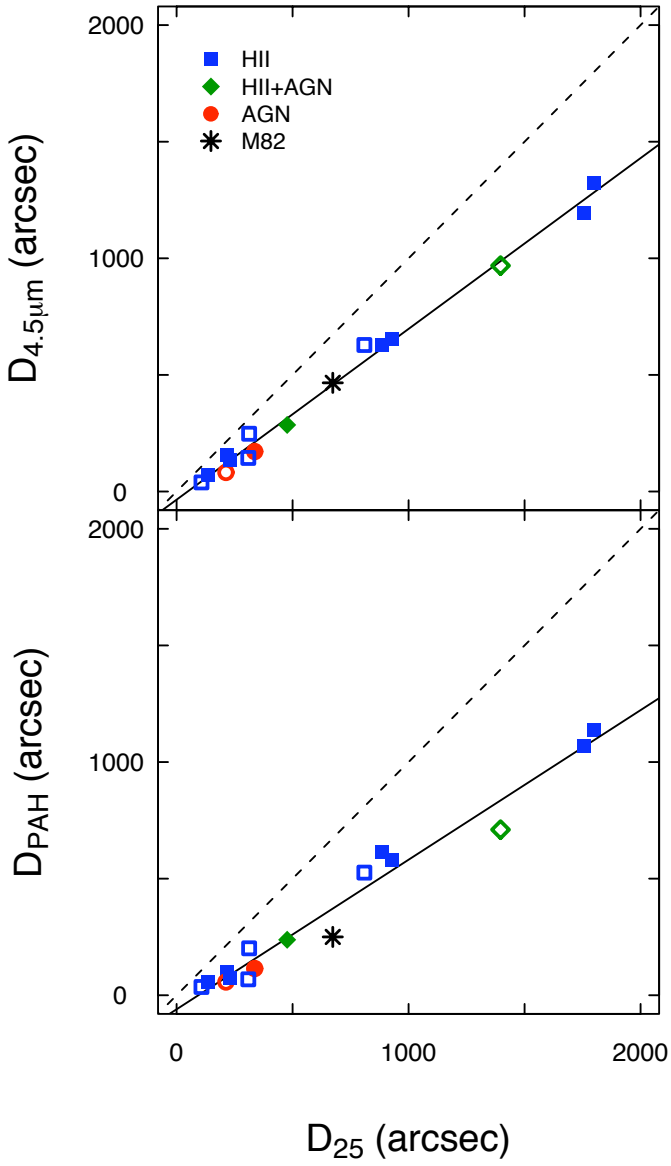

Figure 2.9: Comparisons of the mid-infrared and optical diameters: the major axis in the IRAC 4.5 μm images at the 0.175 MJy sr^{-1} contour ($D_{4.5\mu m}$) and characteristic PAH diameter (D_{PAH}, see § **??**) versus major axis in B-band images at apparent magnitude $m = 25$ (D_{25}). Meaning of the symbols is the same as in Figure 2.1. The solid lines in the top and bottom panels are linear fits with slopes $\alpha = 0.73$ and $\alpha = 0.64$, respectively. The dashed lines shows the 1-to-1 relationship for reference.

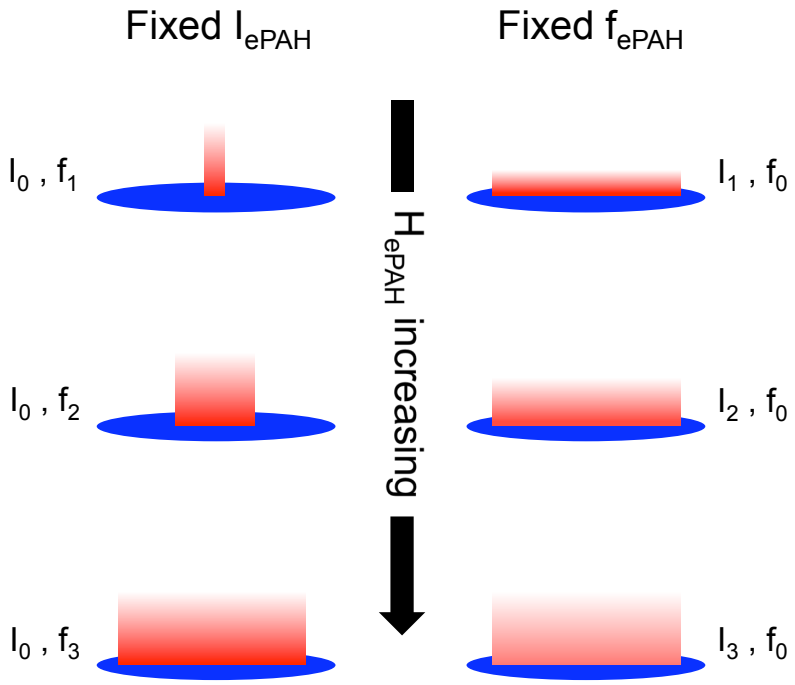

Figure 2.10: The behavior of the characteristic extraplanar PAH emission height, H_{ePAH}, under different scenarios. Blue ellipses represent the stellar disk of the galaxy, and the rectangular red gradients represent the extraplanar emission. Left: for fixed values of the characteristic extraplanar intensity, I_{ePAH}, larger values of total extraplanar PAH flux, f_{ePAH} ($f_1 < f_2 < f_3$) produce larger values of H_{ePAH} (same vertical profile, but more width). Right: for fixed values of f_{ePAH}, smaller values of I_{ePAH} ($I_1 > I_2 > I_3$) produce larger values of H_{ePAH} (same width and total flux, but graduated vertical profile).

Then using this value along with the D_{25} value (see Table 2.1), we calculated the SFR surface density:

$$\Sigma_{SFR} = \frac{4\ SFR}{\pi\ {D_{25}}^2} \tag{2.11}$$

We list the Σ_{SFR} values in Table 2.3.

Since Σ_{SFR} measures an average over the entire stellar disk while star formation tends to concentrate in certain regions, a global calculation will typically underestimate SFR surface density. Therefore we developed a measurement of SFR

surface density, which includes quantification of the star formation location and distribution. In doing so, we used the 8.0 μm band emission as an approximate, though imperfect, tracer of star formation rather than the 24 μm band emission, which is often used as such a tracer [Calzetti et al., 2007]. The archival MIPS data for our sample suffers from lower resolution, bright (sometimes saturated) PSFs that overwhelm or significantly cover some galaxies making reliable disk diameters tricky to obtain, other detector artifacts that complicate photometry, and strong contamination from the AGN in some objects. These characteristics make the 24 μm band less useful than 8.0 μm in determining SFR surface density for our sample.

Using the same algorithm for finding I_{ePAH}, we found the characteristic specific intensity within the disk region of the 8.0 μm images. Although the nuclear regions of some images were compromised by the data reduction process, only small groups of pixels are affected compared to the total numbers in the disks, so they have a negligible effect on the median disk pixel value. Overlaying a contour at this value approximately outlines the densest region or regions of star formation. The contour produced alternatively a concentrated region surrounding the nucleus (e.g. NGC 6810, M82), a region spanning nearly the entire disk (e.g. NGC 4945), or several distinct regions and clumps within the disk (e.g. NGC 55, NGC 3628). Measuring the diameter of a single region or summing the diameters of multiple regions parallel to the galaxy's major axis, we obtained a characteristic diameter of PAH emission in the disk, D_{PAH}. We then used D_{PAH} to calculate a characteristic SFR surface density (Σ'_{SFR}). The values of D_{PAH} and Σ'_{SFR} are listed in Table 2.3, and D_{PAH} is plotted versus D_{25} in Figure 2.9. As a test to justify our use of D_{PAH}, we also

Table 2.3: IR Luminosity and Extraplanar PAH Emission

Galaxy	Type	F_{IR} [1]	L_{IR} [2]	f_{ePAH} [3]	$D_{4.5\mu m}$ [4]	I_{ePAH} [5]	H_{ePAH} [6]	Σ_{SFR} [7]	D_{PAH} [8]	Σ'_{SFR} [9]	z_{ext} [10]
NGC 55	H II	3.24	0.026	0.120	9.3	0.075	0.227	0.0003	8.3	0.0008	1.0
NGC 253	H II	92.5	3.440	0.677	22.2	0.107	1.709	0.0083	19.1	0.0207	5.2
NGC 891	H II	8.12	2.324	0.388	29.2	0.082	7.095	0.0036	24.5	0.0085	6.0
NGC 1482	H II	3.20	3.822	0.025 :	6.7	0.188	3.113 :	0.0523	5.2	0.3083	4.1
NGC 1569	H II	4.66	0.163	0.059	2.5	0.280	0.384	0.0285	1.6	0.1420	0.8
NGC 1705	H II	0.110	0.009	0.001	1.0	0.075	0.090	0.0028	0.9	0.0255	...
NGC 1808	H II	10.3	4.863	0.106 :	14.8	0.130	4.079 :	0.0307	12.0	0.0741	6.0
NGC 2992	AGN	0.984	2.939	0.004 :	12.3	0.119	1.382 :	0.0063	8.6	0.0869	3.9
NGC 3079	H II + AGN	5.19	6.580	0.079	28.0	0.148	3.260	0.0066	23.3	0.0266	5.5
NGC 3628	H II	5.66	2.836	0.083 :	38.7	0.110	1.270 :	0.0021	37.8	0.0044	5.0
NGC 4388	AGN	1.36	1.181	0.010	13.9	0.176	0.447	0.0035	9.3	0.0301	2.1
NGC 4631	H II	8.93	1.612	0.215 :	24.1	0.149	1.547 :	0.0030	21.5	0.0077	3.8
NGC 4945	H II + AGN	63.6	2.493	0.626	16.7	0.236	1.072	0.0095	12.2	0.0366	2.9
NGC 5253	H II	3.71	0.164	0.015 :	2.6	0.167	0.309 :	0.0113	1.2	0.2306	0.9
NGC 6810	H II	2.07	5.299	0.034	19.0	0.380	1.912	0.0114	10.0	0.1160	5.3
M82	H II	144	5.563	4.055	8.0	0.333	9.120	0.0920	4.3	0.6666	6.0

[1,2] The IR flux [10^{-9} erg s^{-1} cm^{-2}] and luminosity [10^{10} $L_{\odot}$] calculated using equations in Table 1 of Sanders & Mirabel [1996], IRAS flux densities listed in the NASA/IPAC Extragalactic Database [Moshir et al., 1990, Sanders et al., 2003], and the distances listed in Table 2.1.

[3] Extraplanar 8.0 μm PAH flux [Jy] measured as described in § 2.4.2. The uncertainties for the flux values are within ∼10-20% (systematic photometric uncertainty) and values followed by a : fall within ∼20-40% (systematic photometric uncertainty plus persistent artifacts). Flux uncertainties also apply to the corresponding H_{ePAH} values.

[4] Major axis [kpc] in the IRAC 4.5 μm images at the 0.175 MJy sr^{-1} contour.

[5] Characteristic intensity of extraplanar PAH emission [MJy sr^{-1}], see § 2.4.3.

[6] Characteristic height of extraplanar PAH emission [kpc], see § 2.4.3. Uncertainty percentages are the same as in 3.

[7] SFR surface density [$M_{\odot}$ yr^{-1} kpc^{-2}] calculated using L_{IR} and D_{25}, see § 2.4.3.

[8] Characteristic diameter of PAH emission (8.0 μm) in the disk [kpc] used to parametrize the location and distribution of star formation.

[9] Characteristic SFR surface density [$M_{\odot}$ yr^{-1} kpc^{-2}] calculated using L_{IR} and D_{PAH}, see § 2.4.3.

[10] The furthest extent [kpc] of any PAH features projected perpendicular to the galaxy's major axis, see § 2.4.1.

compared best-estimate, non-photometric 24 μm diameters for the seven galaxies where we could measure them with each galaxy's D_{PAH} value and found a one-to-one correlation to within $\sim$ 10%.

2.5 Results and Discussion

We find extraplanar PAH emission features in all but one galaxy. The only exception, NGC 1705, has the least favorable orientation ($i = 42°$) of our sample galaxies. The maximum extent (z_{ext}) of the features ranges from $\sim$ 0.8 kpc (NGC 1569, NGC 5253) up to $\sim$ 6.0 kpc (NGC 891, NGC 1808, and M82). The extraplanar PAH emission features have varied morphology and spatial distribution relative to their host galaxies. Figures 2.11 - 2.20 show comparisons of the 4.5 and 8.0 μm images for each galaxy. Appendix A contains a discussion of the PAH features for

each individual galaxy.

The location and morphology of extraplanar PAH features often strongly suggests where they originated. In some cases, filaments or plumes appear to extend from the galaxy's nucleus (e.g. NGC 1482, NGC 2992), while other galaxies exhibit features extending from locations spread throughout the disk (e.g. NGC 891, NGC 4631 and NGC 4945). In each of these cases, the extraplanar features extend up from the disk, but also tend to splay outward radially. This morphology suggests a radially decreasing density gradient in the ISM at the point of origin. Some evidence exists for isolated extraplanar features at locations far from the nucleus (e.g. NGC 3628), but these appear to be outliers. For some galaxies (e.g. NGC 2992 and NGC 3628), the morphology, location, and orientation of particular PAH features indicates tidal disruption rather than wind-driven origins.

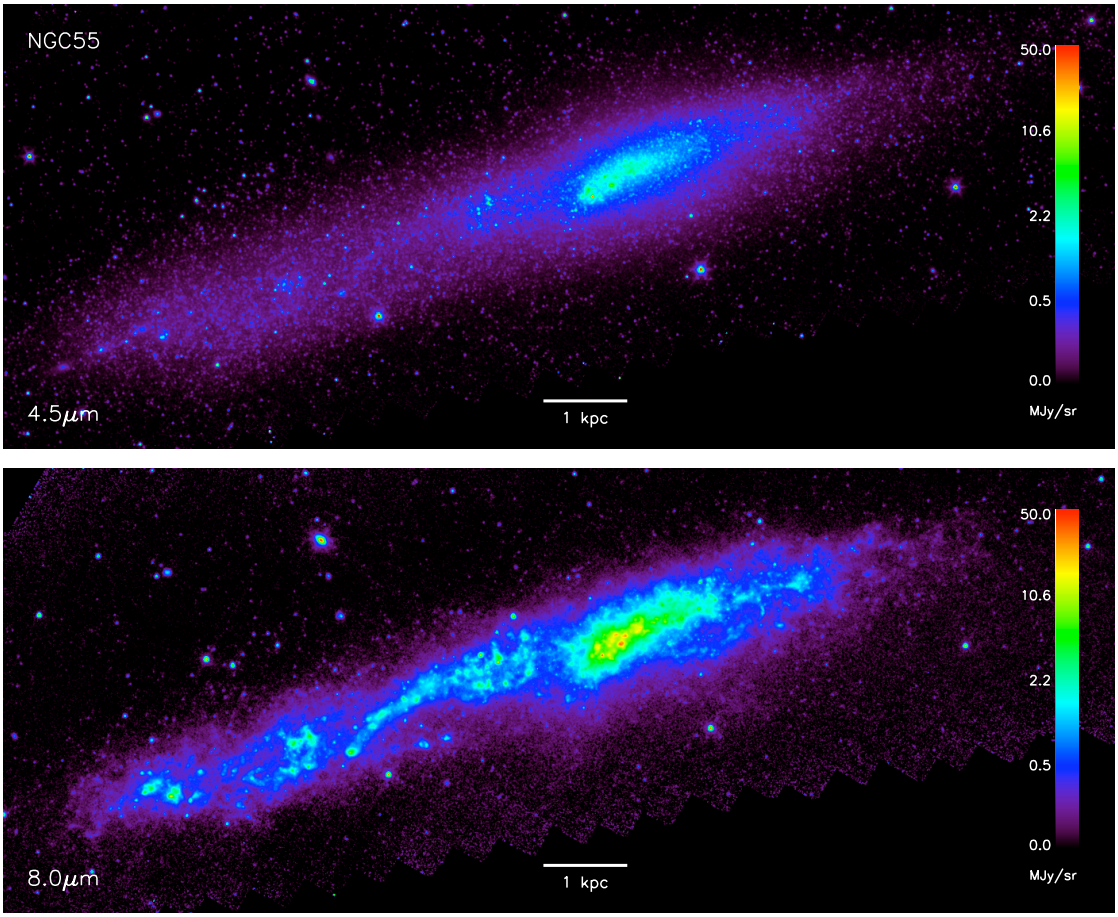

Figure 2.11: Comparing IRAC 4.5 and 8.0 μm maps of NGC 55. The images are displayed with the "asinh" (inverse hyperbolic sine) scaling from Lupton et al. [1999], which has approximately linear scale in the low flux range and approximately logarithmic scale in the high flux range. This scaling allows faint features to stand out without obscuring structure in the brighter regions. North is up and east is left in both images.

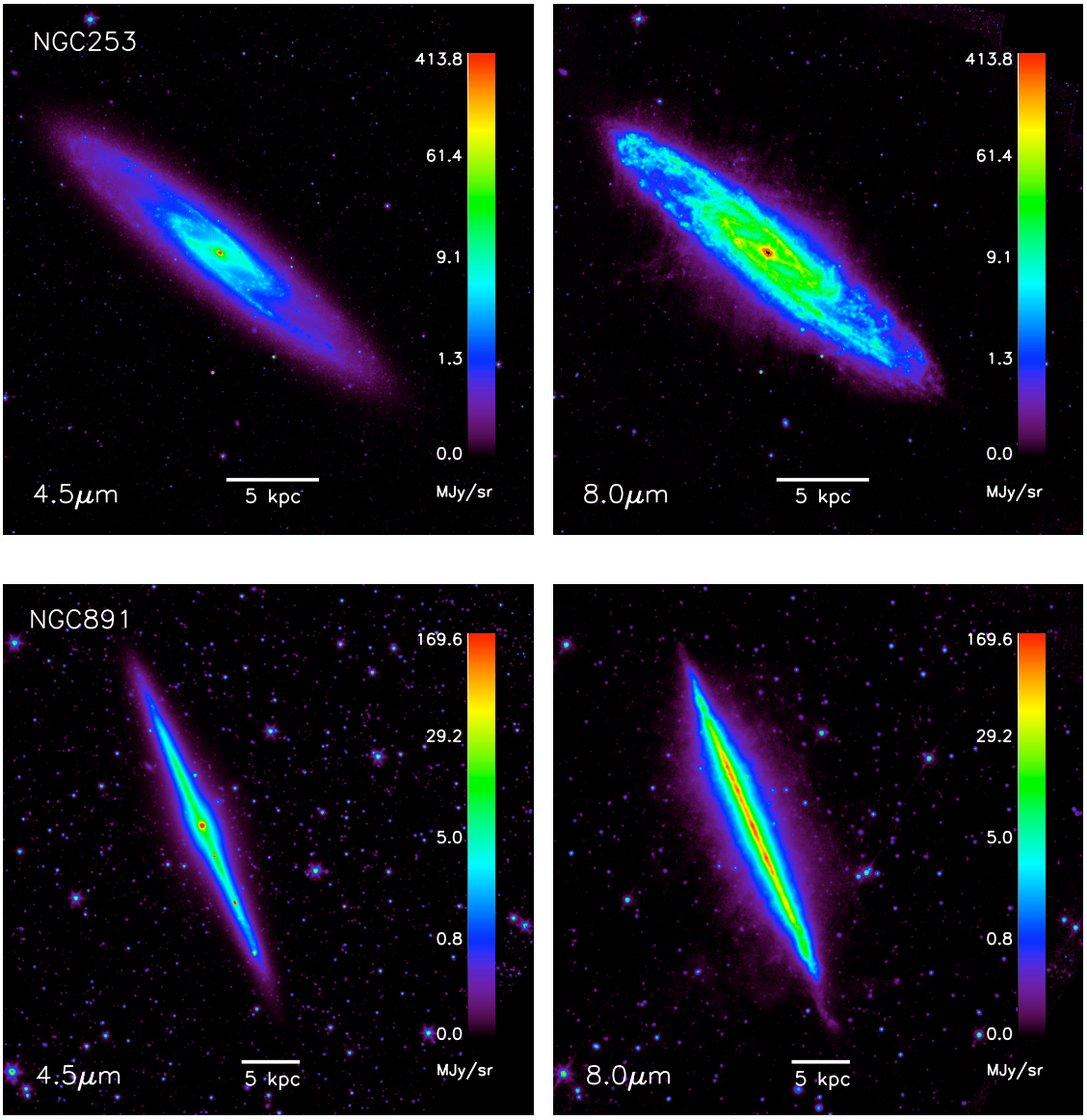

Figure 2.12: Comparing IRAC 4.5 and 8.0 μm maps of NGC 253 and NGC 891. The intensity scalings are "asinh" as described in Figure 2.11. North is up and east is left in all images.

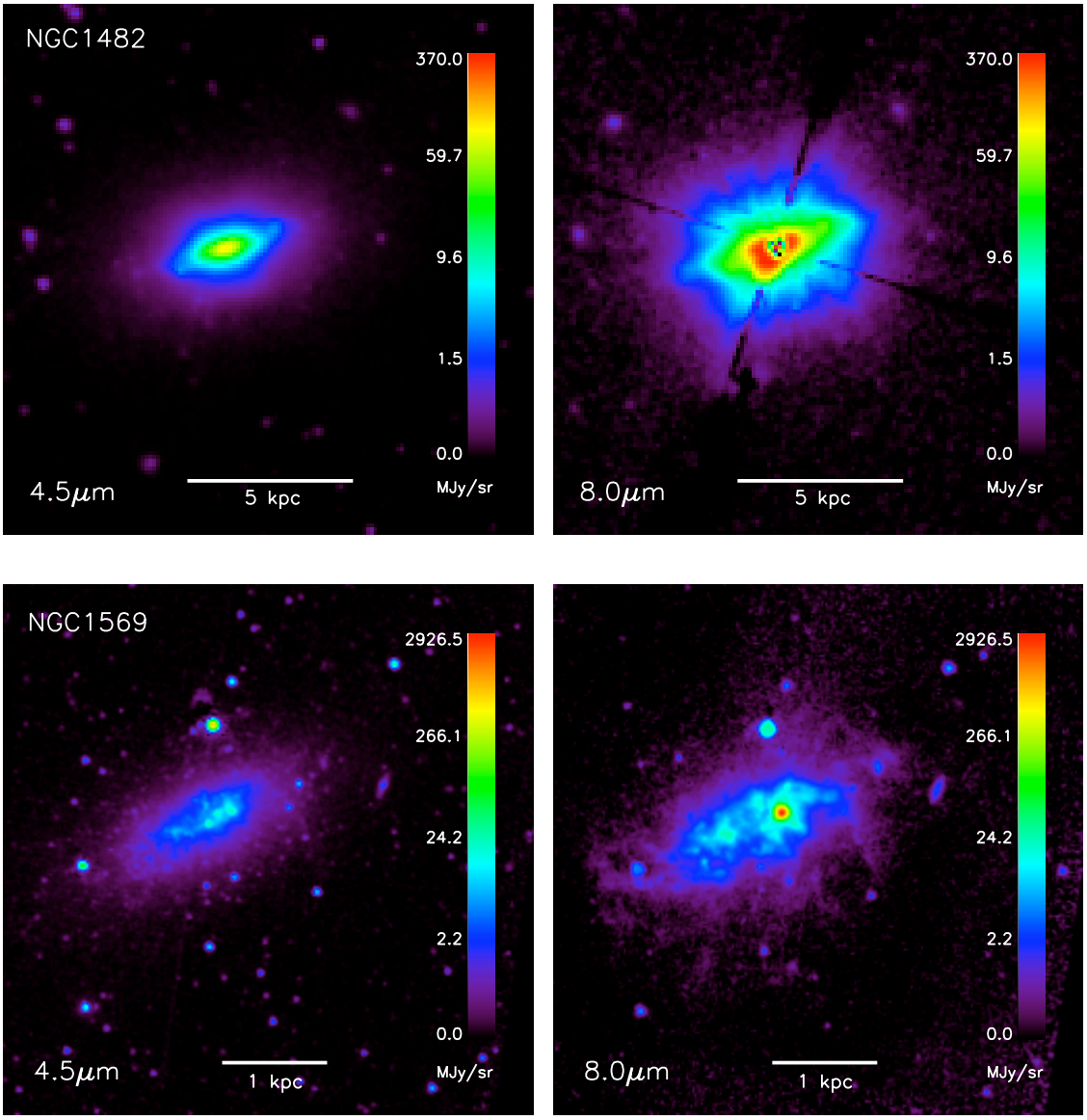

Figure 2.13: Comparing IRAC 4.5 and 8.0 μm maps of NGC 1482 and NGC 1569. The intensity scalings are "asinh" as described in Figure 2.11. North is up and east is left in all images.

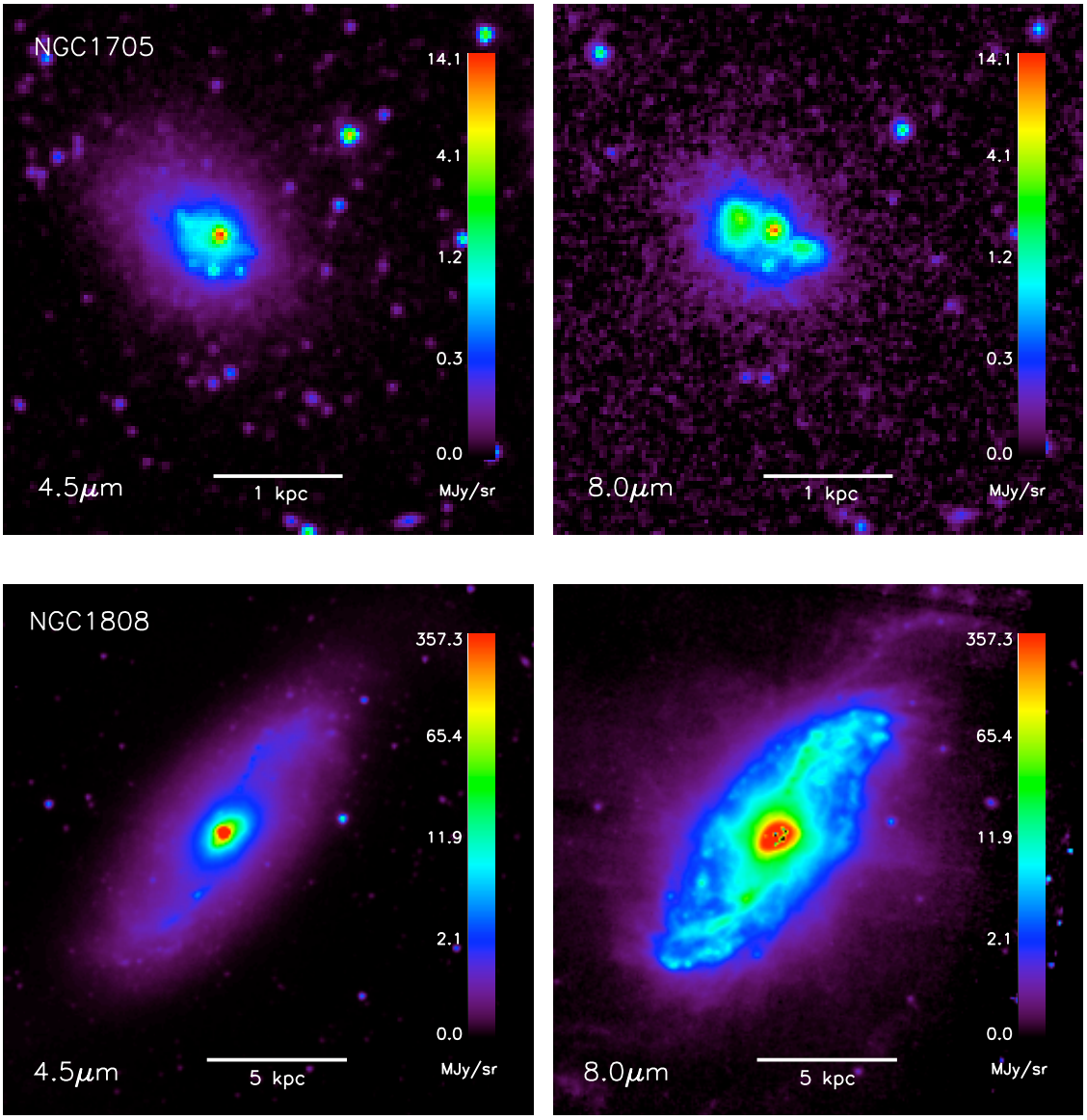

Figure 2.14: Comparing IRAC 4.5 and 8.0 μm maps of NGC 1705 and NGC 1808. The intensity scalings are "asinh" as described in Figure 2.11. North is up and east is left in all images.

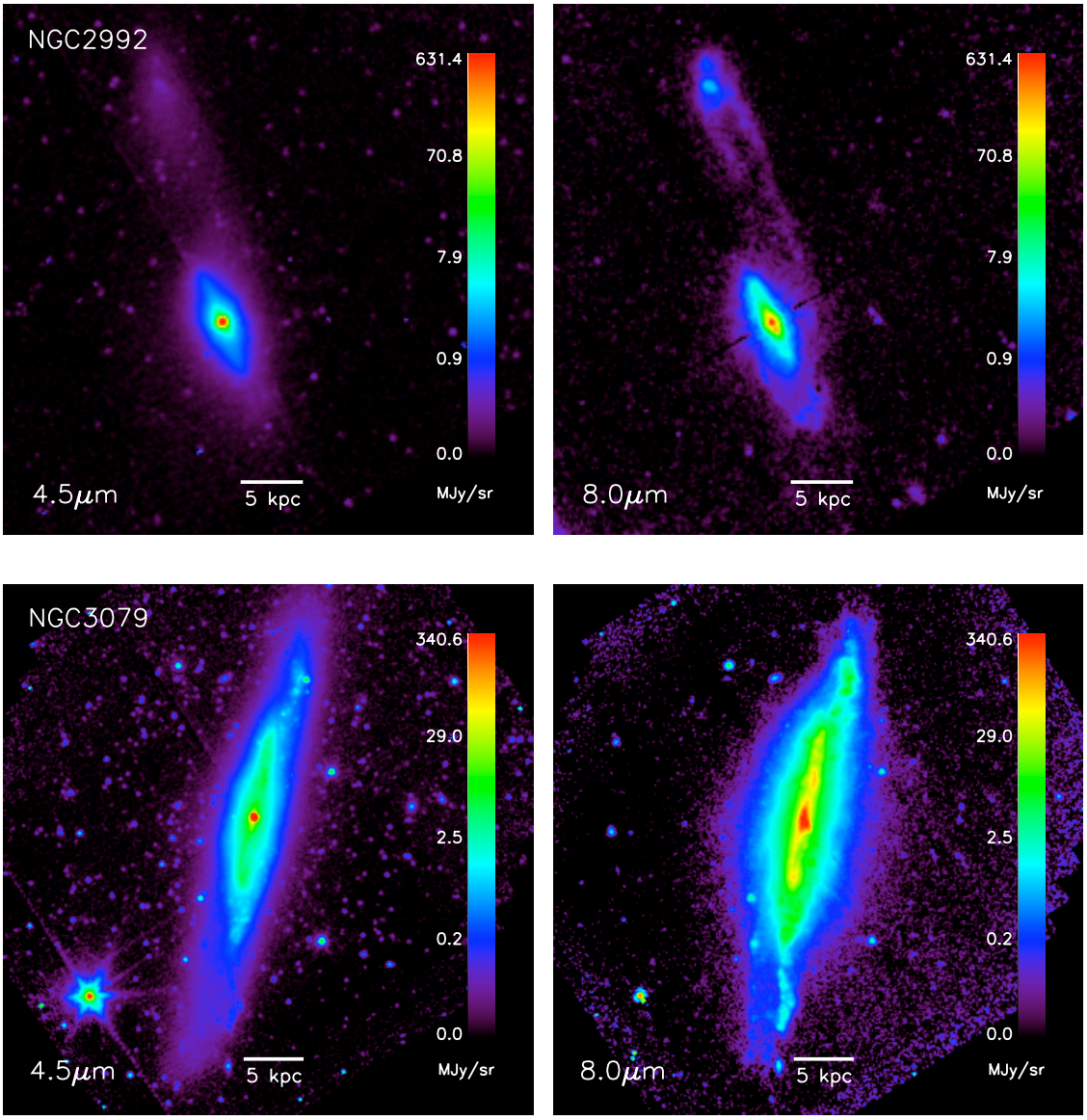

Figure 2.15: Comparing IRAC 4.5 and 8.0 μm maps of NGC 2992 and NGC 3079. The intensity scalings are "asinh" as described in Figure 2.11. North is up and east is left in all images.

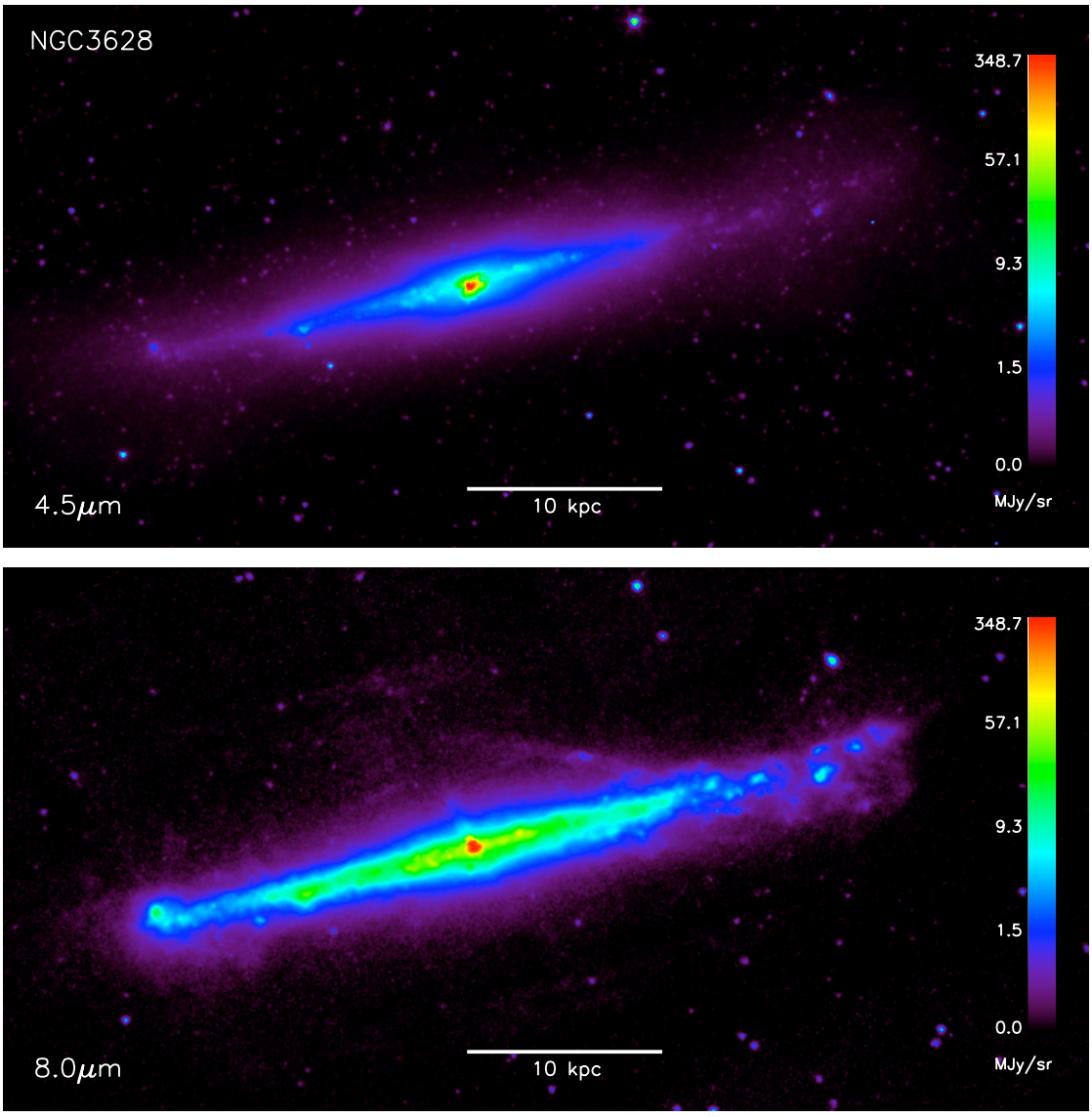

Figure 2.16: Comparing IRAC 4.5 and 8.0 μm maps of NGC 3628. The intensity scalings are "asinh" as described in Figure 2.11. North is up and east is left in both images.

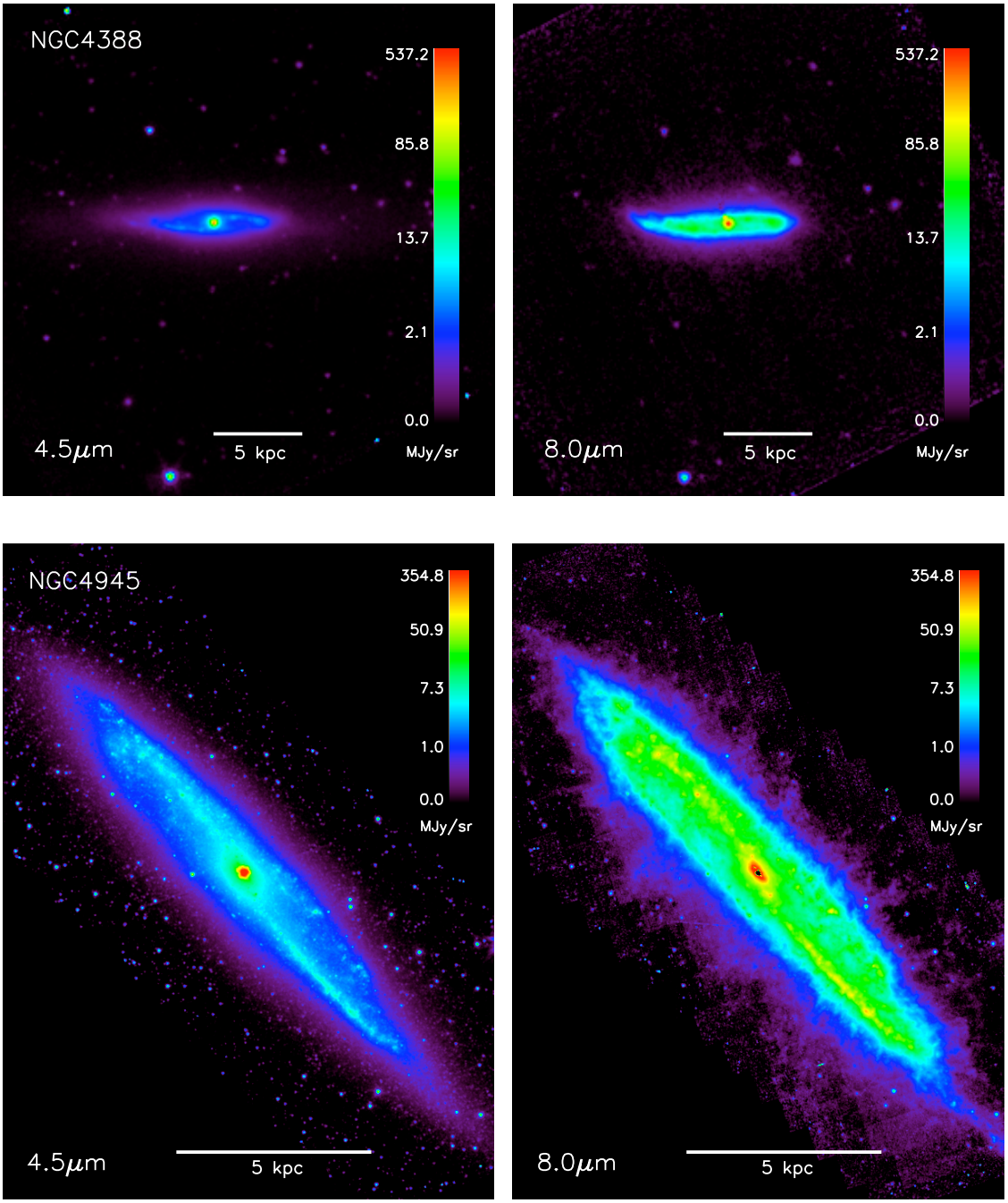

Figure 2.17: Comparing IRAC 4.5 and 8.0 μm maps of NGC 4388 and NGC 4945. The intensity scalings are "asinh" as described in Figure 2.11. North is up and east is left in all images.

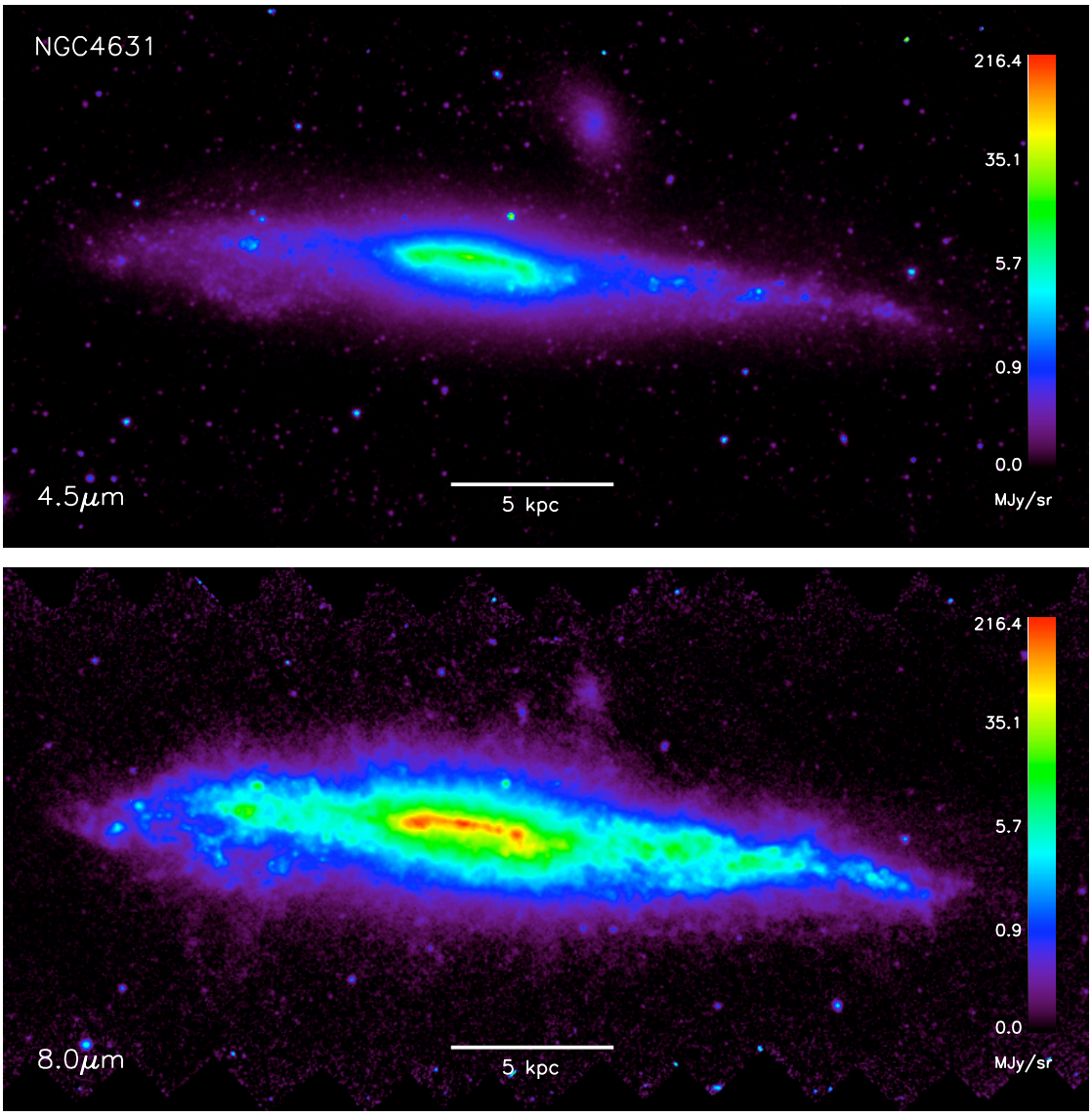

Figure 2.18: Comparing IRAC 4.5 and 8.0 μm maps of NGC 4631. The intensity scalings are "asinh" as described in Figure 2.11. North is up and east is left in both images.

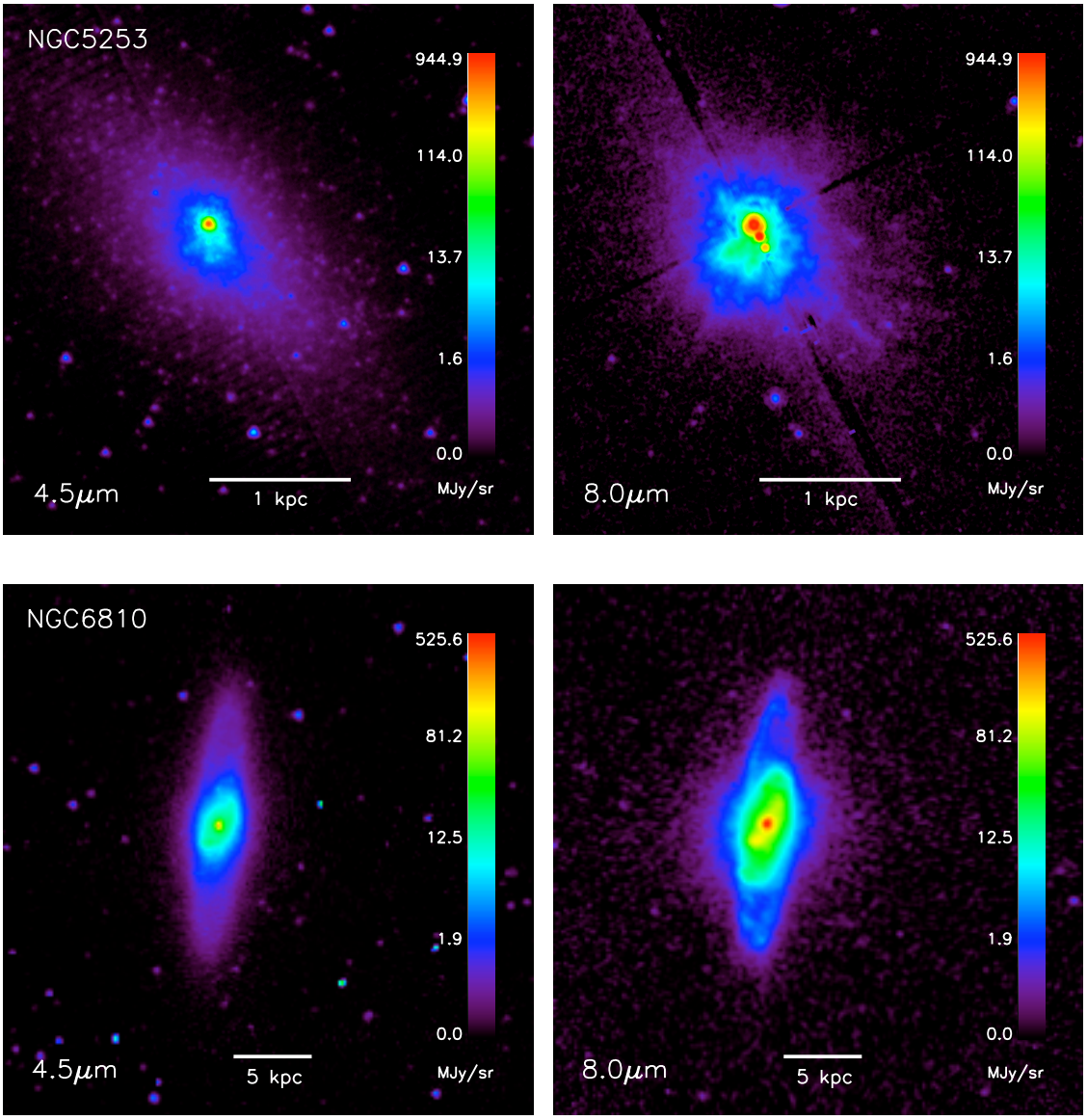

Figure 2.19: Comparing IRAC 4.5 and 8.0 μm maps of NGC 5253 and NGC 6810. The intensity scalings are "asinh" as described in Figure 2.11. North is up and east is left in all images.

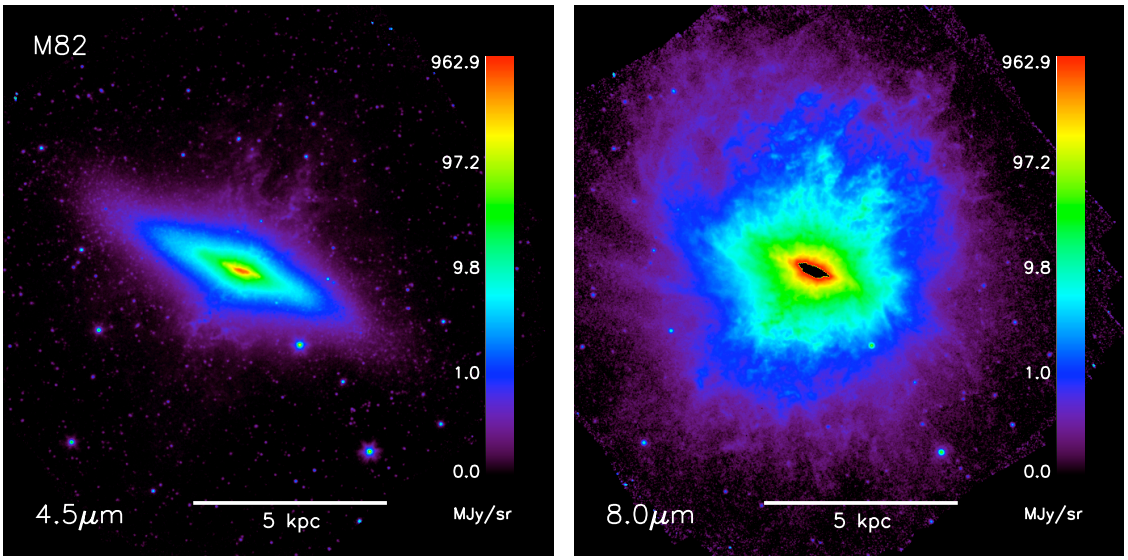

Figure 2.20: Comparing IRAC 4.5 and 8.0 μm maps of M82. The intensity scalings are "asinh" as described in Figure 2.11. North is up and east is left in both images.

The extraplanar PAH features we identify often coincide with previously observed Hα, X-ray, UV, and molecular features. Amongst these observations, Hα appears to trace the spatial extent and morphology of extraplanar PAH features best, though more observations of X-ray, UV, and molecular features are needed for comparison. Bright Hα filaments and areas of diffuse Hα emission very frequently have a PAH analog. However there doesn't seem to be an entirely consistent correlation between these two tracers, since some significant features do not match (e.g. NGC 1705 and NGC 6810). The z_{ext} of PAH emission is often less than coincident Hα or X-ray features, suggesting PAHs do not survive out to the same distances as the wind's gas components, or the sensitivity of the IRAC data is not sufficient to pick up the full extent of these features.

We also compare our measurement of extraplanar PAH flux (f_{ePAH}) to the

total IR flux (F_{IR}) of our sources. Since F_{IR} relates to the galaxy's SFR (excluding possible contributions from the AGN), comparing these fluxes should give some insight into what physical mechanism drives the PAHs out of the galaxy. We plot f_{ePAH} vs. F_{IR} in Figure 2.21. The line in Figure 2.21 represents a power law fit given by:

$$f_{ePAH} = 0.010\ (\pm^{0.003}_{0.002})\ \left(\frac{F_{IR}}{10^{-9}\ erg\ s^{-1}\ cm^{-2}}\right)^{1.13\ (\pm 0.11)}\ Jy \qquad (2.12)$$

This correlation is thus nearly consistent with linearity and has correlation coefficient $r = 0.89$. It provides further support for a link between extraplanar emission and star formation as well as a surface density threshold on the energy or momentum injection rate for ejection of material above the disk [e.g. Schiano, 1985, Mac Low & McCray, 1988, Mac Low et al., 1989, Koo & McKee, 1992a,b, Lehnert & Heckman, 1995, Rossa & Dettmar, 2003, Strickland et al., 2004a,b, Tüllmann et al., 2006]. Significantly, all the open-symbol points - indicating galaxies where we used a 20σ contour region to measure f_{ePAH} - fall below this power law fit in Figure 2.21. These points should probably be considered lower limits, since part of the extraplanar PAH emission associated with these lower inclination disks may overlap with the PAH emission from the disk or be occulted by the disk itself. The points for NGC 2992 and NGC 4388 also lie below the fit. They are the only objects in our sample clearly dominated by a central AGN rather than star formation. This result suggests AGN-driven winds in the absence of robust star formation do not eject PAHs as efficiently. In these cases, the presence of an AGN may also affect the

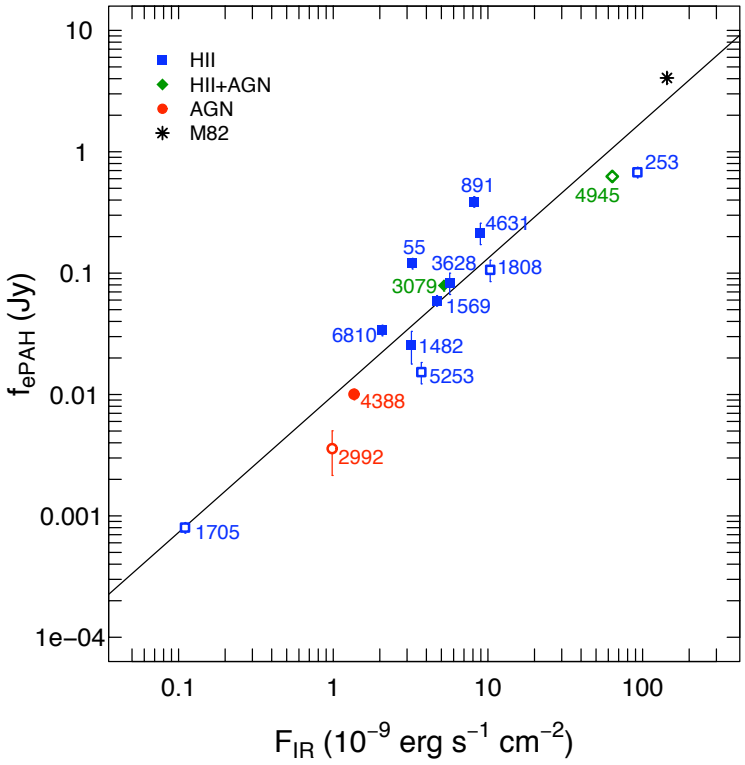

Figure 2.21: The extraplanar PAH flux, f_{ePAH}, plotted versus the calculated total IR flux, F_{IR}, on a log-log scale. Meaning of the symbols is the same as in Figure 2.1. The line is a power law fit with exponent 1.13 $\pm$ 0.11. (see § 2.5).

emitting grain distribution via grain destruction or ionization by the hardness of the radiation field [Smith et al., 2007, Diamond-Stanic & Rieke, 2010]. This tentative difference between AGN- and supernova-driven winds needs to be confirmed with a larger sample of AGN.

We compare the characteristic properties of extraplanar PAH emission to SFR surface density in Figure 2.22. The plot in the top-left panel of Figure 2.22 suggests a moderate correlation between I_{ePAH} and Σ_{SFR} with significant scatter and correlation coefficient $r = 0.55$. The open symbols on the plot tend to fall at lower I_{ePAH} values than other galaxies at similar values of Σ_{SFR}, suggesting again that

an inclined disk probably coincides with or occults a significant portion of the extraplanar PAH flux. The plot in the center-left panel of Figure 2.22 shows scattered H_{ePAH} values, but we do find that the galaxies with smaller diameters ($D_{4.5\mu m} < 5$ kpc; NGC 1569, NGC 1705, and NGC 5253) tend to fall near the lower end of the H_{ePAH} range, as would be expected. NGC 4388 also has a low H_{ePAH} value relative to the rest of the sample, and it's very likely that flux from tidal features increases the value for NGC 2992, so the AGN without robust star formation in our sample tend not to produce broadly extended extraplanar PAH emission features.

As listed in Table 2.3, our sample galaxies span a broad range of sizes and luminosities. Since large galaxies have more of everything compared to dwarf galaxies, they not only have larger SFRs, stellar masses, and disks on average than their dwarf counterparts, but their disks and associated extraplanar regions also extend higher vertically from the disk mid-plane than in dwarf galaxies, and so they tend to have larger H_{ePAH} values on average. To put all galaxies on the same footing, it is therefore natural to normalize H_{ePAH} by the size of the galaxy. Normalization of H_{ePAH} by D_{25} results in a significant correlation with Σ_{SFR}, which is shown in the bottom-left panel of Figure 2.22. The correlation coefficient between H_{ePAH}/D_{25} and Σ_{SFR} is $r = 0.93$, and the best fit power law has an exponent of 0.62 ± 0.12.

The point for NGC 891 (read vertically from the labels in the center-left panel) exhibits the largest offset from the overall trend. The anomalously large H_{ePAH} for NGC 891 is more challenging to explain, but may be due to the halo-like structure of the extraplanar PAH emission in contrast with most other galaxies in our sample, which display filamentary extraplanar PAH emission. In the case of halo-like PAH

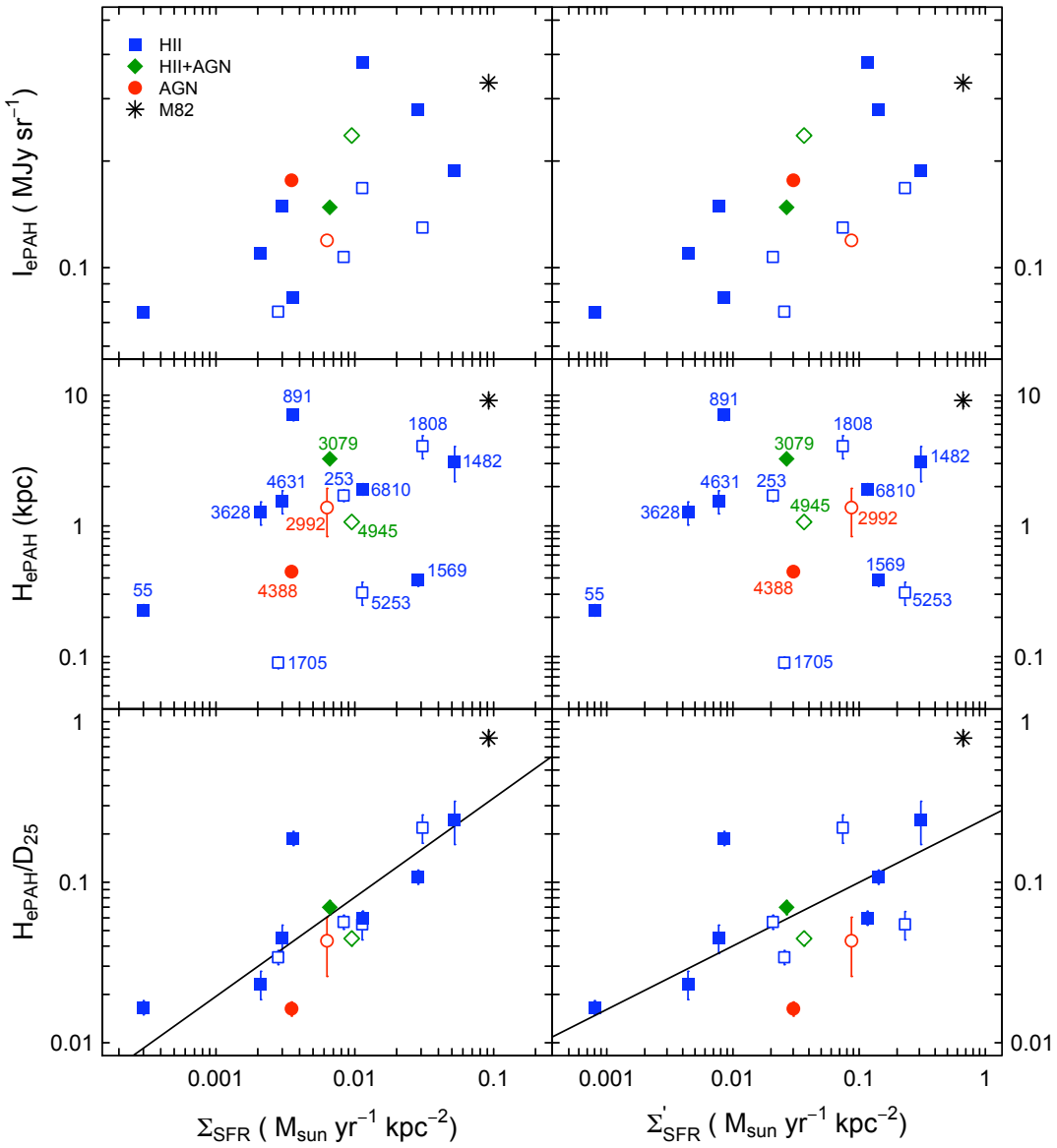

Figure 2.22: Characteristic extraplanar PAH surface brightness (I_{ePAH}), characteristic extraplanar emission height (H_{ePAH}), and H_{ePAH} scaled by the stellar disk diameter (H_{ePAH}/D_{25}) plotted versus the galaxy's star formation rate (SFR) surface density (Σ_{SFR}) and characteristic SFR surface density (Σ'_{SFR}, see § 2.5) on log-log scales. The best fit power laws shown in the bottom-left and bottom-right panels as solid lines have exponents of 0.62 ± 0.12 and 0.40 ± 0.12, respectively. Meaning of the symbols is the same as in Figure 2.1 (see § 2.4.2).

emission, equation 2.9 produces a larger H_{ePAH} value than in the case of filamentary emission, because the overall flux (f_{ePAH}) is larger and I_{ePAH} is smaller (see Figure 2.10).

Using D_{PAH} to calculate Σ'_{SFR} in the right column of Figure 2.22, we find similar results to the left column of plots. The correlation coefficient between H_{ePAH}/D_{25} and Σ'_{SFR} is $r = 0.89$, and the best fit power law shown in the bottom-right panel of Figure 2.22 has an exponent of 0.40 ± 0.12. We also found a similar correlation between $H_{ePAH}/D_{4.5\mu m}$ and Σ_{SFR}. As a note of caution to the reader, we point out that the normalization factor D_{25} on the vertical axis of Figure 2.22 may introduce an artificial correlation due to the linear correlations between D_{25}, $D_{4.5\mu m}$, and D_{PAH} (see Figure 2.9) and the fact that Σ_{SFR} and Σ'_{SFR} depend on D_{25}^{-2} and D_{PAH}^{-2} respectively. While we cannot completely rule out this possibility, we note that H_{ePAH} also depends on $D_{4.5\mu m}^{-1}$ according to equation 2.9, so we would expect a log-log slope of unity between H_{ePAH}/D_{25} and Σ_{SFR} or Σ'_{SFR}, which is inconsistent with our findings. Therefore, we believe that the correlations between H_{ePAH}/D_{25} and Σ_{SFR} and Σ'_{SFR} are physically motivated. These correlations support the idea of a surface density threshold on the energy or momentum injection rate necessary for elevating the disk ISM sufficiently high above the disk to be detectable as extraplanar material.

2.6 Summary

We have used existing data from the *Spitzer Space Telescope* archive to perform the first multi-object search for extraplanar PAH emission associated with known galactic winds. The data from the *Spitzer* archive are ideal for detecting PAHs due to the strength of the 7.7 μm emission feature, which falls conveniently in the IRAC 8.0 μm band. Our sample contains 16 nearby known wind galaxies, for which there are publicly available IRAC data. Our analysis of these data has yielded the following results:

- *Frequent Detection* - We found extraplanar PAH features extending from 15 of the 16 known wind galaxy in our sample with the exception of NGC 1705, which does not have a favorable orientation to search for extraplanar PAH emission.

- *Kiloparsec-Scale Extent* - The extraplanar PAH features we identified extend to projected distances $\sim$ 0.8 - 6.0 kpc. However, the extent of extraplanar PAH features is often less than that of coincident ionized gas features, suggesting PAHs do not survive out to the same distances, or the *Spitzer* data are not sensitive enough to detect PAH emission out that far.

- *Varied Morphology* - A variety of extraplanar PAH features were observed from filamentary structures and large areas of diffuse emission to the rare isolated cloud. The brightest filaments and bulk extraplanar PAH emission appear to originate close to galactic nuclei.

- *Correlations with Other Phases of the ISM* - Since extraplanar PAH features often trace the wind structures detected in Hα and X-rays, the PAHs likely represent cold ISM being swept out of the galaxy by the wind. However, not all features of the ionized gas phase (particularly Hα) match perfectly, so the presence of ionized gas in a wind does not necessarily imply the presence of extraplanar PAHs. This may be due to dust grain destruction or insufficient sensitivity of the Spitzer data.

- *Connection with Star Formation Activity in the Disk* - We found that extraplanar PAH emission flux correlates linearly with total IR flux, a direct tracer of the SFR (excluding possible contributions from an AGN). Employing a more quantitative analysis of the extent of extraplanar PAH emission, we derive a characteristic scale height of the extraplanar PAH emission, H_{ePAH}, for each galaxy. We find a significant correlation between the surface density of star formation in the disk and the characteristic scale height of the extraplanar PAH emission, once it is normalized to the galaxy diameter. This direct link between the star formation activity in the disk and the extent of the extraplanar PAH emission is similar to that seen when considering the extraplanar Hα emission. This result reinforces the idea of a surface density threshold on the energy or momentum injection rate needed to eject material sufficiently high above the disk to be detectable as extraplanar material.

Chapter 3

Exploring the Dust Content of Galactic Winds with *Herschel* II. Nearby Dwarf Galaxies

3.1 Introduction

Galactic winds are a fundamental mechanism of galaxy evolution (see Veilleux et al. 2005 for a review). Simulations have shown that the outflows of material in winds can inhibit the growth of a central supermassive black hole and curb the galactic star formation rate (SFR) by removing its fuel [e.g., Di Matteo et al., 2005, Narayanan et al., 2008, Hopkins & Elvis, 2010]. Winds have also been invoked to explain a host of galaxy observations, including the mass-metallicity relation [Tremonti et al., 2004], the relation between central black hole mass and bulge velocity dispersion [Ferrarese & Merritt, 2000, Gebhardt et al., 2000], and metal enrichment of the intracluster medium and intergalactic medium [e.g., Renzini, 1997,

Buote, 2000]. Furthermore, evidence for galactic winds at $z > 1$ [e.g., Pettini et al., 2001, Shapley et al., 2003, Smail et al., 2003, Weiner et al., 2009, Steidel et al., 2010, Erb et al., 2012, Martin et al., 2012] points to their importance in understanding the past history of the universe. Therefore, detailed observations of galactic winds are critical to fleshing out the narrative of galaxy evolution. Although negative feedback may assert even greater influence at high redshift, where strong starbursts and active galactic nuclei are more commonplace, nearby sources provide the best opportunities for detailed observations of the resultant winds. Investigating the winds of dwarf galaxies is particularly important due to the apparent metal depletion and lower star formation yield at the low end of the galactic mass distribution [Tremonti et al., 2004].

Prior to 2005, much of the observational data emphasized the entrained gas in winds from the neutral gas [e.g., Heckman et al., 2000, Rupke et al., 2002, 2005a,b,c, Schwartz & Martin, 2004, Martin, 2005] to ionized gas [e.g., Heckman et al., 1990, Lehnert & Heckman, 1995] to the highly ionized X-ray emitting plasma [e.g., Read et al., 1997, Martin, 1999, Pietsch et al., 2000, Martin et al., 2002, McDowell et al., 2003, Ehle et al., 2004, Huo et al., 2004, Strickland et al., 2004a,b]. Meanwhile, simulations of winds interacting with non-spherical, radiative, dense or giant molecular clouds [Cooper et al., 2008, 2009] have reproduced the formation of filamentary structure observed in many wind-hosting galaxies. Recent observations have shown that these outflows also entrain dust [e.g., Alton et al., 1999, Heckman et al., 2000, Radovich et al., 2001, Tacconi-Garman et al., 2005, Engelbracht et al., 2006, Kamphuis et al., 2007, Kaneda et al., 2009, 2010, Roussel et al., 2010, McCormick et al.,

2013, Meléndez et al., 2015] and molecular gas [e.g., ?Walter et al., 2002, Sakamoto et al., 2006, Veilleux et al., 2009b, Fischer et al., 2010, Feruglio et al., 2010, Irwin et al., 2011, Sturm et al., 2011, Alatalo et al., 2011, Aalto et al., 2012, Veilleux et al., 2013, Cicone et al., 2014]. Dust grains found in the interstellar medium (ISM) were formed in the atmospheres of evolved stars or during the outbursts of novae and supernovae, but can also be destroyed and reconstituted in the ISM. Interstellar dust plays a crucial role in galaxy evolution and star formation. It absorbs and scatters light, it can act as the catalyst to form molecules through reactions not possible in the gas phase, it can enrich or deplete the interstellar gas via destruction and evaporation of grains or condensation on grains, and electrons liberated from dust grains via the photoelectric effect can heat the ISM gas [Krügel, 2002, Lequeux, 2005]. Therefore, investigating the distribution, mass, and energy of the dust in wind galaxies provides critical information for understanding galaxy evolution. Observations of dusty winds may even catch galaxies in the act of expelling their star formation fuel, eventually halting stellar nurseries [e.g., Roussel et al., 2010, Sturm et al., 2011, Bolatto et al., 2013, Veilleux et al., 2013, Cicone et al., 2014].

In the first paper of this series [Meléndez et al., 2015, hereafter Paper I], we presented *Herschel Space Observatory* [Pilbratt et al., 2010] observations of the nearby wind galaxy NGC 4631. In this second paper of the series , we examine six nearby dwarf galaxies known to host galactic winds. For these sources, the resolution and sensitivity of previous far-infrared (FIR) data (e.g., *Spitzer* MIPS) are insufficient to test the properties of cool, shielded, wind-driven dust filaments or other features. The improved capabilities of *Herschel* have allowed us to interpret

the properties of cool circumgalactic dust in the winds of these nearby dwarf galaxies via new, very deep observations.

In § 3.2, we describe the selection criteria for our sample of nearby dwarf galaxies and provide tables summarizing their basic properties and the data we collected with *Herschel*. In § 3.3 and 3.4, we describe the data reduction process with example images and our analysis respectively. We present our results in § 3.5, including maps of each galaxy in *Herschel's* 70, 160, 250, 350, and 500 μm channels, and comparisons of circumgalactic dust properties with star formation and galactic stellar mass. Our results are summarized in § 3.6. Appendix B contains discussion of each individual galaxy and its features.

3.2 Sample

We chose our sample of six nearby dwarf galaxies primarily due to previous evidence of galactic winds at other wavelengths. Table 3.1 lists the galaxies, some of their properties, and selected references to evidence of galactic winds for each source. From previous multi-wavelength observations, each of the galaxies hosts active star formation (H II regions), and one (He 2-10) contains both H II regions and an AGN. Due to their star formation rate (SFR) densities and the inferred ages of recent or ongoing star formation episodes, the galaxies in our sample are often characterized as starbursts. The membership of NGC 3077 in the M81 group complicates the interpretation of circumgalactic material, so we often represent it with a different symbol on plots and treat it separately in the discussion of results. Due to the

presence of AGN activity in He 2-10 [Reines et al., 2011], we represent it with an open circle on plots to differentiate it from galaxies hosting just star formation.

Table 3.1: Nearby Dwarf Galaxies and Their Properties

Galaxy	Type	Morph.	D_{25}	d	scale	L_{IR}	12 +	M_{HI}	M_{H_2}	$\log(M_*/M_\odot)$	SFR	Σ_{SFR}	Wind/eDIG Ref.
			(')	(Mpc)	(pc/")	($10^9 L_\odot$)	log(O/H)	$10^8 M_\odot$	$10^8 M_\odot$		$M_\odot$ yr^{-1}	$M_\odot$ yr^{-1} kpc^{-2}	
(1)	(2)	(3)	(4)	(5)	(6)	(7)	(8)	(9)	(10)	(11)	(12)	(13)	(14)
He 2-10	H II + AGN	I0? pec	1.74	10.5	50.9	7.00	8.80	3.37	1.85	9.5†	0.81	0.23	1,2,3
NGC 1569	H II	IBm	3.63	3.36	16.3	1.24	8.16	2.11	0.0262	9.14	0.23	0.037	4,5,6,7,8,9
NGC 1705	H II	SA0$^-$ pec	1.91	5.10	24.7	0.0617*	8.48	0.953	1.06	8.37†	0.053	0.0084	10,11,12,13
NGC 1800	H II	IB(s)m	2.00	7.40	35.9	0.137*	8.58	1.58	0.670	8.84	0.034	0.022	8,14,15,16
NGC 3077	H II	I0 pec	5.37	3.83	18.6	0.608	8.78	8.95	0.0541	9.44	0.077	0.093	8,17,18,19,20
NGC 5253	H II	pec	5.01	3.77	18.3	1.48	8.28	1.50	0.0354	9.05†	0.23	0.44	13,21,22,23,24

[1] Galaxy Name.

[2] Optical/UV types are galaxies identified by star-forming H II regions (H II) and galaxies containing both an active galactic nucleus (AGN) and star-forming H II regions (H II + AGN).

[3] de Vaucouleurs morphological type from de Vaucouleurs et al. [1991] (hereafter RC3).

[4] Diameter (major axis) in arcminutes based on 25th magnitude B-band observations (RC3).

[5] z-independent distance. References: He 2-10: Tully 1988; NGC 1569: Grocholski et al. 2008; NGC 1705: Tosi et al. 2001; NGC 1800: Tully 1988; NGC 3077: Dalcanton et al. 2009; NGC 5253: Sakai et al. 2004.

[6] Spatial scale assuming the z-independent distance listed here.

[7] IR luminosity (8 - 1000 μm) expressed in units of $10^9 L_\odot$, calculated using equations in Table 1 of Sanders & Mirabel [1996], IRAS flux densities listed in the NASA/IPAC Extragalactic Database [Moshir et al., 1990, Sanders et al., 2003], and the distances listed in this table. The * indicates the calculation of these L_{IR} values included some upper limit IRAS fluxes.

[8] Metallicity derived using the method in Pettini & Pagel [2004] (O3N2), which has then been converted via the prescriptions in Kewley & Ellison [2008] to conform with the metallicities in Tremonti et al. [2004]. Uncertainties in the metallicity come from a combination of the method used (∼0.1 dex) and the conversion (∼0.06 dex). Emission line strength references: He 2-10, NGC 1569, NGC 5253: Kobulnicky et al. 1999; NGC 1705: Moustakas et al. 2010; NGC 1800: Moustakas & Kennicutt 2006; NGC 3077: McQuade et al. 1995.

[9] Stellar masses calculated using the M/L derived from Bell et al. [2003], Two Micron All Sky Survey K magnitudes [Skrutskie et al., 2003], and optical colors (either B-V or B-R). The † indicates masses adopted from Zastrow et al. [2013] calculated using this method. We used the optical colors found in RC3 to calculate the masses of NGC 1569, NGC 1800, and NGC 3077.

[10] Molecular (H_2) gas masses calculated from CO data from Young et al. [1995] (He 2-10, NGC 1569, NGC 3077, NGC 5253) using the method in Bolatto et al. [2013] (eqs. 3 & 7) or by multiplying the star formation rate by an assumed depletion time of 2 Gyr (NGC 1705 & NGC 1800).

[11] Stellar masses calculated using the M/L derived from Bell et al. [2003], Two Micron All Sky Survey K magnitudes [Skrutskie et al., 2003], and optical colors (either B-V or B-R). The † indicates masses adopted from Zastrow et al. [2013] calculated using this method. We used the optical colors found in RC3 to calculate the masses of NGC 1569, NGC 1800, and NGC 3077.

[12] Star formation rate from combining $L_{H\alpha}$ [Kennicutt et al., 2008] and L_{IR} (this work, see above) according to the prescription in Kennicutt et al. [2009] (eq. 16).

[13] Star formation rate surface density using the star formation rate listed here and the ionized gas radius ($R_{H\alpha}$) listed in Calzetti et al. [2010].

[14] Selected references to a galactic wind or extraplanar diffuse ionized gas (eDIG): (1) Méndez et al. 1999; (2) Johnson et al. 2000; (3) Kobulnicky & Martin 2010; (4) Waller 1991; (5) Hunter et al. 1993; (6) Heckman et al. 1995; (7) della Ceca et al. 1996; (8) Martin 1997; (9) Westmoquette et al. 2008; (10) Meurer et al. 1989; (11) Meurer et al. 1992; (12) Meurer et al. 1998; (13) Heckman et al. 2001; (14) Marlowe et al. 1995; (15) Hunter 1996; (16) Rasmussen et al. 2004; (17) Thronson et al. 1991; (18) Martin 1998; (19) Ott et al. 2003; (20) Calzetti et al. 2004; (21) Calzetti et al. 1999; (22) Strickland & Stevens 1999; (23) Kobulnicky & Skillman 2008; (24) Zastrow et al. 2011.

We acquired very deep (> 6 hrs.) *Herschel Space Observatory* PACS [Poglitsch et al., 2010] images in the 70 and 160 μm infrared (IR) channels for each of the six dwarfs in our sample as part of a two stage observational program to investigate nearby star-forming galaxies. Each of the 70 and 160 um PACS observations consisted of a 4-times repeated scan map of either 30 or 40 scan legs 3' in length and separated by 4" to fully map the galaxies and and to obtain a very high and homogeneous coverage well beyond the size of the galaxies. These 2-band scan-map observations were conducted seven times, each time with a different angle with respect to the detector array orientation. This technique virtually eliminates systematic noise from low-level striping and reaches approximately Poisson noise limits. We also acquired SPIRE [Griffin et al., 2010] data at 250, 350, and 500 μm for the one galaxy in our sample which had not already been observed (NGC 1800) and downloaded archived SPIRE data for the other five galaxies. The SPIRE observations were performed in the LargeScanMap mode using orthogonal scan directions and multiple iterations for four out of the six galaxies (single iterations: He 2-10 and NGC 1569). The *Herschel* data are summarized in Table 3.2.

In additional to the new *Herschel* data we acquired, we also brought together ancillary data for each galaxy in four additional bands: Hα, 4.5, 8.0, and 24 μm. A few different observers collected the Hα data, and we downloaded the IR data from the *Spitzer* archive for IRAC (4.5 and 8.0 μm) and MIPS (24 μm). The ancillary data are summarized in Table 3.3.

Table 3.2: *Herschel Space Observatory* Data

Galaxy	Instrument (PACS[c]/SPIRE)	t_{int}^{a} (hrs)	OD / OID(s)[b]	Principal Investigator (OT/KPGT/SDP/KPOT)[e]
He 2-10	PACS	6.56	1076 / 1342244883-89	Veilleux, S. (OT2)
	SPIRE	0.07	0374 / 1342196888	Madden, S. (KPGT)
NGC 1569	PACS	6.56	1058 / 1342243816-22	Veilleux, S. (OT2)
	SPIRE	0.15	0318 / 1342193013	Madden, S. (KPGT)
NGC 1705	PACS	6.56	0968 / 1342236656-62	Veilleux, S. (OT1)
	SPIRE	0.20	0158 / 1342186114	Madden, S. (SDP)
NGC 1800	PACS	6.56	1377 / 1342263895-901[d]	Veilleux, S. (OT2)
	SPIRE	0.16	1024 / 1342240035	Veilleux, S. (OT2)
NGC 3077	PACS	8.74	1059 / 1342243845-51	Veilleux, S. (OT2)
	SPIRE	0.58	0318 / 1342193015	Kennicutt, R. C., Jr. (KPOT)
NGC 5253	PACS	8.74	1194 / 1342249927-33	Veilleux, S. (OT2)
	SPIRE	0.29	0459 / 1342203078	Madden, S. (KPGT)

[a] Total observation integration time in hours.
[b] *Herschel* Operation Day / Observation ID number(s).
[c] The PACS photometer scan maps were either 3' scan legs × 30 legs × 4" leg separation (He 2-10, NGC 1569, NGC 1705, NGC 1800) or 3' scan legs × 40 legs × 4" leg separation (NGC 3077 and NGC 5253).
[d] The PACS photometer observations from OD1377 (NGC 1800) suffered from a detector problem: After OD 1375 half of the red PACS photometer array was lost. Point-source photometry was still possible, but you should clearly see a much lower coverage in these maps.
[e] *Herschel* Open Time (OT), Key Programme Guaranteed Time (KPGT), Science Demonstration Phase (SDP), or Key Programme Open Time (KPOT).

Table 3.3: Ancillary Data

Galaxy	Band	t_{int} [1] (s)	Observatory/Instrument	Obs. ID(s) [2]	PI(s) [3]
He 2-10	Hα	1200	Magellan/MMTF	...	Oey, S.
	4.5 μm	41.6	*Spitzer*/IRAC	4329472	Rieke, G.
	8.0 μm	41.6	*Spitzer*/IRAC	4329472	Rieke, G.
	24 μm	2.62	*Spitzer*/MIPS	4347904	Rieke, G.
NGC 1569	Hα	300	KPNO/Bok	...	Martin, C. L.
	4.5 μm	52	*Spitzer*/IRAC	4434944	Fazio, G.
	8.0 μm	52	*Spitzer*/IRAC	4434944	Fazio, G.
	24 μm	2.62	*Spitzer*/MIPS	4435456	Fazio, G.
NGC 1705	Hα	1200	Magellan/MMTF	...	Oey, S.
	4.5 μm	214.4	*Spitzer*/IRAC	5535744, 5536000	Kennicutt, R. C., Jr.
	8.0 μm	214.4	*Spitzer*/IRAC	5535744, 5536000	Kennicutt, R. C., Jr.
	24 μm	3.67	*Spitzer*/MIPS	5549312	Kennicutt, R. C., Jr.
NGC 1800	Hα	901.2	KPNO/Bok	...	Martin, C. L.
	4.5 μm	428.8	*Spitzer*/IRAC	22530304, 22530560, 22530816, 22531072	Kennicutt, R. C., Jr.
	8.0 μm	428.8	*Spitzer*/IRAC	22530304, 22530560, 22530816, 22531072	Kennicutt, R. C., Jr.
	24 μm	3.67	*Spitzer*/MIPS	22624000	Kennicutt, R. C., Jr.
NGC 3077	Hα	1000	KPNO/Bok	...	Kennicutt, R. C., Jr.
	4.5 μm	4758.4 (804)*	*Spitzer*/IRAC	4331520, 22000640, 22354944, 22357760, 22358016, 22539520, 22539776	Kennicutt, R. C., Jr., Neff, S., Rieke, G.
	8.0 μm	4758.4 (804)*	*Spitzer*/IRAC	4331520, 22000640, 22354944, 22357760, 22358016, 22539520, 22539776	Kennicutt, R. C., Jr., Neff, S., Rieke, G.
	24 μm	3.67	*Spitzer*/MIPS	17597696	Rieke, G.
NGC 5253	Hα	1200	Magellan/MMTF	...	Oey, S., Veilleux, S., Zastrow, J.
	4.5 μm	249.6	*Spitzer*/IRAC	4386048	Houck, J. R.
	8.0 μm	249.6	*Spitzer*/IRAC	4386048	Houck, J. R.
	24 μm	3.67	*Spitzer*/MIPS	22679040	Kennicutt, R. C., Jr.

[1] Total integration time in seconds.
[2] Observation ID number(s).
[3] Principal Investigator(s).
* Total IRAC mosaic integration time for NGC 3077 (typical mosaic pixel integration time).

3.3 Data Reduction

After the *Herschel* observations were performed between January 2012 and March 2013, we obtained the new PACS and SPIRE data from the *Herschel* Science Archive (HSA). We downloaded the archival *Spitzer* Infrared Array Camera (IRAC) and Multiband Imaging Photometer (MIPS) data from the NASA/IPAC Infrared Science Archive. Before performing any reduction, we briefly examined the new *Herschel* data with version 10.3.0 of the Herschel Interactive Processing Environment (HIPE; Ott 2010), and we also inspected the Hα data and pipeline-processed *Spitzer* data (PBCDs) using SAOImage DS9.

3.3.1 *Herschel* Data Reduction

We reprocessed our *Herschel* data with HIPE up to Level-1 employing the PACS photometer pipeline [Weiner et al., 2009] and then passed these data on to the *Scanamorphos* v21 software[Roussel, 2013]. Since our deep *Herschel* observations aimed to detect very faint emission from cold dust in circumgalactic wind regions, we employed *Scanamorphos*, which was built specifically to handle scan mode observations like ours, the preferred acquisition mode for nearby galaxies. *Scanamorphos* exploits the redundancy of the observations in order to subtract low frequency noise due to thermal and non-thermal components. It also masks high frequency artifacts like cosmic ray hits before projecting the data onto a map. The final pixel sizes, which are $\sim 1/4$ the size of the point-spread functions (PSFs) for each detector, are

1.4, 2.85, 4.5, 6.25, and 9.0" for the 70, 160, 250, 350, and 500 μm maps respectively. The *Herschel* maps are shown in Figures 3.1 - 3.6 along with the ancillary Hα, 4.5, 8.0, and 24 μm data.

3.3.2 *Spitzer* Data Reduction

Our reduction of the *Spitzer* IRAC data followed the same procedures as those described in McCormick et al. [2013], summarized here. Starting from the basic calibrated data, we corrected any electronic and optical banding in the 8.0 μm channel. Several of our sample galaxies' bright nuclei generate broad point spread functions (PSFs) in both the 4.5 and 8.0 μm channels, which overlap with circumgalactic regions, so we subtracted the wings of any broad PSFs using the APEX and APEX QA modules of the *Spitzer Science Center*-provided MOPEX software [Makovoz & Khan, 2005]. Where necessary, we also performed a background subtraction to better distinguish background flux from circumgalactic features. Once the basic calibrated data were processed, we created maps of both channels using MOPEX. For NGC 1569, NGC 1705, and NGC 5253, we used the previously-reduced data presented in McCormick et al. [2013].

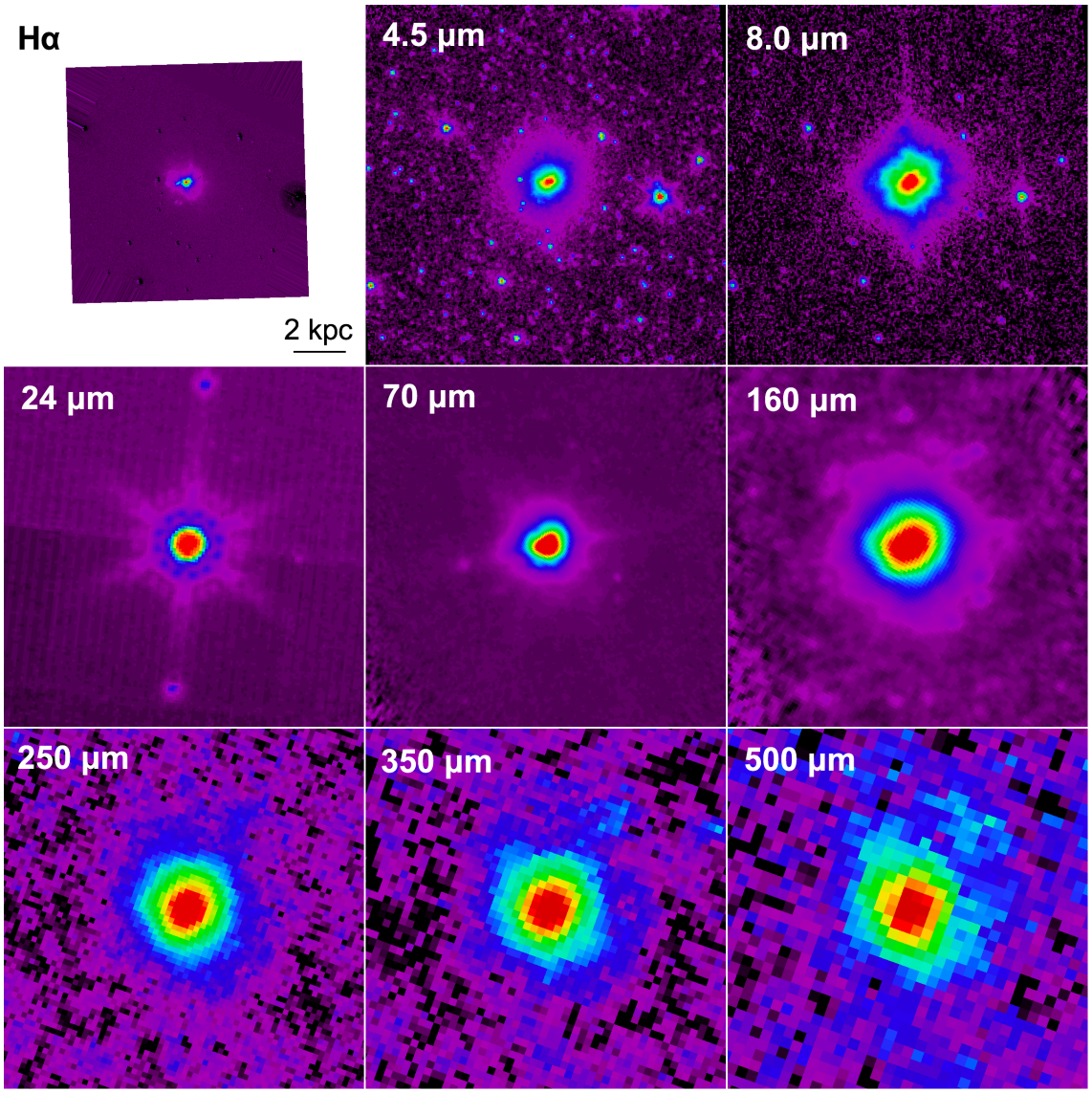

Figure 3.1: Henize 2-10 - Hα [Zastrow et al., 2013], IRAC 4.5 and 8.0 μm and MIPS 24 μm (*Spitzer* archive, this work), PACS 70 and 160 μm, and SPIRE 250, 350, and 500 μm (this work). All images are displayed with a logarithmic scale. North is up and east is to the left in all images. The bar in the Hα image indicates the scale in all images.

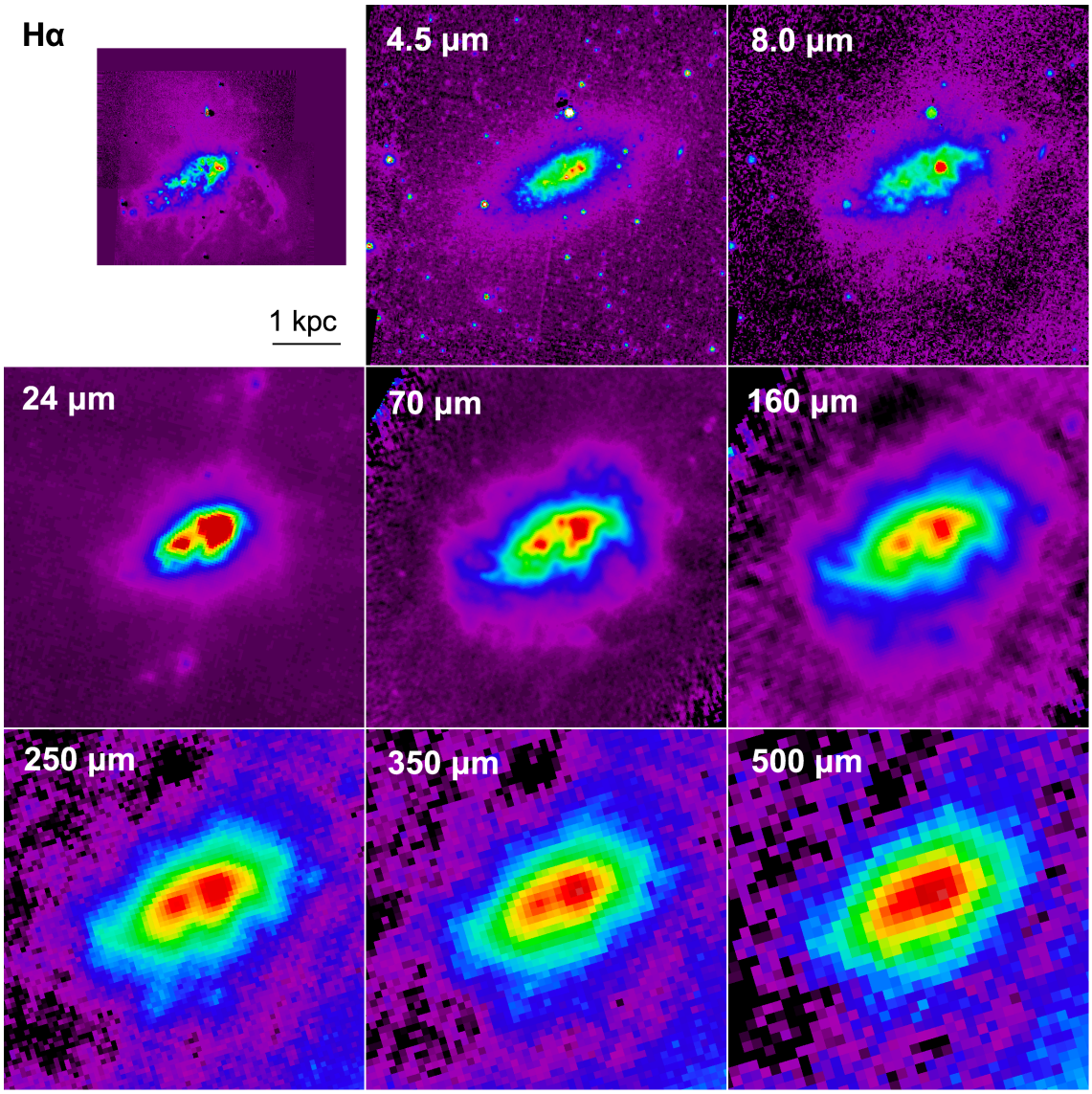

Figure 3.2: NGC 1569 - Hα [Martin, 1997], IRAC 4.5 and 8.0 μm [McCormick et al., 2013], otherwise, the same as in Figure 3.1.

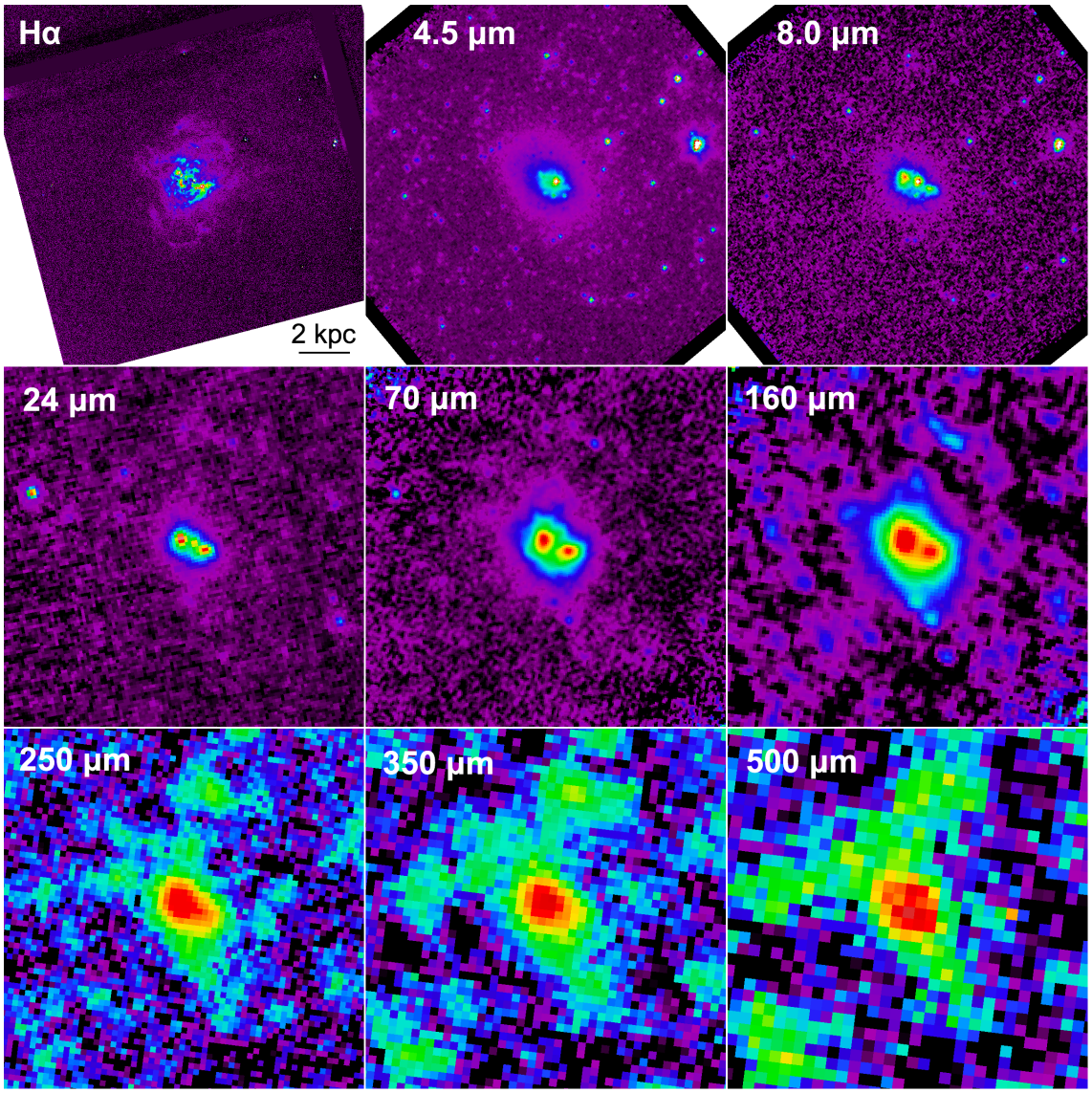

Figure 3.3: NGC 1705 - Hα [Zastrow et al., 2013], IRAC 4.5 and 8.0 μm [McCormick et al., 2013], otherwise, the same as in Figure 3.1.

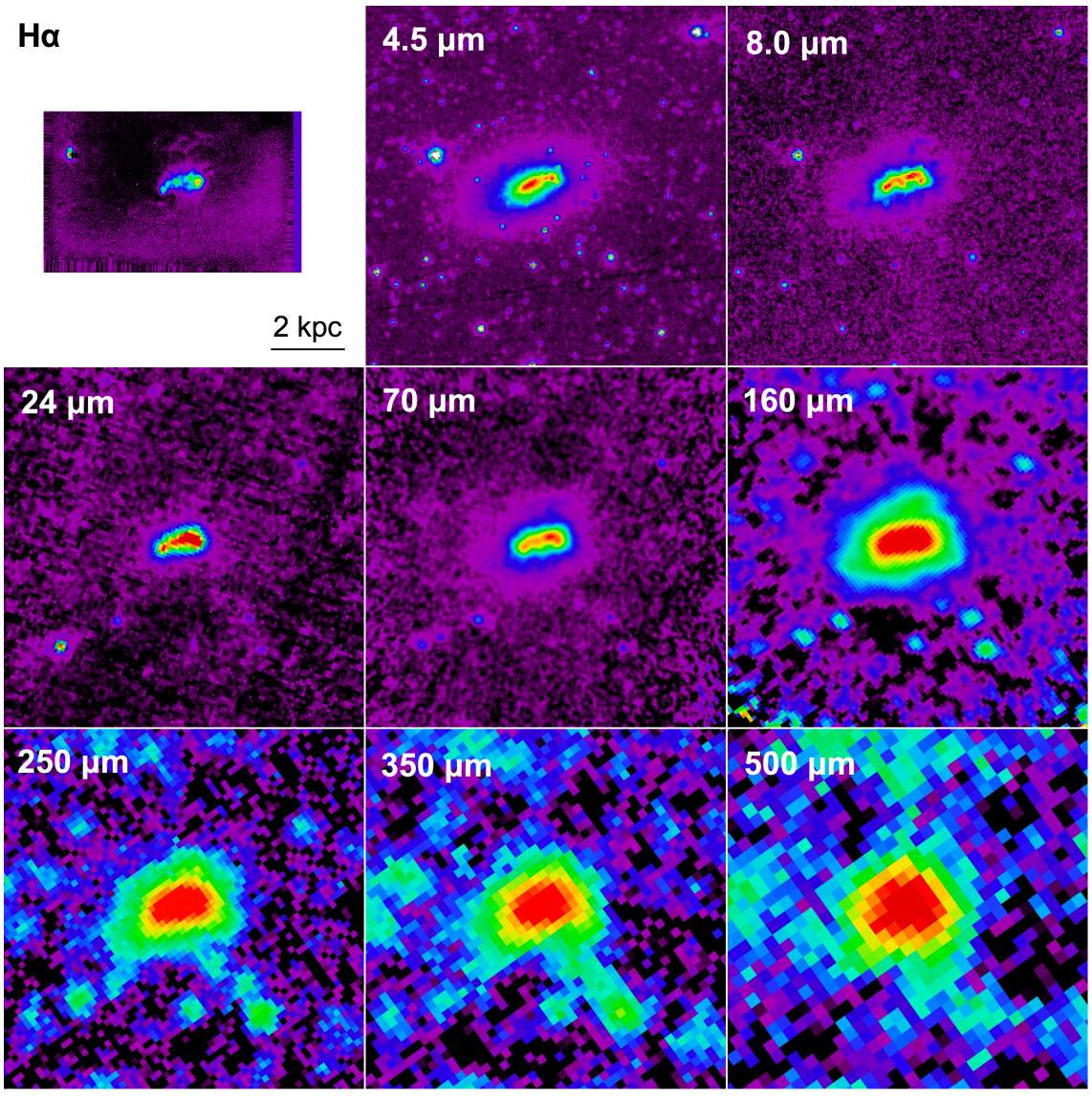

Figure 3.4: NGC 1800 - Hα [Martin, 1997], otherwise, the same as in Figure 3.1.

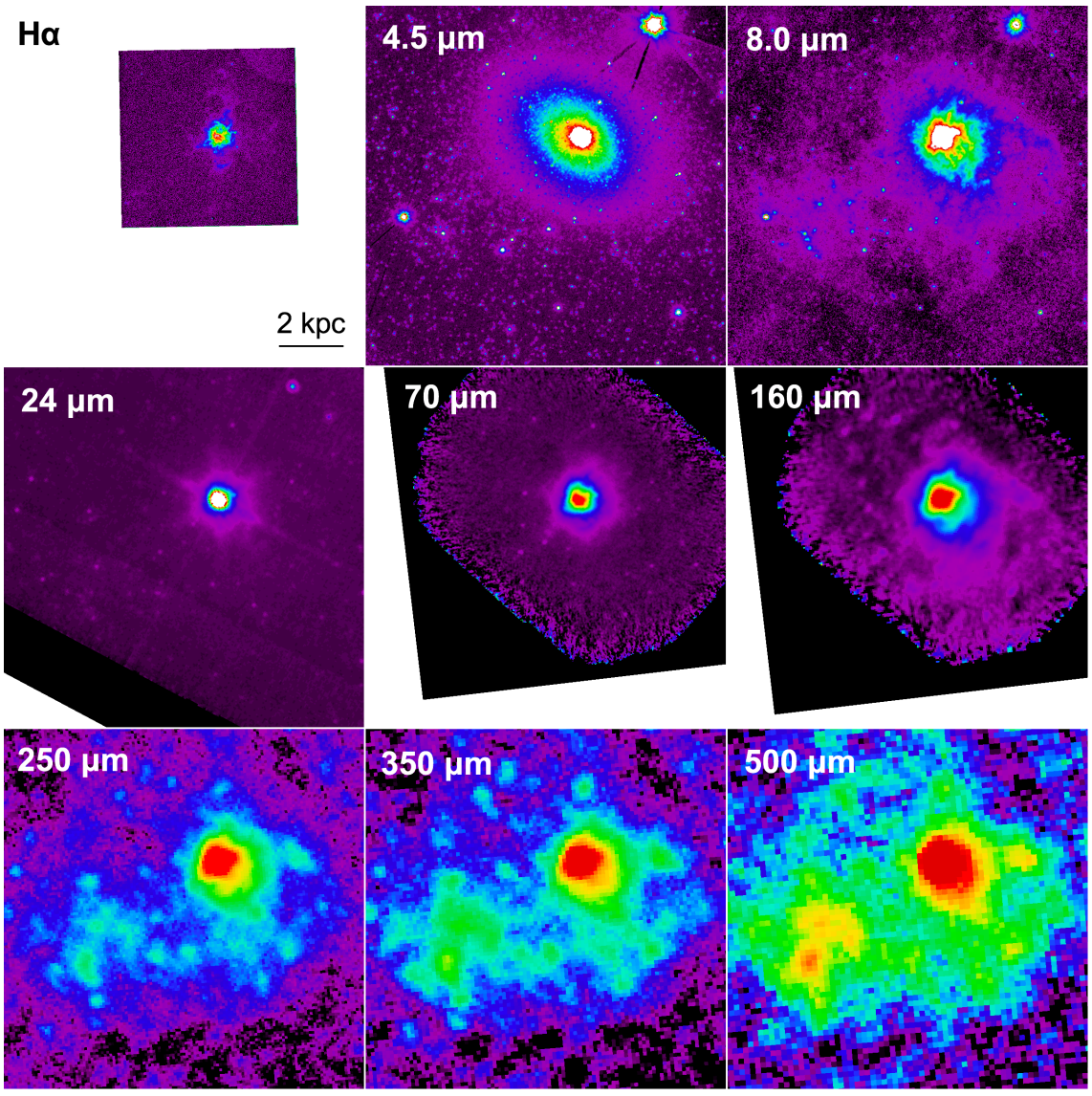

Figure 3.5: NGC 3077 - Hα [Dale et al., 2009], otherwise, the same as in Figure 3.1.

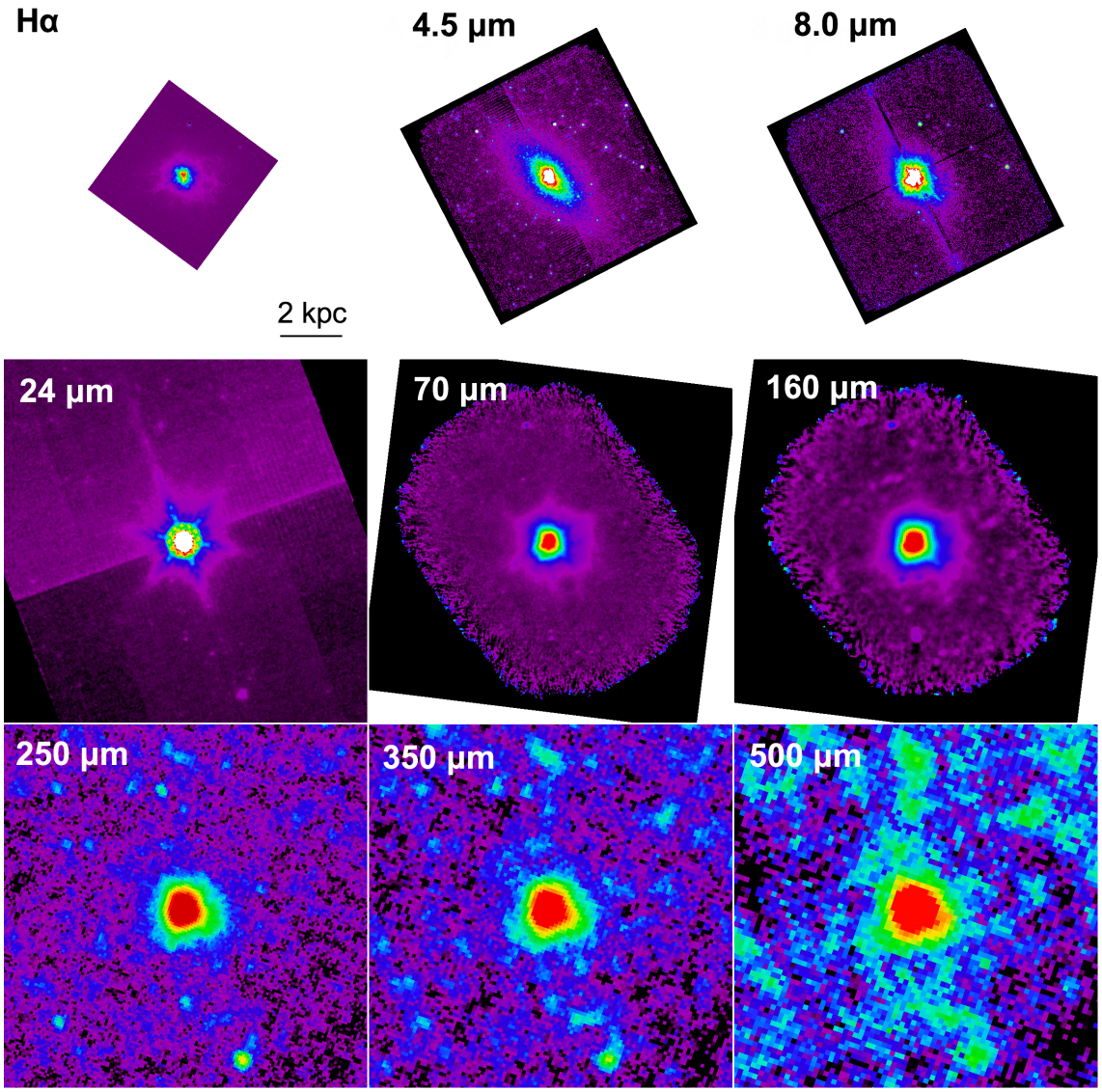

Figure 3.6: NGC 5253 - Hα [Zastrow et al., 2011], IRAC 4.5 and 8.0 μm [McCormick et al., 2013], otherwise, the same as in Figure 3.1.

3.4 Data Analysis

3.4.1 Disk-Circumgalactic Decomposition

Differentiating between a galaxy and its circumgalactic or extraplanar or halo region necessitates defining an edge or border between the two when analyzing an image projected on the sky. In McCormick et al. [2013], we defined an edge by applying two different methods to the predominantly stellar emission of the IRAC 4.5 μm channel, which generated very similar regions when both methods were workable. The first method employed a fitted scale height in the case of sufficiently edge-on disk galaxies. The second method used the standard deviation of the 4.5 μm background noise and a 20σ contour to delineate the galaxy from the circumgalactic regions. For the sample of dwarf galaxies in this work, which mostly exhibit irregular morphology, we used the same methods but defined a more conservative edge. We applied the scale height method using a multiple of five scale heights (instead of the three used in McCormick et al. [2013]) for NGC 1569 and a 5σ contour for the remaining galaxies. Figure 3.7 shows a comparison of the scale height regions determined for NGC 1569 and its 5σ contour. The more conservative scale height region comes close to matching the 5σ contour. For the sake of consistency, we will call all of these 'disk' regions, although most of the galaxies do not exhibit a classical disk morphology. The flux regions are shown in Figures 3.9 - 3.14. The circumgalactic flux region for NGC 1569 is necessarily conservative, because of the proximity of Galactic cirrus, which are noticeably impinging on the circumgalactic

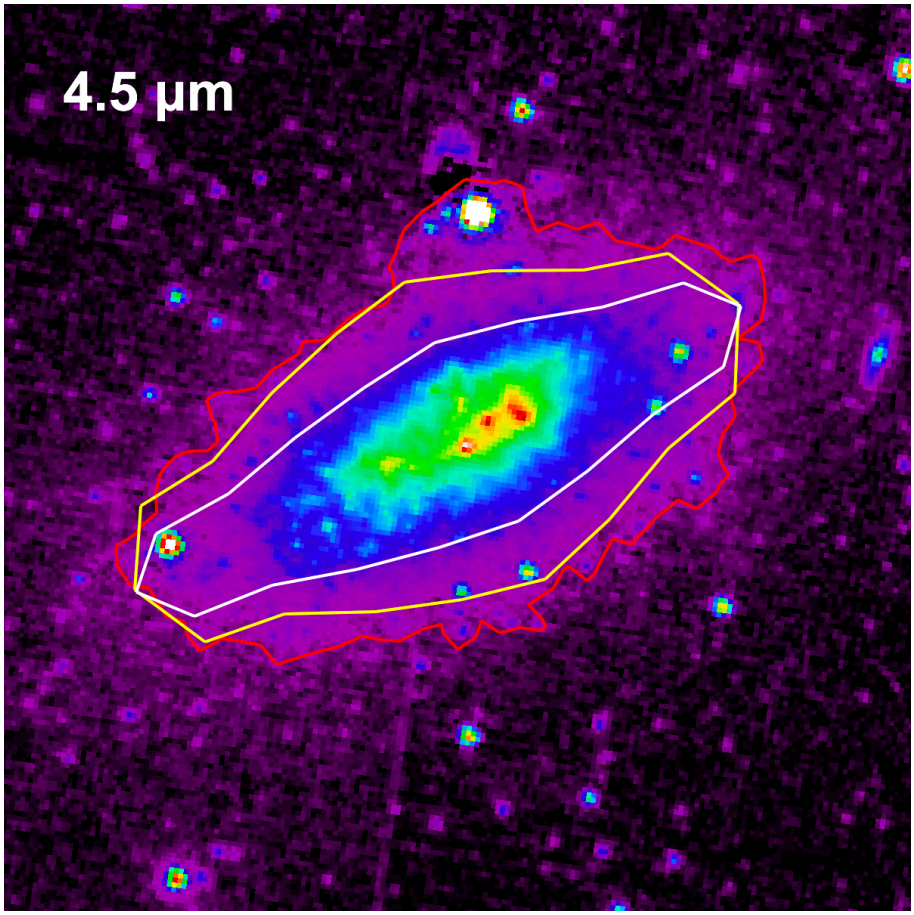

Figure 3.7: An example comparison of disk region edge definitions for the predominantly stellar component of NGC 1569 (*Spitzer* IRAC 4.5 μm). The white region shows the disk region defined by the fitted scale height method in McCormick et al. [2013]. The yellow region shows the more conservative fitted scale height disk region derived from a multiple of five scale heights and used in this work. The red contour shows the 5σ contour above the background noise for comparison.

region in the SPIRE maps (see Figure 3.2).

3.4.2 Removal of the Disk PSFs with a CLEAN Algorithm

In both the PACS and SPIRE instruments, the PSFs are broad enough that the wings from bright disk region sources bleed out and contribute significant excess flux to the circumgalactic regions where we are looking for just the faint circumgalactic dust emission. To account for this excess, we employed a modified version of

the CLEAN algorithm[1] [Högbom, 1974]. Our CLEAN algorithm finds the peak pixel within an area similar to the disk region, subtracts the appropriate PSF scaled by a pre-defined gain as a fraction of the peak pixel value, and repeats these two steps until the peak pixel value meets or drops below a pre-defined minimum threshold value. Once the minimum threshold value is reached, the algorithm outputs component and residual images. Since the galaxies in our sample contain broad, bright areas within their disk regions, we chose observations of Vesta (Obs. IDs 1342195624, 1342195625, also the reference PSF for PACS) and Uranus (Obs. ID 1342197342) as our beam PSFs. We selected *Herschel* observations of Vesta and Uranus with the same scan speed as our observations, which is important for matching the shape of the PSFs. We processed the Vesta and Uranus PSFs through the same combination of HIPE and *Scanamorphos* as described in § 3.3.1. Next, we rotated the PSFs to match the galaxy observations, centered the PSFs on their central pixels, and scaled the PSFs by normalizing their central peak pixels to a value of 1 for gain multiplication. Finally, we applied our CLEAN algorithm to each of the PACS and SPIRE images iteratively lowering the threshold value to determine circumgalactic flux value convergence. Figure 3.8 illustrates the before and after results of applying our CLEAN algorithm to the maps of NGC 1569. Across all bands before application of the CLEAN algorithm, we find $\sim$ 75-80% (standard deviation = $\sim$ 20%) of the flux in the circumgalactic region has bled out from the disk region. There is no apparent trend with wavelength. Residual maps after application of our CLEAN algorithm are shown in Figures 3.9 - 3.14.

[1]Adapted from http://www.mrao.cam.ac.uk/∼bn204/alma/python-clean.html.

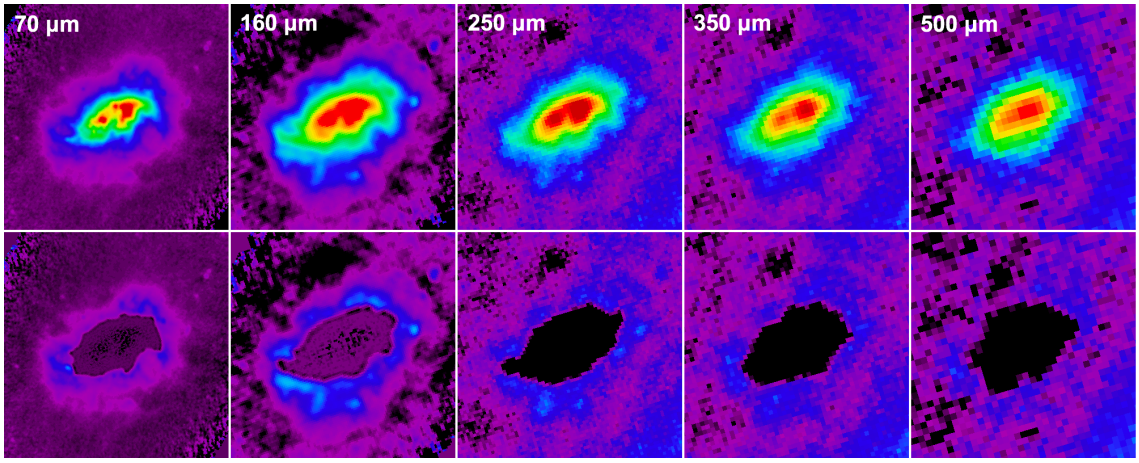

Figure 3.8: PACS and SPIRE maps of NGC 1569 (top row) plus the resulting residual maps (bottom row) after application of our modified CLEAN algorithm. We defined the regions where we applied the CLEAN algorithm in each band based on the disk region for NGC 1569. Since each map has a different pixel scale and slightly different morphology to the bright disk areas, the regions where we applied the CLEAN algorithm are similar in extent but necessarily slightly different from band to band. All maps are shown with logarithmic scale. North is up and east is to the left in all maps.

3.4.3 *Herschel* Flux Measurements

In each of the five *Herschel* bands, we took global flux measurements from the original *Scanamorphos* maps using a circular or elliptical aperture centered on the galaxy and containing the most extended circumgalactic cold dust feature. Note that the most extended features did not always appear in the same *Herschel* band. In each of the five bands, we calculated the cleaned circumgalactic flux by subtracting the disk region flux from the global region flux in the CLEAN residual maps. We then calculated the corrected disk flux by subtracting the cleaned circumgalactic flux from the original global flux value. Using this method, the excess flux that bled

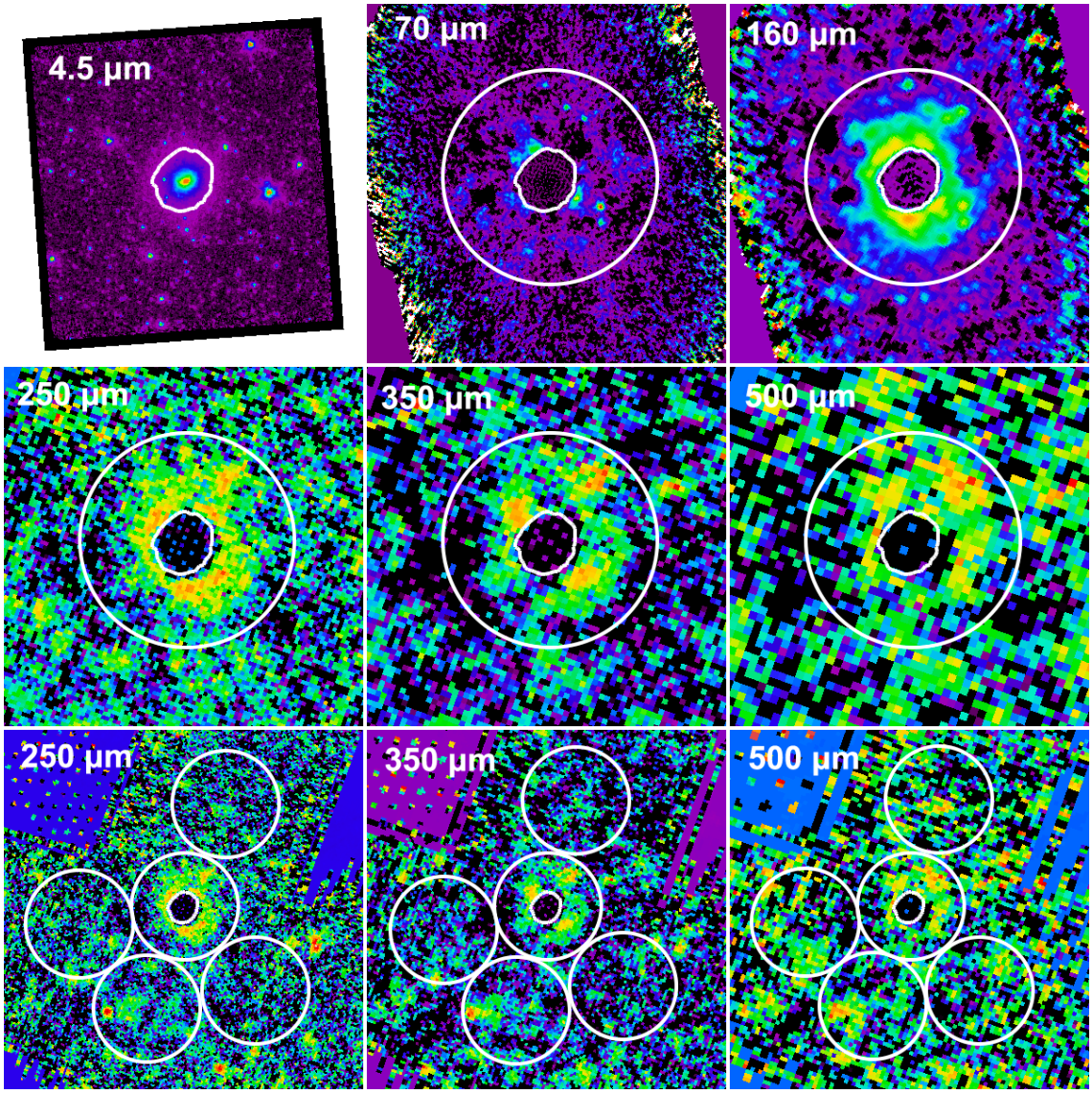

Figure 3.9: Henize 2-10 - 70, 160, 250, 350, and 500 μm *Herschel* maps after application of our CLEAN algorithm with the IRAC 4.5 μm map for comparison to the stellar component. All images are displayed with a logarithmic scale. North is up and east is to the left in all images. The white regions in the *Herschel* maps indicate the global flux region and the stellar disk region derived from the 4.5 μm data. The bottom row of SPIRE maps (250, 350, and 500 μm) show the regions used for background estimation at 0.5 the scale of the six panels shown above it.

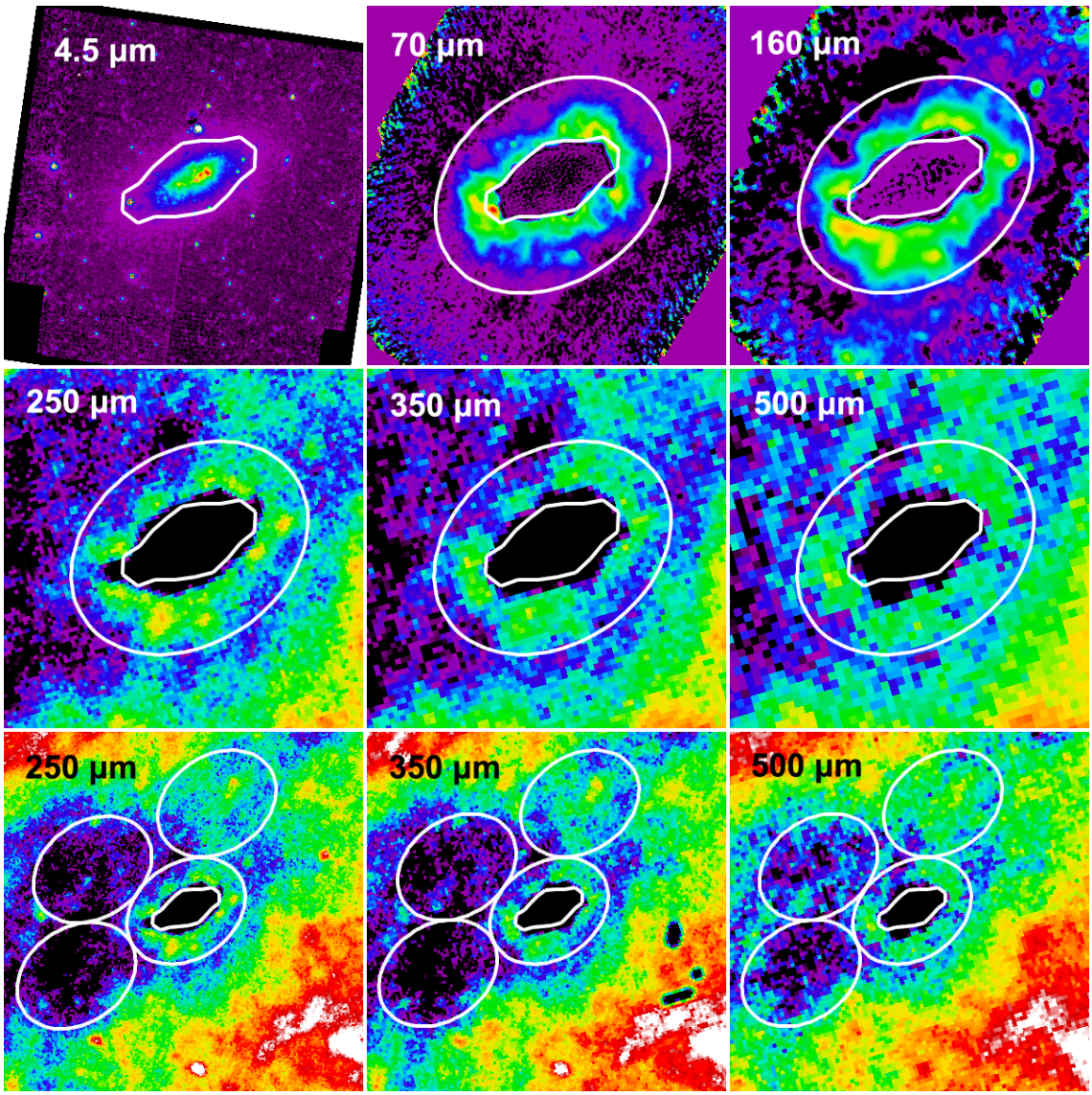

Figure 3.10: NGC 1569 - display is the same as in Figure 3.9.

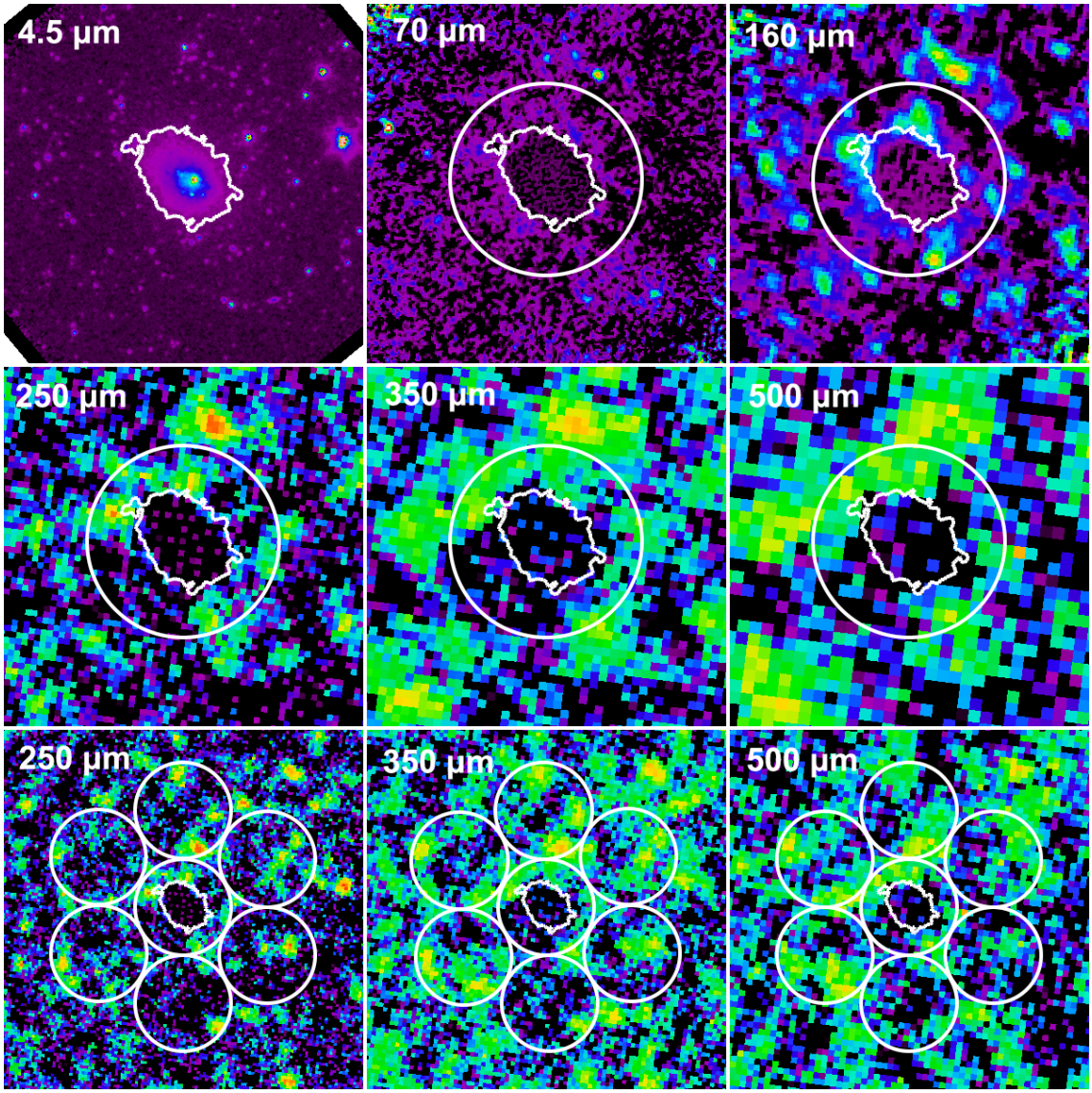

Figure 3.11: NGC 1705 - display is the same as in Figure 3.9.

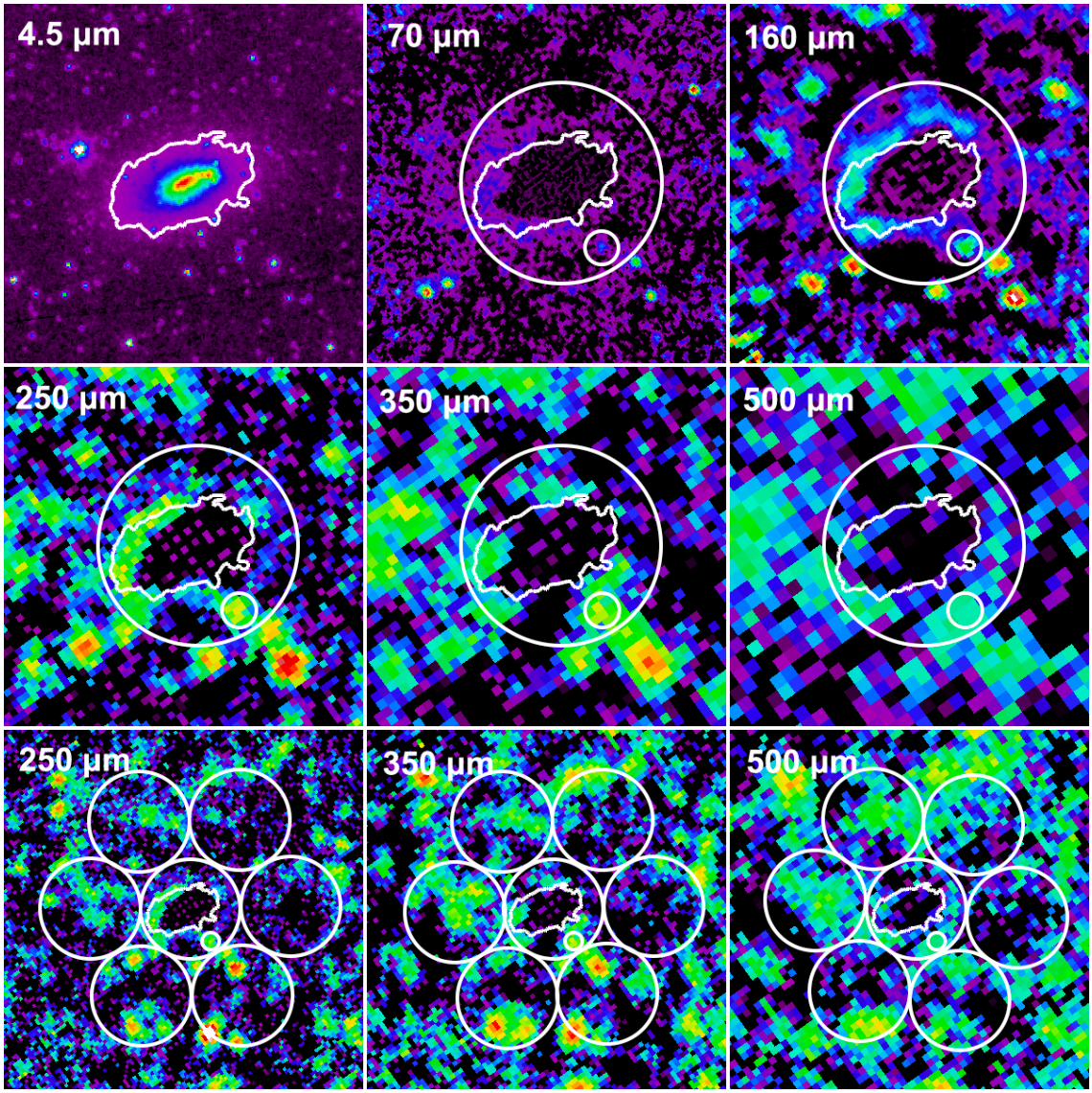

Figure 3.12: NGC 1800 - display is the same as in Figure 3.9, plus one region is masked (smaller white circle).

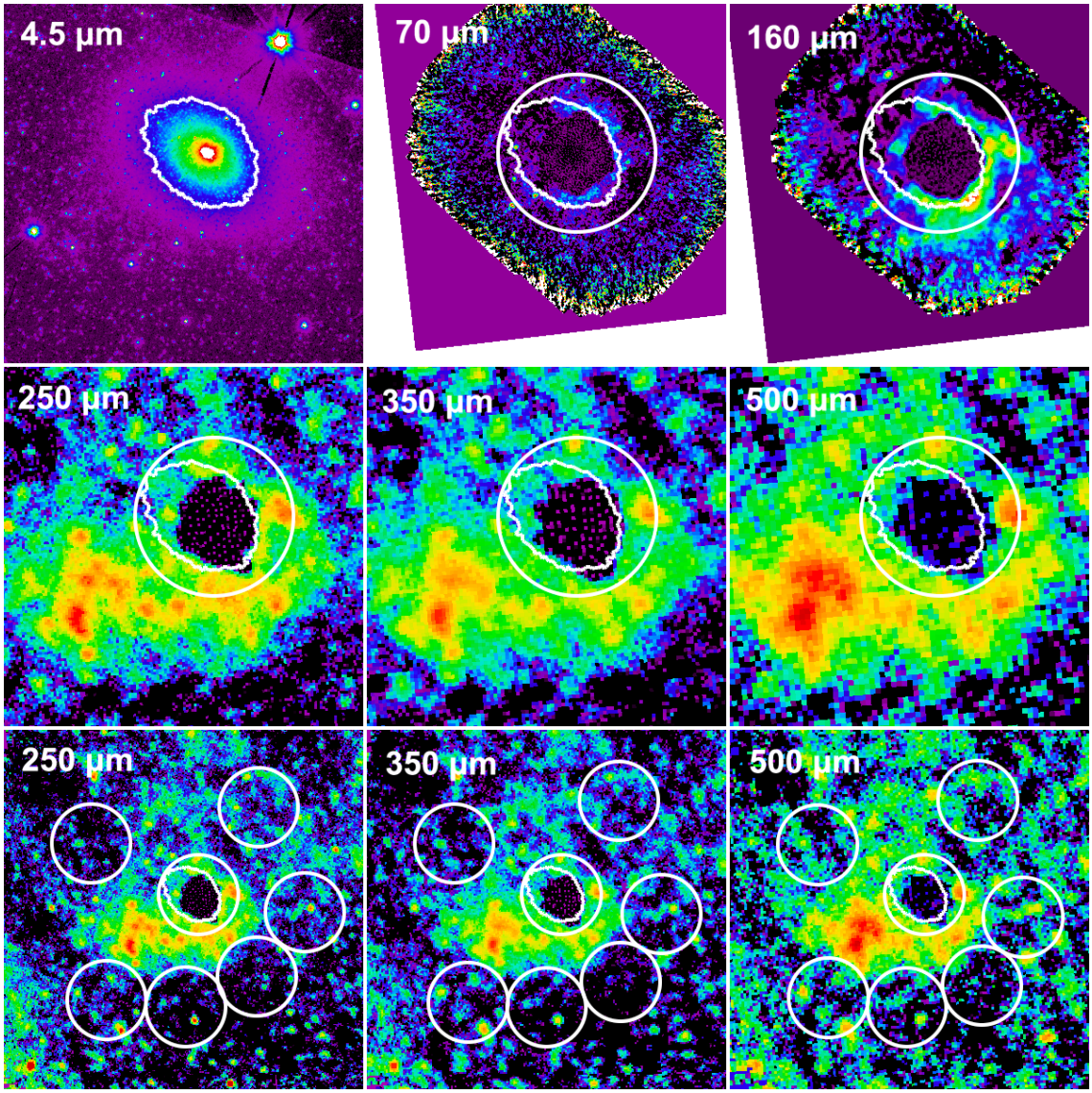

Figure 3.13: NGC 3077 - display is the same as in Figure 3.9.

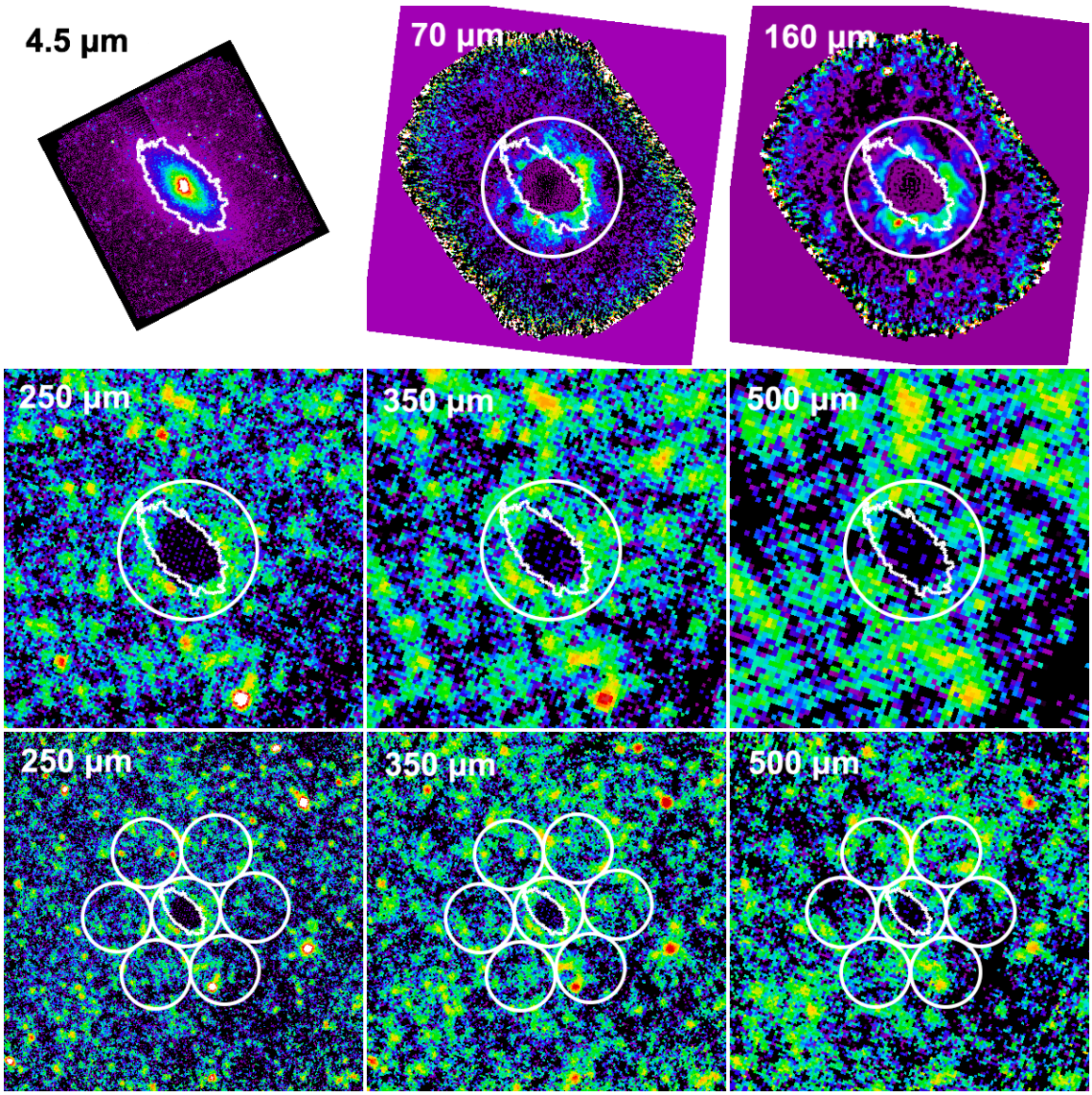

Figure 3.14: NGC 5253 - display is the same as in Figure 3.9.

out of the disk region into the circumgalactic region is added back into the disk flux total.

We also took sample flux measurements in darker, mostly source-free sky regions outside the global flux regions to confirm whether *Scanamorphos* had properly removed the background in the *Herschel* maps. The background regions in the PACS maps contained flux values close enough to zero as to be indistinguishable from noise. However, the backgrounds of the SPIRE maps still contained enough flux from either background sources or residual noise to require a background correction. We measured the flux in background regions identical in size and shape to the global region tiled around the global region perimeter. The bottom row of panels in each of Figures 3.9 - 3.14 shows the SPIRE background regions. We then averaged these background fluxes and subtracted the average to get the final SPIRE global flux measurement. The SPIRE background contribution fell somewhere in the 2-14% range (mean $\sim$ 8%) with NGC 1569 as an outlier at about 35% (weighted average of the regions shown in Figure 3.10) likely due to some contribution from the nearby Galactic cirrus.

We adopted a conservative flux calibration uncertainty of 10%, which consists of the systematic (4-5%), statistical (1-2%), and PSF/beam size (4%) uncertainties. The aperture sizes of the global regions in our sample had radii $\sim$ 110". Derived aperture corrections of order $\sim$ 3-4% [Paper I, Balog et al., 2014] are small compared to this calibration uncertainty. Color corrections[2] are on the order of 2-3% (for sources with a temperature of $\sim$ 30 K), which are also small compared with our 10%

[2]http://herschel.esac.esa.int/twiki/pub/Public/PacsCalibrationWeb/cc_report_v1.pdf

flux uncertainty. For sources with temperatures closer to 20 K, the color correction to the 70 μm PACS flux is 8%. The global, disk, and circumgalactic flux values are listed in Table 3.4.

Table 3.4: Global, Disk, and Circumgalactic Fluxes

	Global[a,b] (Jy)					Disk[a], c (Jy)					Circumgalactic[a,d] (Jy)				
Galaxy	70	160	250	350	500	70	160	250	350	500	70	160	250	350	500
He 2-10	24.206	19.260	6.696	2.543	0.878	24.014	17.965	5.993	2.153	0.757	0.192	1.295	0.703	0.390	0.121
NGC 1569	55.466	37.953	13.462	5.659	2.040	50.354	34.045	7.154	2.597	0.959	5.112	3.908	6.308	3.062	1.081
NGC 1705	1.234	1.372	0.593	0.292	0.125	1.228	1.284	0.498	0.274	0.104	0.006	0.088	0.095	0.018	0.021
NGC 1800	1.048	1.900	0.909	0.436	0.182	1.043	1.859	0.864	0.428	0.181	0.005	0.041	0.045	0.008	0.001
NGC 3077	17.897	22.071	10.115	4.204	1.539	17.832	20.955	8.649	3.535	1.313	0.065	1.116	1.466	0.669	0.226
NGC 5253	30.740	21.540	8.212	3.709	1.466	30.304	20.901	7.741	3.446	1.399	0.436	0.639	0.471	0.263	0.067

[a] Tabulated fluxes have a calibration uncertainty of 10%.
[b] Global fluxes measured in the 250, 350, and 500 μm SPIRE maps include background corrections.
[c] Disk fluxes are calculated: Global - Circumgalactic (see § 3.4.3).
[d] Circumgalactic fluxes are measured in the CLEAN residual images (see § 3.4.3).

3.4.4 Spectral Energy Distribution (SED) Fitting

In order to characterize the cold dust of each galaxy in our sample, we fit a modified blackbody (MBB) following the one found in Section 3.1 of Smith et al. [2012]. We fit the sets of 70, 160, 250, 350, and 500 μm global and disk flux values to:

$$S_\nu \;=\; \frac{M_d\ \kappa_\nu\ B_\nu(T_d)}{d^2} \tag{3.1}$$

where M_d and T_d are the dust mass and temperature respectively, d is the distance to the galaxy listed in Table 3.1, B_ν is the Planck function, and κ_ν is the dust absorption coefficient which has a power law dependence with dust emissivity index β where $\kappa_\nu = \kappa_0(\nu/\nu_0)^\beta$. κ_0 is the dust opacity at $\nu_0 = 350$ μm: 0.192 m^2 kg^{-1} [Draine, 2003]. We fit the parameters M_d, T_d, and β to each set of global and disk fluxes determining values for M_{global}, T_{global}, M_{disk}, T_{disk}. The fits also included the 10% flux calibration uncertainties. Fitting all three parameters often produced unphysical β values, so instead we fit just M_d and T_d and adopted a fixed value of $\beta = 2.0$, which is indexed to the dust opacity κ_0. Since the 70 μm flux value likely includes a contribution from a warmer dust component [Casey, 2012], we treated it as an upper limit in our MBB fits. For consistency, we did not include any 100 μm flux values in the MBB fits, since observations have not been done to match the depth of our 70 and 160 μm data. We estimated the uncertainties in the fit parameters by running 500 Monte Carlo MBB fits for each set of fluxes, which we let vary randomly within the associated uncertainties for each run. Figures 3.15

and 3.16 show the global and disk MBB fits, respectively, with the disk MBB fits shown for fluxes both before and after application of the CLEAN algorithm. The MBB fit parameters and the uncertainties estimated with the Monte Carlo method are listed in Table 3.5.

We also tried fitting the circumgalactic flux values to the same single MBB, but these fits produced unphysical results (e.g., unrealistically high dust masses). We believe this is due to the faint flux of the circumgalactic emission and the heterogeneous nature of this emission (e.g., filaments of different temperatures and masses which are not well represented by a single MBB). Due to these unphysical results, we calculated a circumgalactic cold dust mass using $M_{cg} = M_{global}$ - M_{disk}. Perhaps a detailed superposition of MBBs could reproduce the combined circumgalactic SED, but that avenue of analysis wades into more degenerate, subjective territory.

Our choice of the disk region depended directly on the distribution of stellar emission in the IRAC 4.5 μm band, but choosing a more or less conservative disk region as discussed in § 3.4.1 had an effect on the measured fluxes, MBB fits, and therefore the circumgalactic dust masses. Choosing smaller, less conservative disk regions (e.g., the white disk region in Figure 3.7) did produce a decrease of $\sim 10\%$ in the disk masses as well as an increase of ~ 1 K in the disk temperatures when fitting the MBBs. However, since the disk masses (M_{disk}) are similar in magnitude to the global masses (M_{global}) and we determined $M_{cg} = M_{global}$ - M_{disk}, a small decrease in the disk mass produces a proportionally larger increase in the circumgalactic mass (M_{cg}). With smaller, less conservative disk regions, we found circumgalactic masses $\sim$ 50-100% more massive than with the more conservative regions we have

chosen. Therefore our choice of the larger, more conservative disk region does not significantly affect the derived disk properties, but does produce a more conservative circumgalactic dust mass.

Table 3.5: Spectral Energy Distribution Fits

	Global			Disk			Circumgalactic[a]	Circumgalactic/Global[b]
Galaxy	$\log\left(\frac{M_{global}}{M_\odot}\right)$	β^c	T_{global}	$\log\left(\frac{M_{disk}}{M_\odot}\right)$	β^c	T_{disk}	$\log\left(\frac{M_{cg}}{M_\odot}\right)$	$\frac{M_{cg}}{M_{global}} = 1 - \frac{M_{disk}}{M_{global}}$
He 2-10	$6.43\ ^{+0.042}_{-0.047}$	2.00	27.7 ± 1.2	$6.33\ ^{+0.056}_{-0.064}$	2.00	29.0 ± 1.8	$5.74 \pm 73\%$	0.206 ± 0.035
NGC 1569	$5.85\ ^{+0.061}_{-0.071}$	2.00	25.7 ± 1.4	$5.30\ ^{+0.116}_{-0.161}$	2.00	34.9 ± 5.8	$5.70 \pm 24\%$	0.718 ± 0.246
NGC 1705	$5.12\ ^{+0.149}_{-0.228}$	2.00	20.8 ± 4.2	$5.03\ ^{+0.194}_{-0.359}$	2.00	21.3 ± 6.3	$4.37\ ^{+350\%}_{-100\%}$	0.178 ± 0.124
NGC 1800	$5.65\ ^{+0.074}_{-0.090}$	2.00	20.3 ± 1.3	$5.64\ ^{+0.199}_{-0.378}$	2.00	20.2 ± 6.6	$3.78\ ^{+4400\%}_{-100\%}$	0.014 ± 0.008
NGC 3077	$5.94\ ^{+0.045}_{-0.050}$	2.00	22.8 ± 1.2	$5.82\ ^{+0.044}_{-0.049}$	2.00	23.9 ± 0.9	$5.31 \pm 58\%$	0.236 ± 0.036
NGC 5253	$5.85\ ^{+0.104}_{-0.136}$	2.00	23.4 ± 2.2	$5.81\ ^{+0.107}_{-0.142}$	2.00	23.8 ± 2.1	$4.81\ ^{+410\%}_{-100\%}$	0.090 ± 0.035

[a] Circumgalactic dust mass was determined by subtracting the disk value from the global value (see § 3.4.4). The circumgalactic dust mass uncertainties come from the global and disk mass uncertainties added in quadrature.
[b] The circumgalactic / global dust mass uncertainties come from the global and disk mass *fractional* uncertainties added in quadrature.
[c] β values were fixed at 2.00 (see § 3.4.4).

3.5 Results and Discussion

3.5.1 Morphology

We find circumgalactic cold dust features for all six of our sample wind galaxies. The most extended features range from 1.2 kpc (NGC 1800) to 2.6 kpc (He 2-10) as measured from the center of the galaxy or from the mid-plane of a disk-like region out to the furthest part of the feature at least 3σ above the background. These features extend to scales of $\sim$1.2-2.5 times the radii of the stellar component as measured by the 4.5 μm stellar disk region, and typically do not trace the orientation of the stellar disk. The circumgalactic features vary in morphology including extended filaments (NGC 1569, NGC 1705, NGC 1800, NGC 3077, and NGC 5253), clouds or knots of dust apparently separated from the disk region (NGC 1569, NGC 1705, and NGC 5253), as well as broader regions extending over large circumgalactic angles (e.g., He 2-10). This varied morphology suggests different processes can lead to the presence of cold dust in circumgalactic regions. As a member of the M81 group, NGC 3077 is in the process of interacting with M81 and M82, so much of the circumgalactic cold dust features might be attributed to tidal stripping. In particular, the features to the east, west and north-northeast of NGC 3077 are likely due to tidal stripping mostly from M81, since 21 cm observations [Cottrell, 1976, van der Hulst, 1979, Yun et al., 1994] show H I tidal streams in those regions.

Some cold circumgalactic dust features coincide with similar emission features in the ancillary Hα, 8.0, and 24 μm data (e.g. filaments of NGC 1569 and NGC

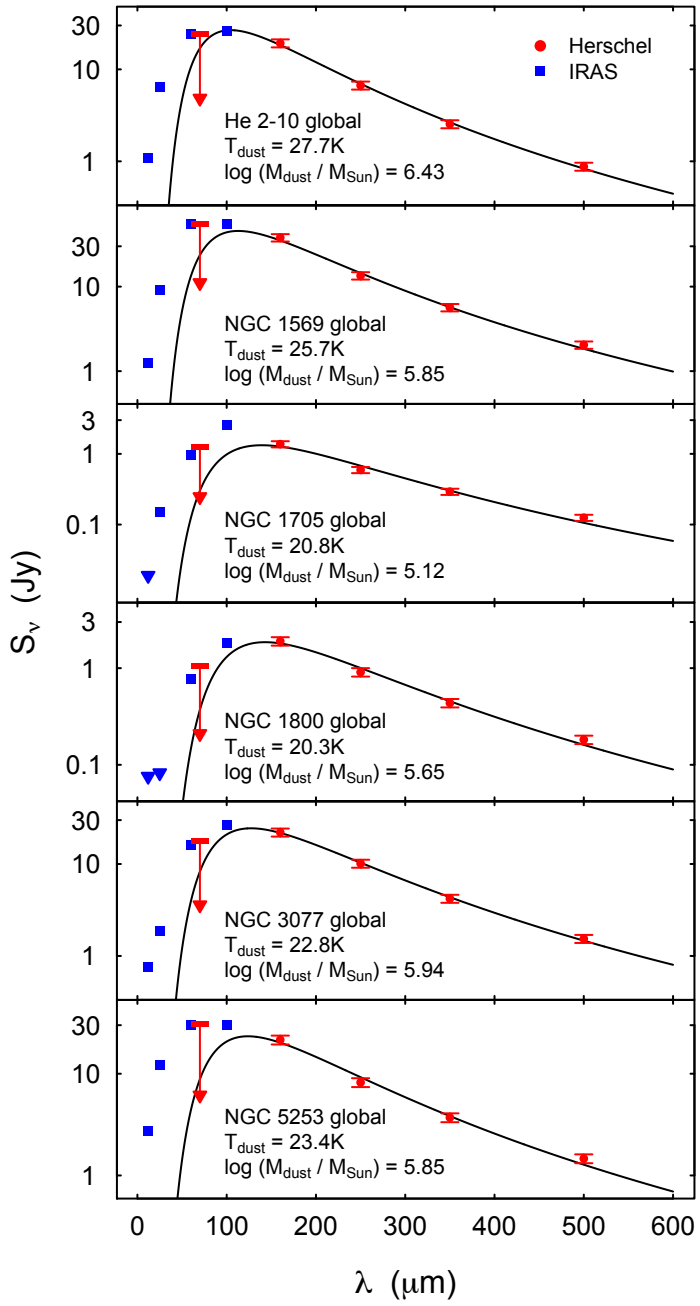

Figure 3.15: Modified blackbody fits for the global galaxy fluxes based on the 70, 160, 250, 350, and 500 μm *Herschel* bands (black lines and red points). In fitting, the 70 μm flux values were treated as upper limits as indicated by the downward arrows. The fit parameters are M_{dust} and T_{dust}. Refer to § 3.4.4 for details. Blue square points mark the *IRAS* fluxes at 12, 25, 60, and 100 μm [Moshir et al., 1990, Sanders et al., 2003], while blue downward triangles represent upper limits. The modified blackbody fits do not include the *IRAS* flux values since these data are shallower than our *Herschel* maps.

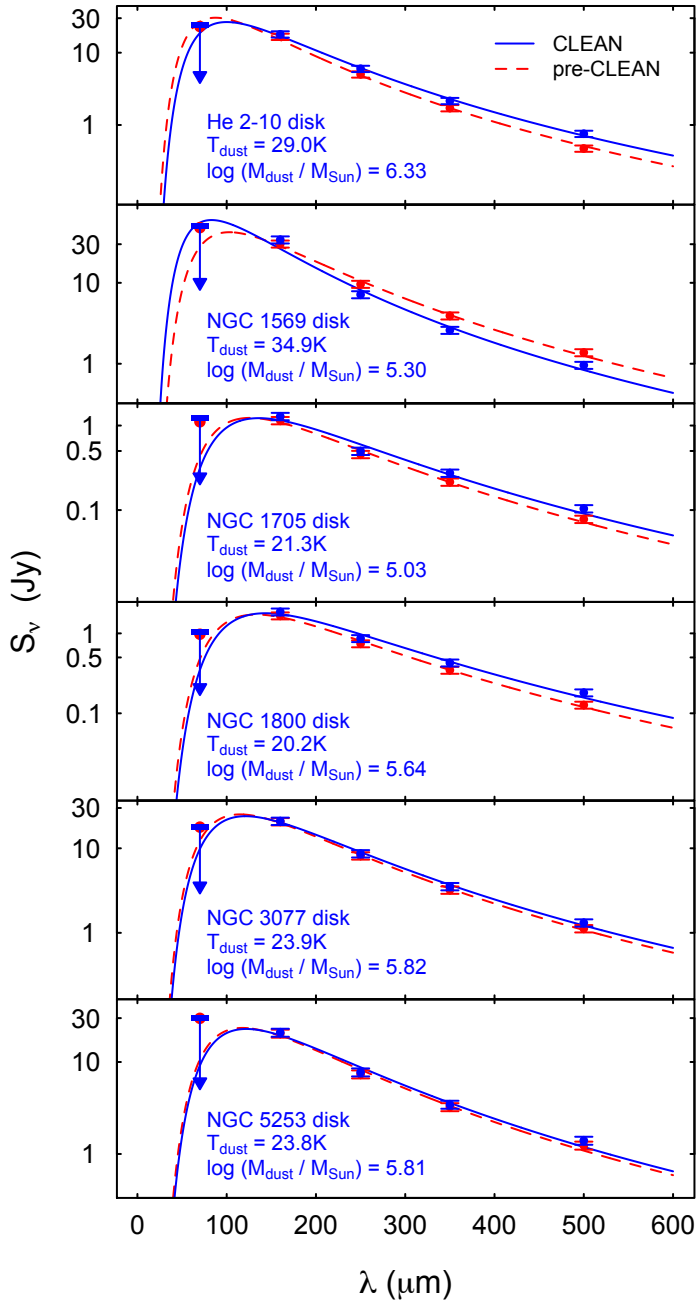

Figure 3.16: Modified blackbody fits for the galaxy disk fluxes based on the 70, 160, 250, 350, and 500 μm *Herschel* bands before (dashed red line) and after (solid blue line) applying our modified CLEAN algorithm. In fitting, the 70 μm flux values were treated as upper limits as indicated by the downward arrows. The fit parameters are M_{dust} and T_{dust}. Refer to § 3.4.4 for details.

1800), but others do not (e.g. the broader plume extending SSW from NGC 1705). Also, the cold circumgalactic features do not always match the morphology of their shorter wavelength counterparts. For example, the cold dust around NGC 1705 exhibits a somewhat filamentary morphology while the Hα features are more shell-like. Therefore, hot and warm wind components like Hα and polycyclic aromatic hydrocarbon (PAH) emission will not correlate exactly with the cold dust component, and should not be used as a predictor of cold dust or vice versa. This result supports the idea of shielded regions within a galactic wind where dust may remain protected from sputtering via thermal, radiation, or collisional processes [Jurac et al., 1998, Gnedin & Draine, 2014]. Appendix B contains further discussion of individual galaxies, their cold dust features, and comparisons with H I and X-ray observations.

3.5.2 70μm / 160μm Ratio Maps

In order to estimate the dust temperature and its spatial distribution using a proxy measurement, we made ratio maps of the 70μm to 160μm emission. The dust emissivity, β, and dust grain size distribution can also contribute to variations in 70μm / 160μm values (see Paper I). We first convolved the 70μm maps to the pixel scale of the 160μm maps using the convolution kernels described in Aniano et al. [2011]. We then aligned the resulting convolved images with the 160 μm maps and took the ratio, limiting the plotted ratios to pixels where the 160 μm map had values >0.0001 Jy/pixel ($\sim 1\sigma$ above the background) for the sake of clearly displaying galactic features. The 70μm / 160μm ratio maps are shown in Figure 3.17. All

of the galaxies exhibit warmer dust temperatures (ratio >1.0) near their nuclei as would be expected for the stronger radiation field in nuclear regions, while their outer regions tend to appear cooler. Unlike the rest of the galaxies, NGC 3077 has a striking temperature gradient along the northeast to southwest axis. Observations have shown the tidal features of NGC 3077 are significantly cooler than the galaxy itself [Walter et al., 2011]. The cooler dust to the southwest of the nucleus appears to coincide with warm dust in the 8.0 and 24 μm maps and the H I tidal stream towards M81 [Cottrell, 1976, van der Hulst, 1979, Yun et al., 1994], but not any obvious Hα feature. The warmer regions in the ratio maps shown by yellow and red colors in Figure 3.17 do not appear to correlate well in a qualitative sense with much of the warm dust features in the 8.0 and 24 μm maps or hot ionized gas of the Hα maps, though some exceptions arise like the bright filament to the southwest of NGC 1569 and the warmer region to the east of the nucleus in NGC 5253 coinciding with the ionization cone reported by Zastrow et al. [2011]. The temperature structure of He 2-10 exhibits a more disturbed temperature distribution than the other galaxies. At least three distinct warmer regions outside the nucleus extend in twisting filaments rather than a smooth gradient, perhaps due to anisotropic heating via AGN activity in its nucleus [Reines et al., 2011].

3.5.3 Comparing Dust and Host Galaxy Properties

Table 3.5 lists the cold dust masses and temperatures of each galaxy fit via MBB for both the global and disk regions. The fit global cold dust masses are in

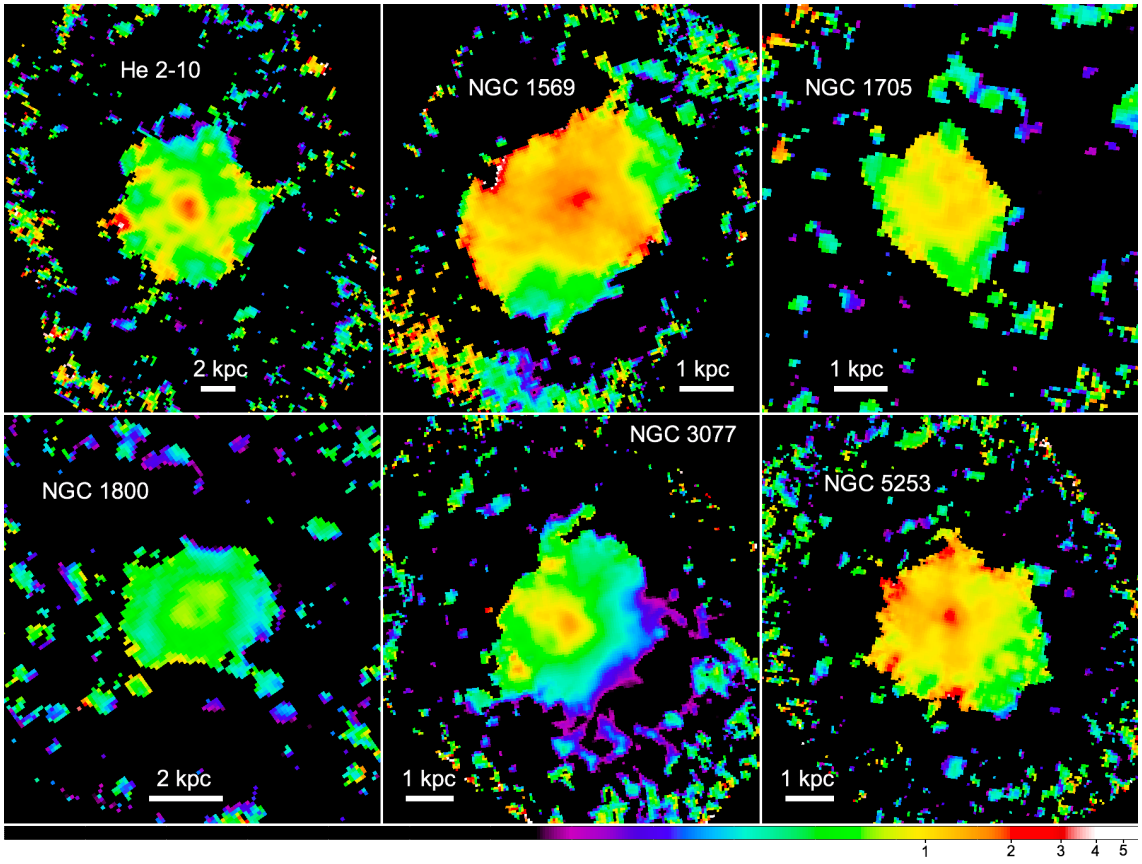

Figure 3.17: 70μm / 160μm ratio maps. All maps are shown with the same logarithmic scale indicated by the color bar. The white bar in each panel indicates the scale of each image. North is up and east is to the left in all images.

the range $\sim 10^5$ - $10^{6.5}$ $M_\odot$. We list H I and H_2 gas masses taken from the literature in Table 3.1. The total gas mass (H I + H_2) for the galaxies in our sample is in the range $\sim$1.5 - 9.0 $\times$ 10^8 $M_\odot$. Comparing these with the respective global dust masses, we estimate gas-to-dust ratios of in the range $\sim$ 200 - 1500 suggesting these galaxies are dust-poor compared to the the Milk Way ratio of $\sim$ 140 from Table 2 in Draine et al. 2007 (H_2 gas mass to dust mass ratios range from $\sim$ 4-800).

We calculated the circumgalactic cold dust mass (M_{cg}) shown in Table 3.5 by

subtracting the disk cold dust mass (M_{disk}) from the global cold dust mass (M_{global}). Figure 3.18 shows M_{cg} versus the total baryonic (stellar plus gas) mass for the galaxies in our sample. The stellar masses (M_*) are listed in Table 3.1 and were calculated using the same method as Zastrow et al. [2013] (see Table 3.1 for more detail). The circumgalactic dust, which likely manifests due to 10^7 year timescale star formation-driven winds or 10^8 year timescale tidal processes, exhibits a weak (Pearson's r = 0.76) positive correlation with the baryonic mass, which results from the 10^9 year timescale process of galaxy formation.

In Figure 3.19, we show M_{cg} normalized by M_{global} versus star formation rate surface density (Σ_{SFR}, see Table 3.1) using the star formation rate as calculated above together with the extent of the Hα emission ($R_{H\alpha}$) listed in Table 1 of Calzetti et al. [2010]. We did not correct for possible AGN contributions to the FIR emission in He 2-10, so its dust masses and star formation values carry that caveat, indicated by the open red circle for He 2-10 in Figures 3.18-3.22.

Although the typical dust mass uncertainties from the MBB fitting are on the order of $\sim$ 40%, Figure 3.19 still shows $\sim$10-20% of the cold dust in most of these wind-hosting dwarf galaxies can be found in the circumgalactic region, with NGC 1569 having $\sim$70% of its cold dust in the circumgalactic region. In the case of NGC 1569, it is possible our measurements are missing very cold dust in giant molecular clouds within the disk, thus over-estimating the dust fraction in the circumgalactic region. However, the H_2 gas mass value in Table 3.1 is only about 1% of the H I gas mass value, suggesting few hiding places for additional dust in the disk. Although the sky immediately surrounding NGC 1569 appears mostly free of Galactic

cirrus in the SPIRE bands, there is cirrus emission in adjacent regions. Therefore, NGC 1569 carries with it the caution that potential coincident foreground emission from Galactic cirrus might contribute some flux in the SPIRE bands, which would effectively increase the dust masses. Our estimate of contaminating background and foreground flux attempts to account for this by including a region (upper right ellipse in Figure 3.10) which includes some cirrus emission. If the flux contribution from Galactic cirrus to NGC 1569 was distributed just in the circumgalactic region to the exclusion of the disk region, then there would be an artificial increase in M_{cg} / M_{global}, but we find this scenario very unlikely. As another caveat, NGC 3077 may have an exaggerated circumgalactic dust mass from the dust contribution of tidal streams due to interaction with M81 and M82. These data also show no obvious trend in M_{cg}/M_{global} with Σ_{SFR}, as might be naively expected if the dust is lifted above the disk by energy inputs from star formation activity in the disk. Comparing the fitted global dust temperature (T_{global}) with Σ_{SFR} (Figure 3.20) provides tentative evidence for a positive trend, as would be expected from a more luminous ultraviolet (UV) radiation field in higher Σ_{SFR} galaxies. However, the dust temperature of He 2-10 may be increased due to the presence of an AGN [Reines et al., 2011], which would weaken the apparent dependence on Σ_{SFR}. Figure 3.21 shows the circumgalactic to global flux ratio (f_{cg} / f_{global}) versus Σ_{SFR} for the five PACS and SPIRE bands. The f_{cg} / f_{global} values tend to peak in the SPIRE bands, indicating the circumgalactic dust is typically cooler than the dust in the disk. This is consistent with the negative radial/vertical gradients generally detected in the 70-to-160 um flux ratio maps of these galaxies (see Figure 3.17).

Given the significant fraction of circumgalactic dust around the tidally disturbed NGC 3077 [Walter et al., 2011], it is natural to ask whether the immediate intergalactic environment plays an important role in stirring up circumgalactic dust. Karachentsev & Makarov [1999] developed a tidal index parameter (Θ_i) as a measure of the galaxy's interaction based on a combination of the three-dimensional distance and masses of its nearest neighbors. The maximum value of Θ_i determines the galaxy's "Main Disturber" (MD). A maximum Θ_i greater than zero indicates gravitational interaction with the MD within a tidal radius, while a value less than zero indicates a relatively isolated galaxy outside that tidal radius. Amongst our sample, NGC 1569, NGC 3077, and NGC 5253 have positive Θ_i values [Karachentsev et al., 2014], of which NGC 3077 unsurprisingly has the highest value. The circumgalactic dust of NGC 3077 is likely a combination of tidal dust streams and dust lifted into the halo via star formation. In contrast, He 2-10, NGC 1705, and NGC 1800 all have negative Θ_i, indicating their isolation and thus likely negligible contributions from tidal streams to the measured circumgalactic dust.

If a galaxy's dust carries fractionally more metals than its gas, infall addition or outflow removal of dust to or from the galaxy can significantly affect the overall ISM metallicity [Spitoni et al., 2010], though some controversy over these scenarios remains [Feldmann, 2015]. We determined a metallicity (12 + log(O/H)) for each galaxy in our sample using the emission line method developed in Pettini & Pagel [2004] (using ([O III]/Hβ)/(N II/Hα)) with emission line strengths from a few sources (see Table 3.1). In order to compare these metallicities with the mass-metallicity relation derived in Tremonti et al. [2004], we used the metallicity calibration con-

version found in Kewley & Ellison [2008] to calculate analogous values, taking into account the ∼0.1 dex uncertainty in the Pettini & Pagel [2004] method as well as the ∼0.06 dex uncertainty in the conversion [Kewley & Ellison, 2008]. The converted values are listed in Table 3.1. The mass-metallicity relation derived in Tremonti et al. [2004] is:

$$12 + \log(O/H) \;=\; -\,1.492 + 1.847(\log M_*) - 0.08026(\log M_*)^2 \qquad (3.2)$$

where O/H is the oxygen abundance and M_* is the stellar mass in units of solar masses. The equation is valid over the mass range $8.5 < \log\, M_* < 11.5$. We used this relation and the M_* values listed in Table 3.1 to calculate the predicted value of 12 + log(O/H)$_{pre}$. We have taken Solar metalicity to be 12 + log(O/H) = 8.69 [Allende Prieto et al., 2001].

In Figure 3.22, we calculate a metallicity deficit (Δ log(O/H)) by subtracting 12 + log(O/H)$_{pre}$ from the value derived from emission line strengths and compare that to M_{cg}/M_{global}. In NGC 3077 and He 2-10, dusty tidal streams and AGN should be considered respectively when interpreting Figure 3.22. The tidal streams of NGC 3077 likely increase M_{cg}/M_{global}, even though our observations do not cover the entire spatial extent of the streams when compared with the H I data [Cottrell, 1976, van der Hulst, 1979, Yun et al., 1994, Walter et al., 2011]. The AGN in He 2-10 [Reines et al., 2011] may eject and heat dust more efficiently, thus increasing M_{cg}/M_{global}. Also, log(O/H) can be underestimated in the presence of an AGN, which will contribute to raising [O III]/Hβ. With these considerations for NGC

3077 and He 2-10 in mind, the metallicity deficit of NGC 1569 in Figure 3.22 hints at a possible upward trend of M_{cg}/M_{global} with larger O/H deficits. In this context, it is interesting to see that the amount of metals locked in the dust of the cold outflow we found with our MBB fits (5×10^5 $M_\odot$, assuming most of the dust mass is in metals) is ~ 10 times larger than the mass of O detected in its hot outflow [3.4 $\times$ 10^4 $M_\odot$; Martin et al., 2002]. However, the uncertainties for all of our sample in both Δ log(O/H) and M_{cg}/M_{global} and the small number statistics preclude any statistically significant conclusions. Furthermore, recent results from large samples have shown the increased scatter in the mass-metallicity relation at lower masses [Zahid et al., 2012], which may further cloud the issue. Data from more galaxies would help clarify whether dust entrained in a wind can contribute to metallicity depletion.

3.6 Summary

In this second paper of a series (see Paper I), we have utilized new, very deep *Herschel Space Observatory* data of six nearby dwarf galaxies with known galactic-scale winds to investigate the detailed structure and properties of cold dust. *Herschel's* gains in resolution and light-collecting ability over earlier instruments (e.g., *Spitzer* MIPS) allowed us to resolve and detect previously unavailable details. Spatial decomposition of circumgalactic and disk regions has allowed us to investigate the properties of cold dust found outside the disk. Our analysis of these observations has yielded the following results:

- *Detection and kiloparsec-scale extent of cold dust features.* We detected circumgalactic cold dust features in all six of our sample of nearby dwarf galaxies with known galactic-scale winds. These features range in maximum extent from 1.2-2.6 kpc and are similar in scale to their host galaxy's stellar radii, but typically do not trace the stellar component.

- *Varied morphology.* We identified cold dust features with filamentary structure, dust clouds distinct from their host galaxies, and broad angle regions with more uniform emission distribution.

- *Imperfect spatial correlation with other wind components.* Some cold dust features we identified coincide with similar emission features in Hα, 8.0, and 24 μm data, but others do not, preventing the simple prediction of one component via another.

- *Significant fraction of the total dust mass found outside the stellar disk.* Through the spatial decomposition of circumgalactic and disk regions, we found that a substantial $\sim$10-20% of the total dust mass resides in the circumgalactic region. In the case of NGC 1569, this value is $\sim$70%.

- *Tantalizing correlations between dust properties and Σ_{SFR}.* Comparisons of global dust temperature with star formation rate surface density suggests a potential positive correlation, but the uncertainties in dust temperature as well as small number statistics make this conclusion tenuous at best.

- *Limited environmental dependence.* The presence of circumgalactic cold dust features for our dwarf galaxies doesn't obviously depend on the gravitational influence of neighboring galaxies, though it may play a role for certain sources (e.g., NGC 3077).

- *A hint towards metallicity depletion via cold dust outflow.* Comparing the fraction of circumgalactic cold dust mass with galaxy metallicity points towards a greater metallicity deficit in a galaxies with fractionally more circumgalactic dust, but uncertainties in the dust mass and metallicity plus small number statistics preclude any solid conclusion.

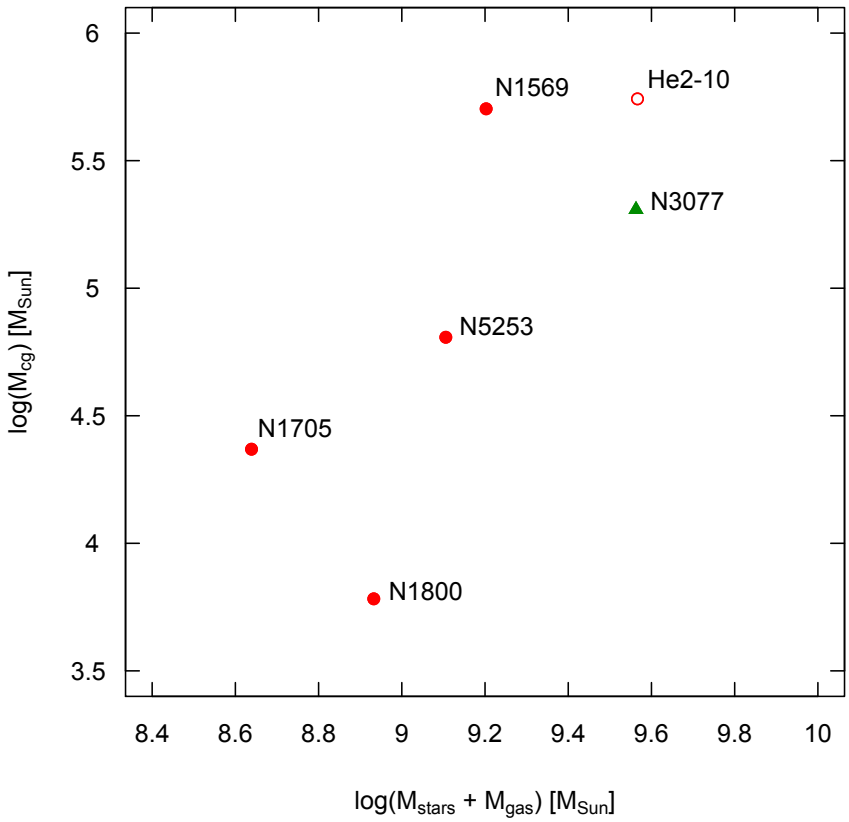

Figure 3.18: Circumgalactic dust mass versus total baryonic (stellar plus gas) mass, where the gas mass is the sum of the H I and H_2 gas masses. NGC 3077 is differentiated with a green triangle to indicate the likely tidal contribution to its circumgalactic dust features, and He 2-10 is differentiated with an open circle to indicate the possible AGN contribution to the FIR flux and therefore dust mass. With those caveats, this plot suggests a weak (Pearson's r = 0.76) positive correlation between circumgalactic dust mass and total baryonic mass.

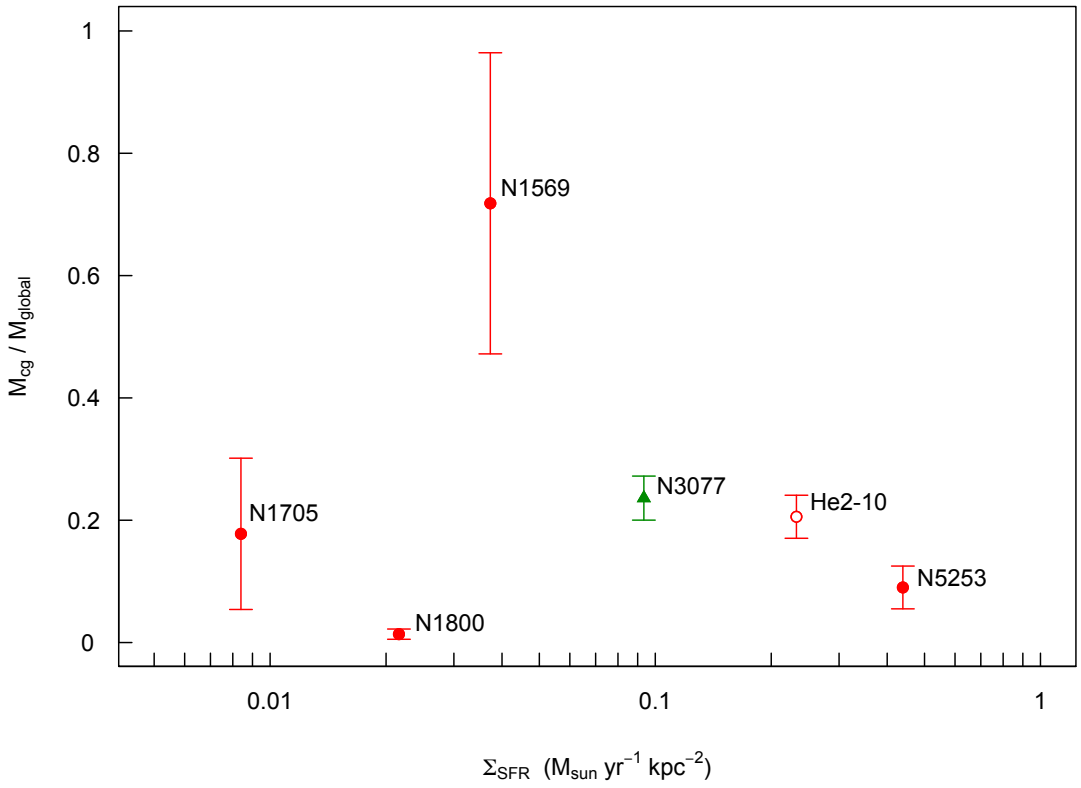

Figure 3.19: Circumgalactic dust mass fraction versus star formation rate surface density from Table 3.1. The uncertainty in M_{cg}/M_{global} comes from the uncertainties in the SED fitting (see § 3.4.4 and Table 3.5). Meaning of the symbols is the same as in Figure 3.18.

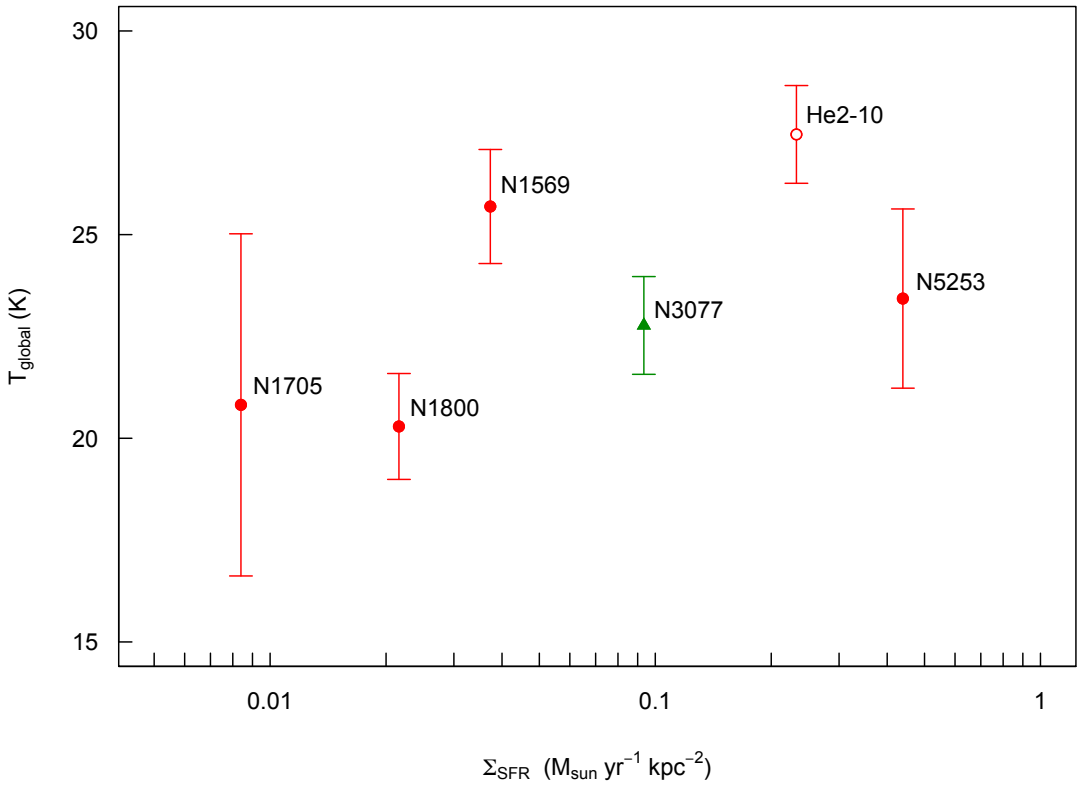

Figure 3.20: Global dust temperature from the modified blackbody fits versus the star formation rate surface density from Table 3.1. The uncertainty in T_{global} comes from the uncertainties in the SED fitting (§ 3.4.4 and Table 3.5). Meaning of the symbols is the same as in Figure 3.18.

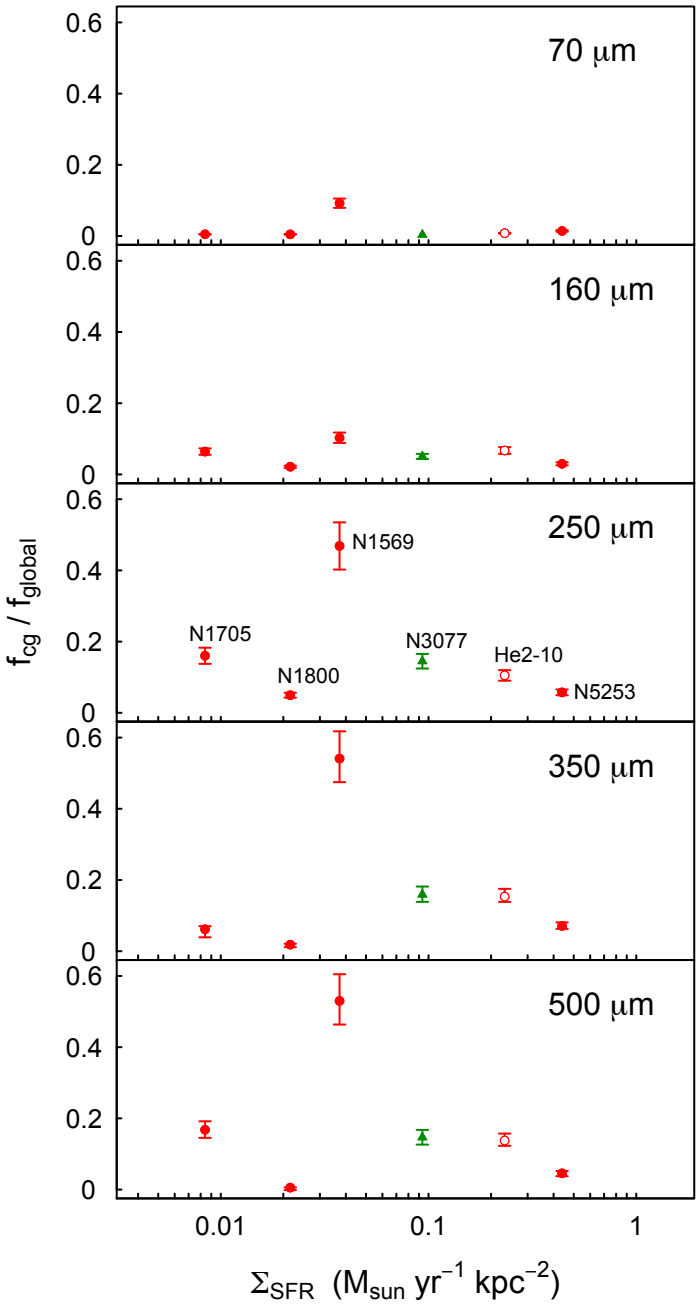

Figure 3.21: Circumgalactic flux fraction in each of the *Herschel* bands versus star formation rate surface density from Table 3.1. Meaning of the symbols is the same as in Figure 3.18.

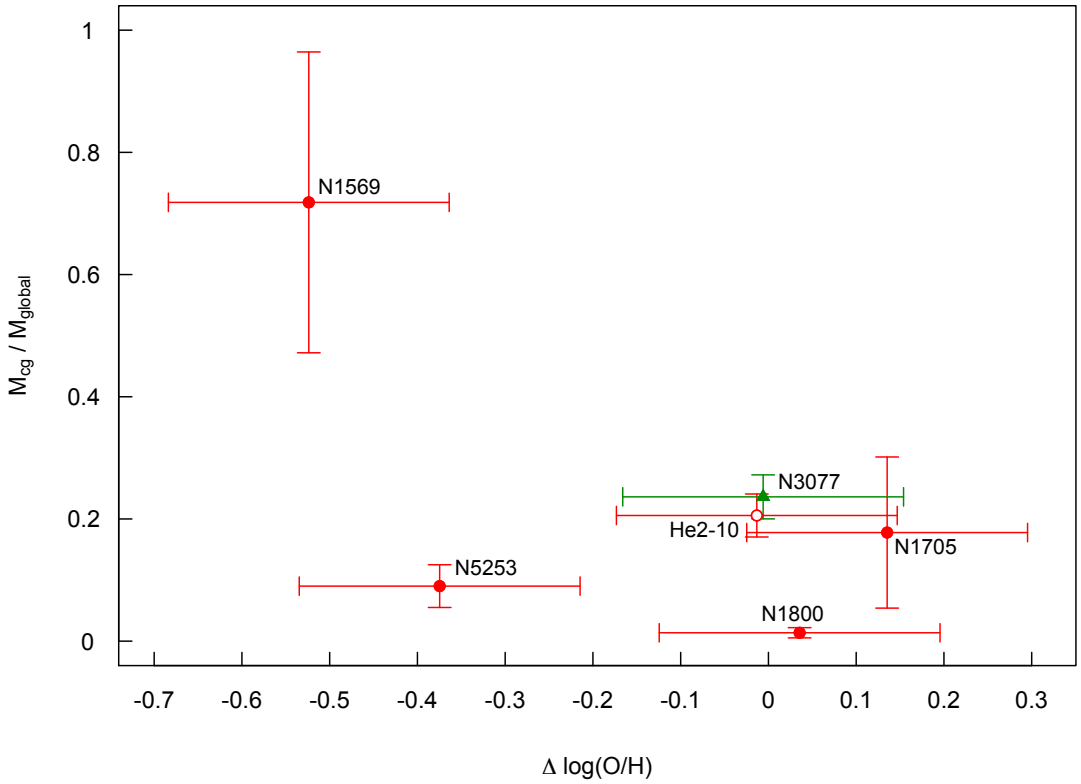

Figure 3.22: Circumgalactic dust mass fraction versus metallicity deficit, Δlog(O/H). Where Δlog(O/H) is the difference between the galaxy metallicity (see Table 3.1) and the metallicity predicted by the relation derived in Tremonti et al. [2004] between M_* and 12 + log (O/H). The uncertainty in Δlog(O/H) comes from uncertainty in the galaxy metallicity ($\sim$0.1 dex) and uncertainty in converting values to conform with Tremonti et al. [2004] ($\sim$0.06 dex). Meaning of the symbols is the same as in Figure 3.18.

Chapter 4

Summary and Future Work

4.1 Main Results

- *Frequent detection* - We detected extraplanar PAH emission or circumgalactic cold dust in nearly all of the nearby known wind galaxies in our samples, providing support for the ubiquity of dust in galactic winds.

- *Imperfect spatial correlations* - We compared our *Spitzer* and *Herschel* data with Hα, X-ray, H I, observations from the literature as well as data from collaborators and found imperfect spactial correlations with the ionized and highly-ionized components, some correlation with neutral hydrogen, and again imperfect spatial correlations with neutral gas in winds. These results suggest the division of winds into zones [as in Veilleux et al., 2005], which may be shielded from eachother.

- *kiloparsec-scale features* - In nearly all cases, we found extended PAH and dust features on kiloparsec scales. Explaining how dust survives out beyond

the stellar component while driven out by a galactic wind remains a challenge.

- *Correlation between f_{ePAH} and F_{IR}* - We found a nearly linear correlation of the flux from extraplanar PAH material with the total IR flux, suggesting a connection between star formation rate and PAHs being driven out of disk galaxies hosting a wind.

- *At least ∼10-20% of cold dust in the circumgalactic region* - By performing modified blackbody spectral energy distribution fits to our *Herschel* data, we determined that at least ∼10-30% of the dust mass in these known wind galaxies resides outside the stellar disk region. In the case of NGC 1569, the fraction may be as hight as 70%.

- *Hints at metallicity depletion and temperature correlation with Σ_{SFR}* - Although considerable uncertainties remain, there appears to be hints of a metallicity deficit in dwarf galaxies that have more dust outside their stellar disk region. Comparing the global cold dust temperature of dwarf galaxies with star formation rate surface density also hints at a correlation. However, these correlations are not statistically significant given the small number of objects in the sample and the uncertainties in the measurements.

4.2 Future Work

4.2.1 CTIO 4m Blanco Telescope - NEWFIRM

Building on the successful deep H_2 observations of M82 by Veilleux et al. [2009b], we will trace the morphology of the molecular wind-entrained material for a small but representative set of local wind galaxies using deep H_2 2.12 μm images obtained with the NEWFIRM camera on the Blanco 4-m telescope at CTIO. Table 4.1 contains a summary of the data we have obtained along with Margaret Trippe over the course of two 5-night observing runs (June 2-6, 2010 and October 20-24, 2010). Seeing was typically $\sim$ 1.1" for the observed IR wavelengths during both our runs. A. McCormick was the primary observer for the second run. We followed exactly the same method of Veilleux et al. [2009b]. The 4Q standard observing pattern was used with high-order Fowler sampling of 8 to obtain deep images of each target in the H_2 2.12 μm band, and K_s images were also obtained to derive continuum-subtracted emission-line maps of each object. This observational mode cycles the target through the four 2048 x 2048 pixel arrays, or quadrants, allowing for simultaneous off-target sky sampling.

Data Reduction and Analysis

We will follow the reduction method of Veilleux et al. [2009b], which uses NOAO NEWFIRM Science Pipeline version 1.0 to reduce the data [Swaters et al., 2009]. After the data are dark-subtracted, linearlized, and flat-fielded, a sky background

image will be determined for each exposure by taking the median of the four preceding and for subsequent exposures, but excluding exposures containing the galaxy. This sky image will then be scaled to match the sky background in the galaxy exposures and subtracted. Astrometric solutions will be obtained, and the data will be resampled and stacked. Next, we will produce a new stack by repeating the sky subtraction to mask out persistent images, bad pixels, and transient effects detected in the first pass. In order to isolate and measure H_2 emission, we will subtract an estimate of the continuum emission from the scaled K_s image stacks. The "pure" H_2 maps will be compared with previous observations at other wavelengths.

Table 4.1: NEWFIRM Data Summary

Galaxy	d (Mpc)	Morph. Type	Incl. (degrees)	H_2 2.12 μm (hr)	K_s (hr)
NGC 55	1.6	SB(s)m	80	5.0[1,2]	0.7[2]
NGC 253	3.46	SAB(s)c	76	4.7[1,2]	0.7[1]
NGC 1705	6.5	SA0	33	4.0[2]	0.7[2]
NGC 1808	12.3	(R)SAB(s)a	53	4.0[2]	0.7[2]
NGC 4945	3.55	SB(s)cd	79	4.0[1]	0.7[1]
NGC 5253	4.1	Im	68	4.7[1]	1.7[1]
Circinus	4.2	SA(s)b?	64	2.3[1]	0.7[1]

[1] Data taken during June 2-6, 2010 observations at CTIO.
[2] Data taken during October 20-24, 2010 observations at CTIO.

4.2.2 Expanding the Sample: Additional AGN

Our *Spitzer* sample only contained two "pure" AGN, but their extraplanar PAH emission suggested they are possibly less efficient at entraining PAHs in outflows, though there is some degeneracy with inclination effects. Expanding our sample to include more AGN-only galaxies would help determine whether this is a

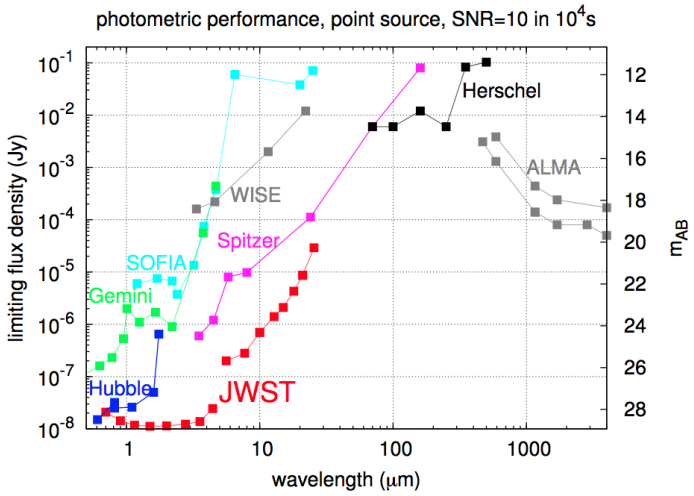

Figure 4.1: The future waveband coverage and photometric performance of the James Webb Space Telescope (JWST) compared with several current observatories. Source: Space Telescope Science Institute

feature of AGN galaxies hosting winds or just a few outliers.

4.2.3 Possible Future Observations

The coming launch of the James Webb Space Telescope (JWST) will usher in a new era of extragalactic IR astronomy. JWST provides the waveband coverage and sensitivity to observe the features of galactic winds we've identified and other, fainter features, but with much shorter observations. A plot showing the improved sensitivity and waveband coverage for JWST is shown in Figure 4.1.

Appendix A

Spitzer - Notes on Individual Galaxies

- NGC 55 (Figure 2.11): Faint PAH filaments extend from the southern edge of the disk's nuclear region in the 8.0 μm image, bracketing the eastern and western extent of the nuclear region. Some evidence also exists to suggest the base of a north eastern loop or shell structure similar in location to extraplanar ones observed in [O III] by Graham & Lawrie [1982] and Hα by Hoopes et al. [1996] and Otte & Dettmar [1999]. In contrast with the Hα observations of Ferguson et al. [1996] and Hoopes et al. [1996], we do not observe significant extraplanar PAH emission north of galactic disk.

- NGC 253 (Figure 2.12, top): Complexes of filamentary and halo-like PAH structures extend both north and south from the nuclear region of NGC 253. Two particularly prominent filaments extend north and south-east from the north-eastern area of the disk. The filament extending north appears to have an 'S'-like shape with two foreground stars superimposed over the upper portion of the 'S'. The PAH emission from the filament to the south-east extends

away from the nuclear region ∼5 kpc, making and angle of ∼65° with the outer part of the disk to the north-east. This same feature appears in Hα and X-ray [Strickland et al., 2002] as well as UV images [Hoopes et al., 2005]. The IRAC 8.0 μm image from this work exhibits more extraplanar emission south of the disk, whereas previous observations at other wavelengths [Pietsch et al., 2000, Strickland et al., 2002, 2004a,b, Hoopes et al., 2005] show more prominent emission to the north. Some faint, residual banding which could not be removed is present in the 8.0 μm image but does not contribute significantly to the total extraplanar flux.

- NGC 891 (Figure 2.12, bottom): A nearly disk-wide halo of extraplanar PAH emission extends approximately equal distances (∼5 kpc) to the east and west of NGC 891's disk. The disk-wide extent of the extraplanar PAH emission matches the morphology of extraplanar dust filaments observed by Howk & Savage [1997] near the disk in optical images and Hα and [N II] emission observed by Miller & Veilleux [2003]. In contrast, X-ray maps exhibit an asymmetry to the extraplanar emission preferentially towards the northwest with a ∼6 kpc filament extending from the nuclear region in that direction [Bregman & Pildis, 1994, Bregman & Houck, 1997, Strickland et al., 2004a]. Detailed inspection of the halo region reveals finger-like PAH features suggesting the presence of Rayleigh-Taylor instabilities, and reminiscent of the 'highly structured dust features' observed by Howk & Savage [1997, 2000]. Near the south-east edge of the disk, a rather prominent filament appears to be encir-

cled by a faint loop of PAH emission. Faint streaks parallel to the western edge of the disk and separated by about 4 and 5 kpc from the galaxy are due to ghost images of the galaxy's disk in the data, but these artifacts do not contribute significantly to the total extraplanar flux. As with NGC 253, some faint residual banding remains, but also does not contribute significantly to the total extraplanar flux.

- NGC 1482 (Figure 2.13, top): There are several filamentary PAH features extending from both sides of the disk in the 8.0 μm image. These features seem to extend approximately radially from regions near the nucleus. Previous Hα observations [Hameed & Devereux, 1999, Veilleux & Rupke, 2002] found an 'hourglass' morphology, consistent with a biconical outflow. The X-ray observations of Strickland et al. [2004a,b] showed a complementary, similar morphology. While there are some indications of similar structure in the 8.0 μm IRAC image, the PAH emission features seem more evenly distributed with filaments splayed out in all directions. This complementary, but contrasting morphology between Hα and PAH emission recalls the similar observations of M82 by Engelbracht et al. [2006]. The data reduction for NGC 1482 was particularly challenging, since it's bright nucleus is less like a point source than others in our sample. The large solid angle of high luminosity within the nuclear region leads to a smearing of the PSF wings and therefore more overlap with extraplanar regions. Our fit to the wings caused by the bright nucleus took into account the smearing. Therefore we were able to remove the

vast majority of the PSF wings, but the black crosshairs artifact in Figure 2.13 resulted from slight over-subtraction along the vertical and horizontal axes of the detector.

- NGC 1569 (Figure 2.13, bottom): This galaxy exhibits PAH features which, notably, do not all extending from the nuclear region or perpendicular to the disk region's major axis. Several of the brightest, large scale features extend from regions near the edges of the disk. In particular, a filament extends southwest from the western edge of the galaxy (the 'arm' identified by Waller [1991]), and two filaments from the eastern edge of the galaxy curl towards the northeast in the image. Much of the extraplanar PAH emission morphology matches Hα features previously observed by Hodge [1974], Waller [1991], Hunter et al. [1993], though some differences can also be observed - primarily the smaller extent of the extraplanar PAH features, and their more uniformly distributed emission as compared with the more filamentary Hα features. The bright star to the north of the galaxy generated particularly bright PSF wings, so it's removal in the 4.5 μm image left some artifacts, such as the half-moon shaped feature just north of the star. Also, some very faint pixels north of the galaxy in the 8.0 μm image coincide with a region where banding could be expected even after our best efforts at correction (near the top edge of the 8.0 μm image: Figure 2.13, bottom right), so the authenticity of these as PAH emission is questionable at best.

- NGC 1705 (Figure 2.14, top): We did not find significant extraplanar PAH

features in comparing the IRAC images. This result is somewhat surprising considering the strength of the bipolar Hα emission observed by Meurer et al. [1989, 1992]. The 8.0 μm image exhibits clumpy star forming regions similar to those observed by Melnick et al. [1985].

- NGC 1808 (Figure 2.14, bottom): Due to the lower inclination of NGC 1808, the portions of extraplanar PAH features closest to the disk coincide with or are occulted by the disk, making them more difficult to distinguish. The lower inclination also causes an underestimate in the extraplanar PAH flux measurement. Extraplanar PAH features extend both from the northeastern and southwestern edges of the disk. Several filaments can be observed within a more diffuse halo of PAH emission which appears more prominent on the northeastern side of the disk. The brightest of these filaments appear similar to optical absorption features observed by Phillips [1993], and the diffuse PAH halo is somewhat similar to the Hα morphology described by Sharp & Bland-Hawthorn [2010]. The tidal tails to the northwest and southeast also exhibit bright PAH emission. Some residual banding remains both to the east and west of the disk (see masking in Figure 2.7).

- NGC 2992 (Figure 2.15, top): In tracing the PAH emission, we recovered structures similar to the biconical outflow identified in Hα by Veilleux et al. [2001], but unlike radio [Ward et al., 1980, Hummel et al., 1983, Colbert et al., 1996, Gallimore et al., 2006] and X-ray [Colbert et al., 1998] maps, which primarily show extended features east of the nucleus. Particularly, filamentary

PAH emission features extend out from the nucleus in a nearly radial direction (most easily seen as dark blue features in Figure 2.15). The northern tidal tail due to NGC 2992's interaction with NGC 2993 (not shown in the field of view) does coincide with the extraplanar PAH features on the west side of the disk, but the different morphologies allow for the distinction of filaments versus tidal tail. Emission from the coincident tidal tail to the west as well as the tidal filament extending almost directly south contributes to the extraplanar PAH flux measurement, but these components are not easily disentangled. As with NGC 1482, we fit the PSF wings of the bright nucleus, but the image was slightly over-subtracted in certain areas (the black lines emerging from the nucleus along the minor axis).

- NGC 3079 (Figure 2.15, bottom): Extraplanar PAH features extend both from the eastern and western edges of the disk. Several filaments can be observed within a bright halo of PAH emission, which is thickest out to ~ 8 kpc radially from the nucleus. In particular, two PAH filaments separated by about 5 kpc along the eastern edge of the disk and bracketing the nuclear region (light blue in Figure 2.15) as well as another filament south of the nucleus along the western edge of the disk extend outward similar to the X-shaped morphology observed by Heckman et al. [1990] in Hα and by Dahlem et al. [1998], Pietsch et al. [1998], Strickland et al. [2004a] in X-ray maps. We do not observe any PAH features near the nuclear region suggestive of the well-known superbubble which resides there [Ford et al., 1986, Cecil et al., 2001].

- NGC 3628 (Figure 2.16): Two prominent artifacts remain in the 8.0 μm image after the data reduction. Faint streaks parallel to the northern edge of the disk and separated by $\sim$ 2,3 and 7 kpc from the nuclear region of the galaxy are due to ghost images of the galaxy's disk in the data. These artifacts were masked and excluded from the extraplanar region during the extraplanar PAH flux measurement (see Figure 2.7). Some residual banding extends north of the disk from the bright nucleus and was also excluded from the flux measurement. In addition to these artifacts in the 8.0 μm image, the filament rising at an acute angle from the northwestern edge of disk appears to extend in the same direction as the tidal tail observed by Kormendy & Bahcall [1974], Haynes et al. [1979] and Chromey et al. [1998], suggesting it does not result from a wind. The most prominent non-artifact, non-tidal, extraplanar PAH features are a faint cloud of emission separated from the northeastern edge of the disk by about 1 kpc, a brighter protrusion from the southeastern edge of the disk and a bit closer to the nucleus, and perhaps a 2 kpc loop of PAH emission from the far southwestern edge of the disk. There may also be some faint emission coincident with the region just southwest of the nucleus where extended Hα [Fabbiano et al., 1990] and outflowing molecular material [Irwin & Sofue, 1996] have been observed, but certainly not on the same scale or bright enough for confirmation in the IRAC data. The morphology of these faint features does not match the X-ray emission seen extending from the disk in previous observations [Fabbiano et al., 1990, Dahlem et al., 1996, Strickland et al., 2004a].

- NGC 4388 (Figure 2.17, top): Apart from a halo which extends north and south of the disk, very little extraplanar PAH emission can be observed. Some faint residual banding similar to that of NGC 891 can be seen in the 8.0 μm image, but it does not contribute significantly to the total extraplanar flux. Also, the fainter band in the disk directly north of the nucleus resulted from PSF subtraction, and not any real feature in the data. We see little to no evidence of extraplanar PAH emission coincident with the region where Veilleux et al. [1999] observed a complex of highly ionized gas extending north of the nucleus. Nor do we see a PAH analog to the extended, nuclear radio emission [Hummel et al., 1983, Stone et al., 1988].

- NGC 4631 (Figure 2.18): Two $\sim$ 3-4 kpc-scale filaments extend from the southeastern edge of the disk. Some fainter protrusions show up just south of the nuclear region. Also, a dense region of apparent Rayleigh-Taylor instability 'fingers' and filaments covers the entire central portion of the northern disk edge. The PAH filaments north of the disk appear brighter than any features south of the disk, which matches well with previous Hα and X-ray observations [Dahlem et al., 1998, Wang et al., 2001, Strickland et al., 2004a].

- NGC 4945 (Figure 2.17, bottom): Filamentary extraplanar PAH features extend from all regions of this galaxy's disk. The southeastern edge of the disk exhibits the highest concentration of filamentary features, where a dense region of plumes is bright against the background. Filaments northwest and directly north of the nuclear region extend up from the disk and radially out-

ward suggesting similar structure to the wide cone-like feature observed in broadband optical emission by Nakai [1989] and in line splitting by Heckman et al. [1990] (perhaps better seen in the optical image shown by Elmouttie et al. [1997]). We do not see evidence in the PAH emission for the narrower conical wind-blown cavity observed in Hα and H II [Moorwood et al., 1996], as well as X-ray [Strickland et al., 2004a]. The clear presence and morphology of extraplanar PAH emission filaments at large galactic radii suggests much of the extraplanar PAHs were ejected from regions well outside the starburst disk or ring traced by Brγ and L band imaging [Moorwood et al., 1996]. Since NGC 4945 is quite near the Galactic plane ($b \approx 13°$), these PAH filaments at large galactic radii may not appear to have analogs in previous observations at other wavelengths due to Galactic absorption as noted by Colbert et al. [1998] and Strickland et al. [2004a].

- NGC 5253 (Figure 2.19, top): As with our data reduction for NGC 1482, the 8.0 μm PSF was slightly over-subtracted along the vertical and horizontal axes after fitting and subtracting the PSF wings. Also, ghost image artifacts near the nucleus appear as multiple point sources in the 8.0 μm image. Extraplanar PAH filaments seem to extend approximately radially from the nuclear region in most directions. Filaments to the east and west match up somewhat with previous observations of Hα filaments [Marlowe et al., 1995, Martin & Kennicutt, 1995]. However, more prominent PAH emission to the southeast of the nucleus coincides with an H I plume which has been interpreted as a

tidal remnant or inflow [Kobulnicky & Skillman, 2008]. The filaments of PAH emission to the west of the nucleus appear to extend into the region where a "quiescent" (neither outflowing nor inflowing) Hα bubble has been observed [Martin, 1998].

- NGC 6810 (Figure 2.19, bottom): At first look, some of the radially-oriented PAH features (light blue in Figure 2.19) around the nucleus in the 8.0 μm image appeared conspicuously similar to the wings of the SSC-provided PRF. However, upon fitting a PSF to the galaxy's nucleus, we found that there was little to no contribution to the extraplanar features from the PSF. Therefore, the extended extraplanar PAH emission features appear as two galactic-scale bubbles emerging from either sides of NGC 6810's nuclear region. This dust morphology resembles the X-ray features observed by Strickland [2007] more closely than Hα maps, which include a prominent filament extending toward the north-west, confirmed by Strickland [2007] after noting its presence in the observations of Hameed & Devereux [1999].

- M82 (Figure 2.20): We recovered the same widespread extraplanar PAH emission observed by Engelbracht et al. [2006] and also found a consistent value for the extent of the features (z_{ext} = 6.0 kpc). As discussed by Engelbracht et al. [2006], the extraplanar PAH emission is not confined to the biconical wind region as defined by the extraplanar Hα [e.g., Lehnert et al., 1999], X-ray [Strickland et al., 2004a], and UV [Hoopes et al., 2005] emission, but within that region it has similar structure to the tracers at other wavelengths. See

the discussion of Engelbracht et al. [2006] for more detail.

Appendix B

Herschel - Notes on Individual Galaxies

For the discussion in these notes, please refer to:

Figures 3.1 - 3.6 and Figures 3.9 - 3.14.

- *Henize 2-10* - Broad cold dust emission regions surround He 2-10 out to $\sim$ 1.5 kpc in all SPIRE bands as well as the 160 μm PACS map, which appears similar in extent and morphology to the H I distribution observed by Kobulnicky et al. [1995]. The 70 μm PACS map exhibits a bit more anisotropy in its distribution of circumgalactic emission with tapering features extending to the north-northeast, southwest, and east-southeast. The north-northeast tapering feature extends furthest to $\sim$ 2.6 kpc. The orientation of these tapering features appears similar to the smaller 0.5 kpc-scale Hα bubbles [Méndez et al., 1999, Zastrow et al., 2013], but appears less correlated with the shape of the X-ray emission [Kobulnicky & Martin, 2010]. Several knots of emission separated from He 2-10 by $\sim$3-4 kpc to the northwest and southwest in the PACS maps cannot be definitively ruled out as background sources given the

signal to noise levels or foreground Milky Way dust clouds, but coincident emission in the SPIRE maps seems connected to the disk via colder streams bridging their separation. The most prominent emission in the SPIRE maps towards the knots northwest of the disk seems similarly oriented to an X-ray feature observed by Kobulnicky & Martin [2010].

- *NGC 1569* - A dense complex of filamentary and broad circumgalactic cold dust features stretch out from all along the disk of NGC 1569. The prominent Hα, 8.0, and 24 μm filament [Waller, 1991, Hunter et al., 1993, Westmoquette et al., 2008, McCormick et al., 2013] extending southwest from the western edge of the disk also shows up in the PACS maps, but becomes fainter and disappears in the SPIRE bands. A clump of cold dust directly south of the galactic nucleus resides $\sim$1.8 kpc from the disk midplane and appears to have made a clean break with the other circumgalactic cold dust emission in the PACS maps. Some faint 8.0 μm emission [McCormick et al., 2013] coincides with this rogue clump and some extended X-ray emission [Heckman et al., 1995, della Ceca et al., 1996] may as well. The rogue clump has no obvious counterpart in Hα emission, but supershell features surrounding its location [Martin, 1998, Westmoquette et al., 2008] suggest it resides at the center of a ionized gas shell. The structure of the rogue clump suggests anisotropic heating with the warmer 70 μm emission closer to the galactic disk and the colder emission in the SPIRE maps extending further away. The bright emission to the southwest corner of the SPIRE maps comes from foreground Milky Way

cirrus. *Note*: Some dispute remains about the distance to NGC 1569 [Grocholski et al., 2008]. We have adopted the distance determined by Grocholski et al. [2008], which employs *Hubble Space Telescope* data and the tip of the red giant branch to obtain a z-independent distance of 3.36 Mpc, but the range of other distances 1.9 - 3.4 Mpc leads to a range of different star formation rate values.

- *NGC 1705* - Vertical filamentary cold dust emission to the north and south of NGC 1705 coincides with the H I emission, which Meurer et al. [1998] has shown consists mainly of a rotating disk. However, Meurer et al. also note an H I "spur" which is kinematically distinct from the the rotating disk and spatially consistent with the Hα outflow [Meurer et al., 1989, 1992, Zastrow et al., 2013]. Our PACS maps show evidence of a similarly consistent cold dust feature extending almost exactly north from the galaxy. Also in the PACS maps, two bright knots of emission directly to the south are separated from the galactic center by $\sim$1.3 and 1.5 kpc respectively. These knots are also approximately coincident with the rotating H I disk, also appear in the SPIRE maps, and do not have associated background sources. North-northeast of the nucleus, a bright cloud of cold dust appears as a knot in the 70 μm PACS map but has broader spatial extent in our other four *Herschel* maps. This cloud with no obviously associated background source seems spatially consistent with the orientation of the northern Hα superbubble [Zastrow et al., 2013], but resides well beyond its edge (>0.5 kpc), making it a likely example of

material swept out of the ISM by an expanding superbubble. However, we did not include this cloud in the global flux measurements, since it cannot be definitively ruled out as a background source.

- *NGC 1800* - An C-shaped filament of circumgalactic cold dust extends from the northwestern edge of NGC 1800 to ∼1.2 kpc north of the disk in the 70 μm PACS map tracing a similar feature in 8.0 μm emission. In addition there is some more diffuse, less bright 70 μm emission above the disk to the east of this filament. These features lie just south of the filamentary web of Hα emission [Hunter et al., 1994, Marlowe et al., 1995, Hunter, 1996]. The cold dust features along the northwestern edge of NGC 1800 are offset from the Hα "fingers" of Hunter [1996], which extend from the the northeastern edge of the disk. An offset also exists between the southern edge cold dust features which appear like two broad nubs splayed out from the eastern and western edges of the disk in our SPIRE maps versus the centrally concentrated Hα "fingers" and shell outside the disk (again from Hunter 1996). Observations by Rasmussen et al. [2004] reveal X-ray emission crossing the disk of NGC 1800 approximately from southeast to northwest at an angle with respect to the stellar component. The northern extent of this hot X-ray gas above the disk appears to coincide with some of the emission from cold dust in the PACS maps. Within the galactic disk, the peak of the dust emission is offset to the west from the stellar component, perhaps helping explain why the strongest dust feature - the C-shaped filament extending north - emanates from that part

of galaxy. This offset between dust and stellar emission might be explained by ram pressure stripping, but the galaxy appears to be relatively isolated [Karachentsev et al., 2014]. What may appear as cold dust knots to the south in the PACS images could also be either Galactic dust heated by foreground Milky Way stars or emission from background sources evident in the 4.5 μm IRAC map.

- *NGC 3077* - Most if not all of the circumgalactic cold dust features we observe for NGC 3077 can be attributed to the same tidal interaction forces with M81 and M82, which produce tidal arms of H I and the complex of H I and CO offset to the east of the galaxy's stellar component [Cottrell, 1976, van der Hulst, 1979, Yun et al., 1994, Walter & Heithausen, 1999]. However, certain cold dust features appear to complement the morphology of the Hα emission [Martin, 1998, Calzetti et al., 2004]. A C-shaped filament and a knot of cold dust at its tip extending $\sim$2.6 kpc north of the stellar disk (see 70 & 160 μm maps) reside directly above the location of an Hα shell [Calzetti et al., 2004]. A circumferential arc of cold dust visible in the PACS maps and the 250 μm SPIRE map to the south of the disk also traces the edge of a superbubble observed in Hα and X-ray emission [Martin, 1998, Ott et al., 2003]. Cold dust filaments, clouds, broad regions, and clumps to the east and west of NGC 3077 are likely associated with the H I features [Yun et al., 1994, Walter et al., 2011]. The argument has been made that the superbubbles of hot plasma and ionized gas have yet to break out of this galaxy but potentially have enough

energy to generate a breakout wind in the northern direction where there is less H I density [Ott et al., 2003]. The cold dust emission along the north-south direction in the PACS maps appears stronger than the east-west emission while the inverse is true of the east-west emission in the SPIRE maps, which would seem to support the argument for a wind developing in the northern direction. Our deep PACS data provide evidence for this north-south emission, which was not identified in previous analysis of SPIRE data [Walter et al., 2011].

- *NGC 5253* - The morphology of the circumgalactic cold dust features in our PACS and SPIRE maps appears to follow the distribution of H I [Kobulnicky & Skillman, 2008] more closely than any other galaxy component. However, features like the broad emission regions extending from the northwest and southeast edges of the stellar disk in the *Herschel* maps do follow ionized gas features [Marlowe et al., 1995, Calzetti et al., 1999, Zastrow et al., 2011], X-ray emission [Martin & Kennicutt, 1995, Strickland & Stevens, 1999], and some 8.0 μm features [McCormick et al., 2013]. Filaments extend south in the 70, 160, and 250 μm maps, where the westernmost filament protruding from the southwest edge of the disk extends at least $\sim$2 kpc from the disk. In the PACS maps, a circumgalactic cold dust filament also extends directly north from the disk. Looking along the north-south direction, the 500 μm SPIRE map shows tenuous evidence for a significantly larger scale bipolar filamentary emission extending to $\sim$5 kpc outside the galactic disk. The southern extent of this emission appears disturbed and perhaps coincides with the H I plume

interpreted by Kobulnicky & Skillman [2008] as a potential outflow or inflow. However, no obvious counterpart for the northern filament presents itself in the H I images. The challenge of ruling out background sources or cold Milky Way dust clouds remains a concern for this north-south emission, but the brightest features from apparent clouds within this structure are $>4\sigma$ above the background in the 500 μm SPIRE map.

Bibliography

Aalto, S., Garcia-Burillo, S., Muller, S., et al. 2012, A&A, 537, A44

Alatalo, K., Blitz, L., Young, L. M., et al. 2011, ApJ, 735, 88

Allamandola, L. J., Tielens, A. G. G. M., & Barker, J. R. 1985, ApJ, 290, L25

Allamandola, L. J., Tielens, A. G. G. M., & Barker, J. R. 1989, ApJS, 71, 733

Allende Prieto, C., Lambert, D. L., & Asplund, M. 2001, ApJ, 556, L63

Alton, P. B., Bianchi, S., Rand, R. J., et al. 1998, ApJ, 507, L125

Alton, P. B., Davies, J. I., & Bianchi, S. 1999, A&A, 343, 51

Aniano, G., Draine, B. T., Gordon, K. D., & Sandstrom, K. 2011, PASP, 123, 1218

Armus, L., Charmandaris, V., Bernard-Salas, J., et al. 2007, ApJ, 656, 148

Barnes, J. E., & Hernquist, L. 1992, ARA&A, 30, 705

Balog, Z., Müller, T., Nielbock, M., et al. 2014, Experimental Astronomy, 37, 129

Bell, E. F., McIntosh, D. H., Katz, N., & Weinberg, M. D. 2003, ApJS, 149, 289

Blandford, R. D., & Narayan, R. 1992, ARA&A, 30, 311

Bolatto, A. D., Warren, S. R., Leroy, A. K., et al. 2013, Nature, 499, 450

Boylan-Kolchin, M., Bullock, J. S., & Kaplinghat, M. 2011, MNRAS, 415, L40

Boylan-Kolchin, M., Springel, V., White, S. D. M., Jenkins, A., & Lemson, G. 2009, MNRAS, 398, 1150

Brandl, B. R., Bernard-Salas, J., Spoon, H. W. W., et al. 2006, ApJ, 653, 1129

Bregman, J. N., & Houck, J. C. 1997, ApJ, 485, 159

Bregman, J. N., Miller, E. D., Seitzer, P., Cowley, C. R., & Miller, M. J. 2013, ApJ, 766, 57

Bregman, J. N., & Pildis, R. A. 1994, ApJ, 420, 570

Buote, D. A. 2000, ApJ, 539, 172

Burke, J. A. 1968, MNRAS, 140, 241

Calzetti, D., Conselice, C. J., Gallagher, J. S., III, & Kinney, A. L. 1999, AJ, 118, 797

Calzetti, D., Harris, J., Gallagher, J. S., III, et al. 2004, AJ, 127, 1405

Calzetti, D., Kennicutt, R. C., Engelbracht, C. W., et al. 2007, ApJ, 666, 870

Calzetti, D., Wu, S.-Y., Hong, S., et al. 2010, ApJ, 714, 1256

Casey, C. M. 2012, MNRAS, 425, 3094

Cecil, G., Bland-Hawthorn, J., Veilleux, S., & Filippenko, A. V. 2001, ApJ, 555, 338

Chromey, F. R., Elmegreen, D. M., Mandell, A., & McDermott, J. 1998, AJ, 115, 2331

Cicone, C., Maiolino, R., Sturm, E., et al. 2014, A&A, 562, AA21

Colbert, E. J. M., Baum, S. A., Gallimore, J. F., O'Dea, C. P., & Christensen, J. A. 1996, ApJ, 467, 551

Colbert, E. J. M., Baum, S. A., O'Dea, C. P., & Veilleux, S. 1998, ApJ, 496, 786

Cooper, J. L., Bicknell, G. V., Sutherland, R. S., & Bland-Hawthorn, J. 2008, ApJ, 674, 157

Cooper, J. L., Bicknell, G. V., Sutherland, R. S., & Bland-Hawthorn, J. 2009, ApJ, 703, 330

Cottrell, G. A. 1976, MNRAS, 174, 455

Dahlem, M., Heckman, T. M., Fabbiano, G., Lehnert, M. D., & Gilmore, D. 1996, ApJ, 461, 724

Dahlem, M., Weaver, K. A., & Heckman, T. M. 1998, ApJS, 118, 401

Dalcanton, J. J., Williams, B. F., Seth, A. C., et al. 2009, ApJS, 183, 67

Dale, D. A., Bendo, G. J., Engelbracht, C. W., et al. 2005, ApJ, 633, 857

Dale, D. A., Cohen, S. A., Johnson, L. C., et al. 2009, ApJ, 703, 517

Davis, M., Efstathiou, G., Frenk, C. S., & White, S. D. M. 1985, ApJ, 292, 371

de Grijs, R., & Peletier, R. F. 1997, A&A, 320, L21

de Vaucouleurs, G., de Vaucouleurs, A., Corwin, H. G., Jr., et al. 1991, Third Reference Catalogue of Bright Galaxies (New York, NY: Springer)

della Ceca, R., Griffiths, R. E., Heckman, T. M., & MacKenty, J. W. 1996, ApJ, 469, 662

Di Matteo, T., Springel, V., & Hernquist, L. 2005, Nature, 433, 604

Diamond-Stanic, A. M., & Rieke, G. H. 2010, ApJ, 724, 140

Draine, B. T. 2003, ARA&A, 41, 241

Draine, B. T., Dale, D. A., Bendo, G., et al. 2007, ApJ, 663, 866

Ehle, M., Dahlem, M., Jiménez Bailón, E., Santos-Lleó, M., & Read, A. M. 2004, IAU Symp. 217, Recycling Intergalactic and Interstellar Medium, held in Syndey, Australia, Ed P.-A. Duc J. Braine and E. Brinks, San Francisco: ASP, 154

Einstein, A. 1917, Sitzungsberichte der Königlich Preußischen Akademie der Wissenschaften (Berlin), Seite 142-152., 142

Elmouttie, M., Haynes, R. F., Jones, K. L., et al. 1997, MNRAS, 284, 830

Engelbracht, C. W., Kundurthy, P., Gordon, K. D., et al. 2006, ApJ, 642, L127

Erb, D. K., Quider, A. M., Henry, A. L., & Martin, C. L. 2012, ApJ, 759, 26

Fabbiano, G., Heckman, T., & Keel, W. C. 1990, ApJ, 355, 442

Feldmann, R. 2015, MNRAS, 449, 3274

Ferguson, A. M. N., Wyse, R. F. G., & Gallagher, J. S. 1996, AJ, 112, 2567

Ferrarese, L., & Merritt, D. 2000, ApJ, 539, L9

Feruglio, C., Maiolino, R., Piconcelli, E., et al. 2010, A&A, 518, L155

Fischer, J., Sturm, E., González-Alfonso, E., et al. 2010, A&A, 518, L41

Ford, H. C., Dahari, O., Jacoby, G. H., Crane, P. C., & Ciardullo, R. 1986, ApJ,

311, L7

Gallimore, J. F., Axon, D. J., O'Dea, C. P., Baum, S. A., & Pedlar, A. 2006, AJ, 132, 546

Gebhardt, K., Bender, R., Bower, G., et al. 2000, ApJ, 539, L13

Gnedin, N. Y., & Draine, B. T. 2014, ApJ, 795, 37

Gordon, K. D., Engelbracht, C. W., Rieke, G. H., et al. 2008, ApJ, 682, 336

Graham, J. A., & Lawrie, D. G. 1982, ApJ, 253, L73

Griffin, M. J., Abergel, A., Abreu, A., et al. 2010, A&A, 518, L3

Grocholski, A. J., Aloisi, A., van der Marel, R. P., et al. 2008, ApJ, 686, L79

Gültekin, K., Richstone, D. O., Gebhardt, K., et al. 2009, ApJ, 698, 198

Hameed, S., & Devereux, N. 1999, AJ, 118, 730

Haynes, M. P., Giovanelli, R., & Roberts, M. S. 1979, ApJ, 229, 83

Hazard, C. 1962, MNRAS, 124, 343

Heckman, T. M., Armus, L., & Miley, G. K. 1990, ApJS, 74, 833

Heckman, T. M., Dahlem, M., Lehnert, M. D., et al. 1995, ApJ, 448, 98

Heckman, T. M., Lehnert, M. D., Strickland, D. K., & Armus, L. 2000, ApJS, 129, 493

Heckman, T. M., Sembach, K. R., Meurer, G. R., et al. 2001, ApJ, 554, 1021

Herschel, W. 1785, Royal Society of London Philosophical Transactions Series I, 75,

213

Hodge, P. W. 1974, ApJ, 191, L21

Högbom, J. A. 1974, A&AS, 15, 417

Hoopes, C. G., Walterbos, R. A. M., & Greenwalt, B. E. 1996, AJ, 112, 1429

Hoopes, C. G., Heckman, T. M., Strickland, D. K., et al. 2005, ApJ, 619, L99

Hopkins, P. F., Croton, D., Bundy, K., et al. 2010, ApJ, 724, 915

Hopkins, P. F., & Elvis, M. 2010, MNRAS, 401, 7

Hopkins, P. F., & Quataert, E. 2010, MNRAS, 407, 1529

Howk, J. C., & Savage, B. D. 1997, AJ, 114, 2463

Howk, J. C., & Savage, B. D. 2000, AJ, 119, 644

Hubble, E. 1929, Proceedings of the National Academy of Science, 15, 168

Hummel, E., van Gorkom, J. H., & Kotanyi, C. G. 1983, ApJ, 267, L5

Hunter, D. A., Hawley, W. N., & Gallagher, J. S., III 1993, AJ, 106, 1797

Hunter, D. A., van Woerden, H., & Gallagher, J. S., III 1994, ApJS, 91, 79

Hunter, D. A. 1996, ApJ, 457, 671

Huo, Z. Y., Xia, X. Y., Xue, S. J., Mao, S., & Deng, Z. G. 2004, ApJ, 611, 208

Irwin, J. A., & Sofue, Y. 1996, ApJ, 464, 738

Irwin, J. A., Wilson, C. D., Wiegert, T., et al. 2011, MNRAS, 410, 1423

Johnson, H. E., & Axford, W. I. 1971, ApJ, 165, 381

Johnson, K. E., Leitherer, C., Vacca, W. D., & Conti, P. S. 2000, AJ, 120, 1273

Jurac, S., Johnson, R. E., & Donn, B. 1998, ApJ, 503, 247

Kamphuis, P., Holwerda, B. W., Allen, R. J., Peletier, R. F., & van der Kruit, P. C. 2007, A&A, 471, L1

Kaneda, H., Ishihara, D., Suzuki, T., et al. 2010, A&A, 514, A14

Kaneda, H., Yamagishi, M., Suzuki, T., & Onaka, T. 2009, ApJ, 698, L125

Karachentsev, I. D., Dolphin, A. E., Geisler, D., et al. 2002, A&A, 383, 125

Karachentsev, I. D., Kaisina, E. I., & Makarov, D. I. 2014, AJ, 147, 13

Karachentsev, I. D., & Makarov, D. I. 1999, Galaxy Interactions at Low and High Redshift, 186, 109

Kennicutt, R. C., Jr. 1998, ApJ, 498, 541

Kennicutt, R. C., Jr., Armus, L., Bendo, G., et al. 2003, PASP, 115, 928

Kennicutt, R. C., Jr., Hao, C.-N., Calzetti, D., et al. 2009, ApJ, 703, 1672

Kennicutt, R. C., Jr., Lee, J. C., Funes, S. J., José G., Sakai, S., & Akiyama, S. 2008, ApJS, 178, 247

Kewley, L. J., & Ellison, S. L. 2008, ApJ, 681, 1183

Kobulnicky, H. A., Dickey, J. M., Sargent, A. I., Hogg, D. E., & Conti, P. S. 1995, AJ, 110, 116

Kobulnicky, H. A., Kennicutt, R. C., Jr., & Pizagno, J. L. 1999, ApJ, 514, 544

Kobulnicky, H. A., & Martin, C. L. 2010, ApJ, 718, 724

Kobulnicky, H. A., & Skillman, E. D. 2008, AJ, 135, 527

Komatsu, E., Dunkley, J., Nolta, M. R., et al. 2009, ApJS, 180, 330

Koo, B.-C., & McKee, C. F. 1992, ApJ, 388, 93

Koo, B.-C., & McKee, C. F. 1992, ApJ, 388, 103

Koribalski, B. S., Staveley-Smith, L., Kilborn, V. A., et al. 2004, AJ, 128, 16

Kormendy, J., & Bahcall, J. N. 1974, AJ, 79, 671

Kroupa, P. 2001, MNRAS, 322, 231

Krügel, E. 2002, Wiley Praxis Series in Astronomy and Astrophysics, 10,

Lauberts, A. & Valentijn, E. A. 1989, The Surface Photometry Catalogue of the ESO-Uppsala Galaxies (Garching, Germany: ESO)

Leger, A., & Puget, J. L. 1984, A&A, 137, L5

Leitherer, C., Schaerer, D., Goldader, J. D., et al. 1999, ApJS, 123, 3

Lehnert, M. D., & Heckman, T. M. 1995, ApJS, 97, 89

Lehnert, M. D., Heckman, T. M., & Weaver, K. A. 1999, ApJ, 523, 575

Lequeux, J. 2005, The interstellar medium, Translation from the French language edition of: Le Milieu Interstellaire by James Lequeux, EDP Sciences, 2003 Edited by J. Lequeux. Astronomy and astrophysics library, Berlin: Springer, 2005,

Lowenthal, J. D., Koo, D. C., Guzman, R., et al. 1997, ApJ, 481, 673

Lupton, R. H., Gunn, J. E., & Szalay, A. S. 1999, AJ, 118, 1406

Lynds, C. R., & Sandage, A. R. 1963, ApJ, 137, 1005

Mac Low, M.-M., & McCray, R. 1988, ApJ, 324, 776

Mac Low, M.-M., McCray, R., & Norman, M. L. 1989, ApJ, 337, 141

Madau, P., & Dickinson, M. 2014, ARA&A, 52, 415

Magorrian, J., Tremaine, S., Richstone, D., et al. 1998, AJ, 115, 2285

Makovoz, D., & Khan, I. 2005, Astronomical Data Analysis Software and Systems XIV, 347, 81

Marble, A. R., Engelbracht, C. W., van Zee, L., et al. 2010, ApJ, 715, 506

Marlowe, A. T., Heckman, T. M., Wyse, R. F. G., & Schommer, R. 1995, ApJ, 438, 563

Martin, C. L. 1997, ApJ, 491, 561

Martin, C. L. 1998, ApJ, 506, 222

Martin, C. L. 1999, ApJ, 513, 156

Martin, C. L. 2005, ApJ, 621, 227

Martin, C. L., & Kennicutt, R. C., Jr. 1995, ApJ, 447, 171

Martin, C. L., Kobulnicky, H. A., & Heckman, T. M. 2002, ApJ, 574, 663

Martin, C. L., Shapley, A. E., Coil, A. L., et al. 2012, ApJ, 760, 127

Mathews, W. G., & Baker, J. C. 1971, ApJ, 170, 241

McCormick, A., Veilleux, S., & Rupke, D. S. N. 2013, ApJ, 774, 126

McDowell, J. C., Clements, D. L., Lamb, S. A., et al. 2003, ApJ, 591, 154

McGaugh, S. S., & de Blok, W. J. G. 1998, ApJ, 499, 41

McQuade, K., Calzetti, D., & Kinney, A. L. 1995, ApJS, 97, 331

Meléndez, M., Veilleux, S., Martin, C., et al. 2015, ApJ, 804, 46

Méndez, D. I., Esteban, C., Filipović , M. D., et al. 1999, A&A, 349, 801

Melnick, J., Moles, M., & Terlevich, R. 1985, A&A, 149, L24

Meurer, G. R., Freeman, K. C., & Dopita, M. A. 1989, Ap&SS, 156, 141

Meurer, G. R., Freeman, K. C., Dopita, M. A., & Cacciari, C. 1992, AJ, 103, 60

Meurer, G. R., Staveley-Smith, L., & Killeen, N. E. B. 1998, MNRAS, 300, 705

Milgrom, M. 1983, ApJ, 270, 365

Miller, S. T., & Veilleux, S. 2003, ApJS, 148, 383

Moorwood, A. F. M., van der Werf, P. P., Kotilainen, J. K., Marconi, A., & Oliva, E. 1996, A&A, 308, L1

Moshir, M., Kopan, G., Conrow, T., et al. 1990, BAAS, 22, 1325

Moustakas, J., & Kennicutt, R. C., Jr. 2006, ApJS, 164, 81

Moustakas, J., Kennicutt, R. C., Jr., Tremonti, C. A., et al. 2010, ApJS, 190, 233

Nakai, N. 1989, PASJ, 41, 1107

Narayanan, D., Cox, T. J., Kelly, B., et al. 2008, ApJS, 176, 331

Ott, J., Martin, C. L., & Walter, F. 2003, ApJ, 594, 776

Ott, S. 2010, Astronomical Data Analysis Software and Systems XIX, 434, 139

Otte, B., & Dettmar, R.-J. 1999, A&A, 343, 705

Peacock, J. A., Cole, S., Norberg, P., et al. 2001, Nature, 410, 169

Penzias, A. A., & Wilson, R. W. 1965, ApJ, 142, 419

Perlmutter, S., Aldering, G., Goldhaber, G., et al. 1999, ApJ, 517, 565

Pettini, M., & Pagel, B. E. J. 2004, MNRAS, 348, L59

Pettini, M., Shapley, A. E., Steidel, C. C., et al. 2001, ApJ, 554, 981

Phillips, A. C. 1993, AJ, 105, 486

Pietsch, W., Trinchieri, G., & Vogler, A. 1998, A&A, 340, 351

Pietsch, W., Vogler, A., Klein, U., & Zinnecker, H. 2000, A&A, 360, 24

Pilbratt, G. L., Riedinger, J. R., Passvogel, T., et al. 2010, A&A, 518, L1

Planck Collaboration, Ade, P. A. R., Aghanim, N., et al. 2014, A&A, 571, A16

Planck Collaboration, Ade, P. A. R., Aghanim, N., et al. 2015, arXiv:1502.01589

Poglitsch, A., Waelkens, C., Geis, N., et al. 2010, A&A, 518, L2

Radovich, M., Kahanpää, J., & Lemke, D. 2001, A&A, 377, 73

Rasmussen, J., Stevens, I. R., & Ponman, T. J. 2004, MNRAS, 354, 259

Reach, W. T., Rho, J., Tappe, A., et al. 2006, AJ, 131, 1479

Read, A. M., Ponman, T. J., & Strickland, D. K. 1997, MNRAS, 286, 626

Reines, A. E., Sivakoff, G. R., Johnson, K. E., & Brogan, C. L. 2011, Nature, 470, 66

Rémy-Ruyer, A., Madden, S. C., Galliano, F., et al. 2014, A&A, 563, A31

Renzini, A. 1997, ApJ, 488, 35

Riess, A. G., Filippenko, A. V., Challis, P., et al. 1998, AJ, 116, 1009

Rossa, J., & Dettmar, R.-J. 2003, A&A, 406, 493

Roussel, H. 2013, PASP, 125, 1126

Roussel, H., Wilson, C. D., Vigroux, L., et al. 2010, A&A, 518, L66

Rubin, V. C., & Ford, W. K., Jr. 1970, ApJ, 159, 379

Rupke, D. S., Veilleux, S., & Sanders, D. B. 2002, ApJ, 570, 588

Rupke, D. S., Veilleux, S., & Sanders, D. B. 2005a, ApJS, 160, 87

Rupke, D. S., Veilleux, S., & Sanders, D. B. 2005b, ApJS, 160, 115

Rupke, D. S., Veilleux, S., & Sanders, D. B. 2005c, ApJ, 632, 751

Sakai, S., Ferrarese, L., Kennicutt, R. C., Jr., & Saha, A. 2004, ApJ, 608, 42

Sakamoto, K., Ho, P. T. P., Iono, D., et al. 2006, ApJ, 636, 685

Sanders, D. B., Mazzarella, J. M., Kim, D.-C., Surace, J. A., & Soifer, B. T. 2003, AJ, 126, 1607

Sanders, D. B., & Mirabel, I. F. 1996, ARA&A, 34, 749

Schiano, A. V. R. 1985, ApJ, 299, 24

Schmidt, B. P., Suntzeff, N. B., Phillips, M. M., et al. 1998, ApJ, 507, 46

Schwartz, C. M., & Martin, C. L. 2004, ApJ, 610, 201

Seth, A. C., Dalcanton, J. J., & de Jong, R. S. 2005, AJ, 129, 1331

Shapley, A. E., Steidel, C. C., Pettini, M., & Adelberger, K. L. 2003, ApJ, 588, 65

Sharp, R. G., & Bland-Hawthorn, J. 2010, ApJ, 711, 818

Skrutskie, M. F., Cutri, R. M., Stiening, R., et al. 2003, yCat, 7233, 0

Smail, I., Chapman, S. C., Ivison, R. J., et al. 2003, MNRAS, 342, 1185

Smith, J. D. T., Draine, B. T., Dale, D. A., et al. 2007, ApJ, 656, 770

Smith, M. W. L., Eales, S. A., Gomez, H. L., et al. 2012, ApJ, 756, 40

Spitoni, E., Calura, F., Matteucci, F., & Recchi, S. 2010, A&A, 514, A73

Springel, V., Di Matteo, T., & Hernquist, L. 2005, MNRAS, 361, 776

Springel, V., Wang, J., Vogelsberger, M., et al. 2008, MNRAS, 391, 1685

Springel, V., White, S. D. M., Jenkins, A., et al. 2005, Nature, 435, 629

Springob, C. M., Masters, K. L., Haynes, M. P., Giovanelli, R., & Marinoni, C. 2009, ApJS, 182, 474

Steidel, C. C., Erb, D. K., Shapley, A. E., et al. 2010, ApJ, 717, 289

Stone, J. L., Jr., Wilson, A. S., & Ward, M. J. 1988, ApJ, 330, 105

Strickland, D. K. 2007, MNRAS, 376, 523

Strickland, D. K., Heckman, T. M., Colbert, E. J. M., Hoopes, C. G., & Weaver,

K. A. 2004a, ApJS, 151, 193

Strickland, D. K., Heckman, T. M., Colbert, E. J. M., Hoopes, C. G., & Weaver, K. A. 2004b, ApJ, 606, 829

Strickland, D. K., Heckman, T. M., Weaver, K. A., Hoopes, C. G., & Dahlem, M. 2002, ApJ, 568, 689

Strickland, D. K., Ponman, T. J., & Stevens, I. R. 1997, A&A, 320, 378

Strickland, D. K., & Stevens, I. R. 1999, MNRAS, 306, 43

Sturm, E., González-Alfonso, E., Veilleux, S., et al. 2011, ApJ, 733, L16

Swaters, R. A., Valdes, F., & Dickinson, M. E. 2009, Astronomical Data Analysis Software and Systems XVIII, 411, 506

Tacconi-Garman, L. E., Sturm, E., Lehnert, M., et al. 2005, A&A, 432, 91

Thronson, H. A., Jr., Wilton, C., & Ksir, A. 1991, MNRAS, 252, 543

Toomre, A., & Toomre, J. 1972, ApJ, 178, 623

Tosi, M., Sabbi, E., Bellazzini, M., et al. 2001, AJ, 122, 1271

Tremaine, S. 1992, Physics Today, 45, 28

Tremonti, C. A., Heckman, T. M., Kauffmann, G., et al. 2004, ApJ, 613, 898

Trumpler, R. J. 1930, PASP, 42, 214

Tüllmann, R., Breitschwerdt, D., Rossa, J., Pietsch, W., & Dettmar, R.-J. 2006, A&A, 457, 779

Tully, R. B. 1988, Nearby Galaxies Catalog (Cambridge: Cambridge University Press)

Tully, R. B., Rizzi, L., Shaya, E. J., et al. 2009, AJ, 138, 323

van der Hulst, J. M. 1979, A&A, 75, 97

Vázquez, G. A., & Leitherer, C. 2005, ApJ, 621, 695

Veilleux, S., Bland-Hawthorn, J., Cecil, G., Tully, R. B., & Miller, S. T. 1999, ApJ, 520, 111

Veilleux, S., Cecil, G., & Bland-Hawthorn, J. 2005, ARA&A, 43, 769

Veilleux, S., Cecil, G., Bland-Hawthorn, J., et al. 1994, ApJ, 433, 48

Veilleux, S., Meléndez, M., Sturm, E., et al. 2013, ApJ, 776, 27

Veilleux, S., & Rupke, D. S. 2002, ApJ, 565, L63

Veilleux, S., Rupke, D. S. N., Kim, D.-C., et al. 2009a, ApJS, 182, 628

Veilleux, S., Rupke, D. S. N., & Swaters, R. 2009b, ApJ, 700, L149

Veilleux, S., Shopbell, P. L., & Miller, S. T. 2001, AJ, 121, 198

Waller, W. H. 1991, ApJ, 370, 144

Walter, F., Brinks, E., de Blok, W. J. G., et al. 2008, AJ, 136, 2563

Walter, F., & Heithausen, A. 1999, ApJ, 519, L69

Walter, F., Sandstrom, K., Aniano, G., et al. 2011, ApJ, 726, L11

Walter, F., Weiss, A., & Scoville, N. 2002, ApJ, 580, L21

Wang, Q. D., Immler, S., Walterbos, R., Lauroesch, J. T., & Breitschwerdt, D. 2001, ApJ, 555, L99

Ward, M., Penston, M. V., Blades, J. C., & Turtle, A. J. 1980, MNRAS, 193, 563

Weiner, B. J., Coil, A. L., Prochaska, J. X., et al. 2009, ApJ, 692, 187

Westmoquette, M. S., Smith, L. J., & Gallagher, J. S. 2008, MNRAS, 383, 864

Willick, J. A., Courteau, S., Faber, S. M., et al. 1997, ApJS, 109, 333

Wilson, R. W., Jefferts, K. B., & Penzias, A. A. 1970, ApJ, 161, L43

Wolf, M. 1923, Astronomische Nachrichten, 219, 109

Yasuda, N., Fukugita, M., & Okamura, S. 1997, ApJS, 108, 417

Young, J. S., Xie, S., Tacconi, L., et al. 1995, ApJS, 98, 219

Yun, M. S., Ho, P. T. P., & Lo, K. Y. 1994, Nature, 372, 530

Zahid, H. J., Bresolin, F., Kewley, L. J., Coil, A. L., & Davé, R. 2012, ApJ, 750, 120

Zastrow, J., Oey, M. S., Veilleux, S., & McDonald, M. 2013, ApJ, 779, 76

Zastrow, J., Oey, M. S., Veilleux, S., McDonald, M., & Martin, C. L. 2011, ApJ, 741, L17

Zhu, G., Ménard, B., Bizyaev, D., et al. 2014, MNRAS, 439, 3139

Zwicky, F. 1937, ApJ, 86, 217

Zwicky, F. 1956, Ergebnisse der exakten Naturwissenschaften, 29, 344